CONSTRAINTS ON INCREMENTAL ASSEMBLY OF UPPER CRUSTAL IGNEOUS INTRUSIONS, MOUNT ELLEN, HENRY MOUNTAINS, UTAH

By

Laura Isabel Maria de Sousa

December, 2021

Director of Thesis: Dr. Eric Horsman
Major Department: Geological Sciences

Magma systems within the shallow crust drive volcanic processes at the surface. Studying active magma systems directly poses significant difficulty but details of ancient magma systems can provide insight to modern systems. The ancient intrusions now exposed in the Henry Mountains of southern Utah provide an excellent opportunity to study the emplacement of igneous intrusions within the shallow crust. The five main intrusive centers of the Henry Mountains are Oligocene in age and preserve different stages in the development of an igneous system within the shallow crust. Recent studies worldwide have demonstrated that most substantial (> 0.5 km^3) igneous intrusions in the shallow crust are incrementally assembled from multiple magma pulses. In the Henry Mountains, smaller component intrusions (< 0.5 km3) clearly demonstrate incremental assembly but an evaluation of incremental assembly for an entire intrusive center has yet to be performed.

The Mount Ellen intrusive complex is the largest intrusive center (~ 100 km^3, 15 – 20 km diameter) in the Henry Mountains. This thesis research provides constraints on the construction history and emplacement of Mount Ellen using a combination of multiple techniques, including fieldwork, whole-rock major and trace element geochemistry, anisotropy of magnetic susceptibility, and crystal size distribution analysis. Field work and anisotropy of magnetic

susceptibility data suggest that Mount Ellen is a laccolith that in cross section is built a network of stacked igneous sheets. In map-view, the laccolith has an elliptical shape built from numerous igneous lobes radiating away from the central portion of the intrusion. Field observations suggest most lobes are texturally homogenous and likely emplaced from a single magma batch.

Samples collected throughout Mount Ellen were divided into five groups based on a qualitative evaluation of texture. Possible distinctions between these textural groups were then tested using several different techniques. Geochemistry, anisotropy of magnetic susceptibility, and phenocryst crystal size distribution data are individually not sufficient to distinguish all five textural groups. However, limited datasets for two textures can be consistently distinguished using these techniques.

These new results can be integrated with existing constraints to create a comprehensive model for the construction history of Mount Ellen. The intrusive center was constructed in approximately 1 million years at a time-averaged magma injection rate of 0.0004 km3 y^{-1}. The laccolith geometry was built from a radiating network of stacked igneous sheets. The sheets are lobate in map-view (longer than they are wide) and were fed radially outward from a central feeder zone. These component intrusions were emplaced by a minimum of 5 texturally distinct magma pulses, with periods of little or no magmatism between sequential pulses.

CONSTRAINTS ON INCREMENTAL ASSEMBLY OF UPPER CRUSTAL IGNEOUS INTRUSIONS, MOUNT ELLEN, HENRY MOUNTAINS, UTAH

A Thesis Presented To

The Faculty of the Department of Geological Sciences

East Carolina University

In Partial Fulfilment of the Requirements for the Degree

Master of Science in Geology

by

Laura Isabel Maria de Sousa

December, 2021

CONSTRAINTS ON INCREMENTAL ASSEMBLY OF UPPER CRUSTAL IGNEOUS INTRUSIONS, MOUNT ELLEN, HENRY MOUNTAINS, UTAH

By

Laura Isabel Maria de Sousa

APPROVED BY:

DIRECTOR OF THESIS

Eric Horsman, PhD

COMMITTEE MEMBER:

Adriana Heimann, PhD

COMMITTEE MEMBER:

David Mallinson, PhD

COMMITTEE MEMBER:

Scott Giorgis, PhD

CHAIR OF THE DEPARTMENT
OF GEOLOGICAL SCIENCES:

Stephen J. Culver, PhD

DEAN OF THE
GRADUATE SCHOOL:

Paul J. Gemperline, PhD

Acknowledgments

I would like to whole-heartedly thank my thesis advisor Dr. Eric Horsman, without his encouragement I would not have made it through this whole process. He has not only been extremely supportive and understanding but has proven to be nothing short of an amazing advisor and a wonderful human-being. I would also like to thank my committee members, Dr. Adriana Heimann, Dr. Scott Giorgis, and Dr. David Mallinson for their involvement in the completion of my thesis.

Secondly, I would like to thank Trevor Burns for assistance in the field. It was an experience I will never forget with many laughs and a lot of hiking. I hope T.J. is doing well in college.

Thirdly, a special thanks to my parents, I would not be who I am today without them. Thank you for motivating me to be the best I can be and to never settle for less. Don’t worry, be happy. I would also like to thank Seth Sutton for being the most supportive friend through every moment of doubt along this journey and for always listening to me rant about my thesis work.

Finally, I would like to thank the National Science Foundation, the Geological Society of America, and Sigma Xi for funding this project.

TABLE OF CONTENTS

LIST OF TABLES

LIST OF FIGURES

LIST OF ABBREVIATIONS

AMS	Anisotropy of magnetic susceptibility	5
CSD	Crystal Size Distribution	5
REE	Rare Earth Elements	85

LIST OF EQUATIONS

Equation 1.	$P_\mathrm{d} = P_h + P_o - P_{vis} - S_\mathrm{h}$,	Magma driving pressure
Equation 2.	$T = bL^a$,	Intrusion thickness to length relationship
Equation 3.	$T = dL^c$,	Intrusion thickness to volume relationship
Equation 4.	$\mathrm{K}_m = (\mathrm{K}_1 + \mathrm{K}_2 + \mathrm{K}_3)/3$,	Mean susceptibility
Equation 5.	$\mathrm{T} = [2\ln(\mathrm{K}_2/\mathrm{K}_3)/\ln(\mathrm{K}_1/\mathrm{K}_3)] - 1$,	Shape of AMS ellipsoid
Equation 6.	$P_j = \exp(2[(\eta_1 - \eta_b)^2 + (\eta_2 - \eta_b)^2 + (\eta_3 - \eta_b)^2]^{½}$,	Intensity of magnetic fabric
Equation 7.	$L = K_1/K_2$,	Lineation
Equation 8.	$F = K_2/K_3$,	Foliation
Equation 9.	$n'_V(L) = n'_V(0)\mathrm{e}^{-L/G\tau}$,	Population density
Equation 10.	$C = G\tau$,	Characteristic length
Equation 11.	$\tau = (-1/Gxm)/3153600$,	Residence time

GLOSSARY

Note: Terms listed in this glossary are defined based on their use within the context of this thesis.

Emplacement	Refers to the displacement of host rock to accommodate space for injection of magma pulse(s).
Laccolith	A igneous intrusion geometry with a flat base, steep sides, and an arched to flat roof that is constructed from either a single magma pulse, multiple magma pulses, and/or stacked sills. Generally, a laccolith is 30 m or greater in thickness.
Pluton	A body of igneous rock.
Pulse	A single injection of magma emplaced in the upper crust.
Sill	A sheet-like igneous intrusions that can be constructed from a single magma pulse or multiple magma pulses. A sill is typically no greater than 10 m thick.
Sheet	An igneous intrusion with a tabular shape

1. Introduction

Our understanding of how magma systems develop in the shallow crust has changed considerably in recent years. Traditionally, many upper crustal plutons were interpreted as a single, contiguous magma body that cooled and crystallized (Fig. 1). However, detailed research on well-exposed igneous intrusions has changed how we view many of these systems. Instead of a single magma body, many intrusions form through sequential injections of separate magma pulses (Coleman et al, 2004, Glazner et al, 2004). Studies on various size upper crustal igneous intrusions, ranging from sills to batholiths, have shown incremental assembly of intrusive systems across all these spatial scales (de Saint Blanquet et al., 2001, 2011; Coleman et al, 2004; Glazner et al, 2004; Horsman et al, 2005, 2010; Morgan et al, 2008).

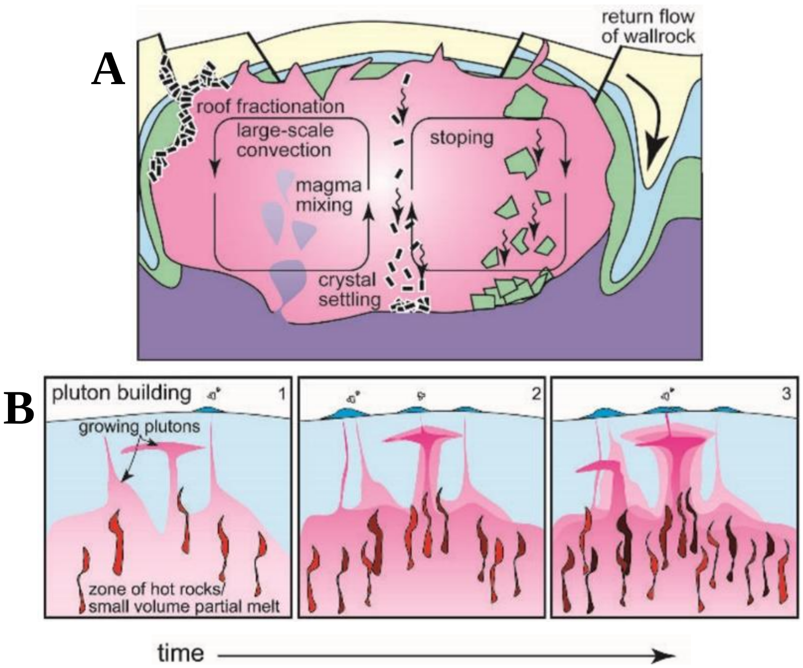

Figure 1. A "Big Tank" diagram showing how upper crustal intrusions appeared to be one giant magma body in contrast to incrementally assembled over time **B.** Diagrammatic sketch of current understanding of pluton emplacement based on smaller batches of magma ascending from mid crust through dikes. Darker reds represent ascending magma and cooler reds represent cooling of magma (Glazner, 2004).

Geochronological data and thermal models clearly demonstrate that crustal magma bodies solidify rapidly below the solidus in thousands of years and larger magma bodies in hundreds of thousands of years for small volume intrusions (Glazner et al. 2004). This suggests that for larger plutons to form on a timescale in the order of millions of years, they would have to be gradually assembled and not emplaced as a single large magma body as assumed by the traditional model.

Saint Blanquat et al. (2011) evaluated various sized upper crustal igneous intrusions and suggest there is a positive correlation between intrusion volume and the duration of construction. The overall volume of an intrusion is a product of magmatic pulses contributing to its construction over a particular timescale (Fig 2). Most importantly, Saint Blanquat et al. (2011) concluded that the vast majority of intrusions form during active tectonic conditions. The longer a magma body is affected by tectonics (while still in a partially liquid state), the more its fabric/texture are influenced by tectonic deformation. Internal contacts may then become cryptic and not easily defined. Smaller intrusions that cool more rapidly and record little about tectonic conditions, preserve a better record of intrusion emplacement processes.

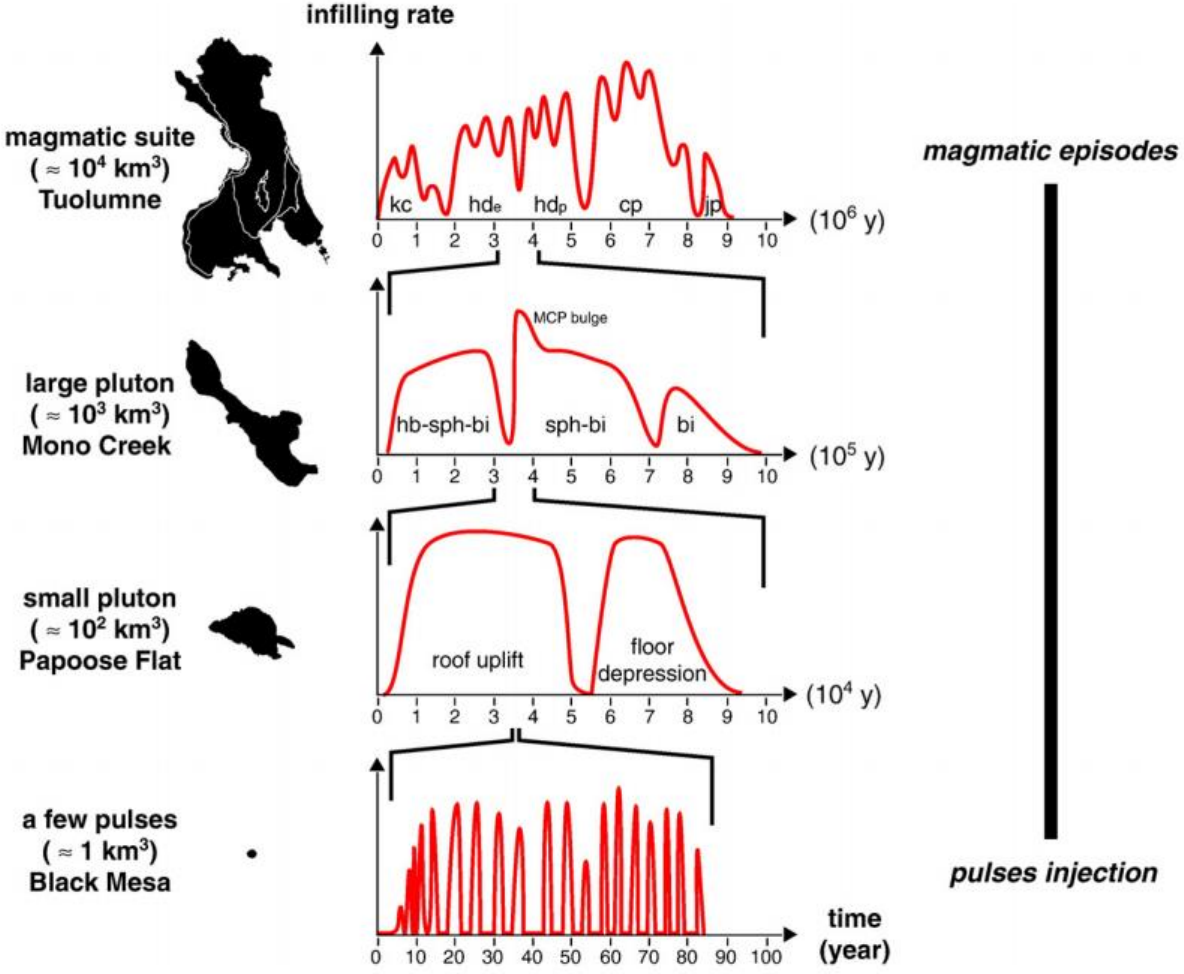

Figure 2. Illustration of upper crustal igneous intrusion construction with time (Saint Blanquat et al. 2011).

This improved understanding of how upper crustal igneous intrusions are constructed aids in interpretation of modern volcanic processes, which are driven by magma propagating through the upper crust. Unfortunately, magma beneath active volcanic systems can only be studied through indirect methods such as remote sensing. However, the study of ancient intrusions now exposed at the surface provides a way to understand these magma systems in detail. Studying ancient igneous intrusions can be difficult due to deformation, lack of exposure, and preservation. The Oligocene intrusions in the Henry Mountains of Utah are well-exposed and lack synmagmatic tectonic deformation, making this an ideal location to study ancient upper crustal intrusions.

The Henry Mountains of southern Utah consist of five intrusive centers that are Oligocene in age (Nelson et al, 1992, Murray et al., 2016). Previous work suggests small component intrusions, like sills, in the Henry Mountains are incrementally assembled (de Saint Blanquet et al., 2006; Morgan et al., 2008; Broda, 2014; Ward, 2014; Maurer, 2015; Thorton, 2015; Horsman et al. 2018), but the large intrusive centers themselves have not been studied in enough detail to determine their growth histories. In large intrusions, a distinction between separate magma pulses may be difficult to recognize unless substantial compositional differences make this distinction apparent (Wiebe & Collins, 1998; Michel et al 2008). Previous work performed by Nelson & Davidson (1993) suggest the igneous rock in the Henry Mountains is compositionally homogenous, although limited isotope data hint that separate intrusive centers may have distinct magma systems. However, the data produced by Nelson & Davidson (1993) are limited to a few samples and did not capture the composition of the igneous rock thoroughly throughout the Henry Mountains.

Where detailed work has been done, clear evidence does exist in the Henry Mountains for incremental assembly of small-volume (less than 5 km^3) igneous intrusions (de Saint Blanquet et al., 2006; Morgan et al., 2008; Broda, 2014; Ward, 2014; Maurer, 2015; Thorton, 2015; Horsman et al. 2018). For example, detailed work on the Copper Ridge laccolith demonstrates compositional differences and distinct magma sheets (Maurer, 2015). More generally, most very small-volume component intrusions ($< l$ km^3) within an igneous center in the Henry Mountains tend to have a consistent texture (Horsman et al., 2005; de Saint Blanquat et al., 2006; Morgan et al., 2008), but texture varies both between separate component intrusions and within larger igneous bodies. Detailed work on the Mount Pennell intrusive center (Ward, 2014) demonstrates very clear textural and compositional differences. The spatial distribution of several separate igneous rock units can be mapped out. It is evident that some compositional and textural differences do exist, at least locally, but a detailed comparison between all five intrusive centers in the Henry Mountains has yet to be performed.

For this study, new data for a single intrusive center, Mount Ellen, were collected and synthesized with previously collected data. With this compilation and through field observations, analysis of geochemical major and trace elements, anisotropy of magnetic susceptibility (AMS), and crystal size distribution data (CSD), I test the hypothesis that Mount Ellen was constructed from numerous component magma pulses.

2. Magmatism in the Shallow Crust: Igneous Intrusions

Understanding how magma systems operate in the shallow crust (< 5 km) is essential for understanding the construction of igneous intrusions. The mechanism through which magma is supplied and how it is emplaced into the shallow crust promotes the formation of igneous intrusions of various sizes, ranging from sills to batholiths. To begin to understand the formation of igneous intrusions, the following need to be addressed: (1) magma supply through vertical dike propagation; (2) sill formation through lateral emplacement of magma; and (3) lateral termination and vertical thickening.

2.1 Magma Supply Through Vertical Dike Propagation

Dikes are the fundamental conduits for pressurized magma to propagate through the upper crust and form igneous bodies (Gudmundsson, 1986, 1990, 1999; Parson et al., 1992; Petford et al., 1993; Annen and Sparks, 2002; Annen et al., 2006; Kavanagh et al., 2006; Annen et al., 2008; Menand, 2008; Daniels, et al., 2012; Gonnermann and Taisne, 2015). Generally, dikes are 1 – 10 m in thickness and extend from 1 – 15 km from their source (Baer and Reches, 1991). To accommodate the ascending magma, dikes propagate in existing fractures or may create their own fractures through existing host rock. Determining which scenario was favored in a particular case can be difficult (Rubin, 1995; Gonnermann and Taisne, 2015).

For magma to ascend through pre-existing fractures or newly created fractures, the magma driving pressure needs to exceed the confining pressure of surrounding host rock to keep the dike from closing (Gonnermann and Taisne, 2015). The magma driving pressure can be defined by

$$(1) \qquad P_{\mathrm{d}} = P_h + P_o - P_{vis} - S_{\mathrm{h}},$$

where P_h is the hydrostatic pressure, P_o is the overpressure of the magma chamber, P_{vis} is the pressure loss due to viscous flow, S_h is the stress perpendicular to the ascending dike walls (Reches and Fink, 1988; Baer and Reches, 1991; Hogan and Gilbert, 1995; Hogan et al., 1998). Of these variables, the hydrostatic pressure predominantly influences the magma driving pressure. Hydrostatic pressure is the difference between the pressure at the top of the magma source (i.e. magma chamber) and the pressure at the tip of the ascending magma. If there is a greater contribution of hydrostatic pressure than there is contribution from horizontal stress, the magma driving pressure will increase (Rocchi et al. 2010).

Other variables that affect the driving pressure of magma are, but not limited to, dike width, dike vertical length, magma viscosity and temperature, and density differences. Because dikes essentially have a planar sheet geometry, the width is crucial to allow a sufficient amount of magma to flow rapidly. It is necessary for the magma to ascend rapidly through these narrow channels because as magma ascends, the temperature decreases due to the temperature difference between the magma and surrounding host rock. Without a sufficient width, a flux of magma will solidify rather than ascend. The temperature differences also affect the viscosity of the magma, which increases exponentially with cooling. A low viscosity magma is ideal for magma propagation through vertical dike ascent (Petford et al., 1993). The density difference between the ascending magma and the host rock also relate to magma ascent rate and the magma driving pressure. The greater the density contrast between the ascending magma and the host rock, the more pressure exerted on the driving pressure of the ascending magma that allows rapid ascent through the crust before magma solidification (Petford et al., 1993).

While dikes may eventually reach the surface, many are arrested at depth. According to Gudmundsson (1990, 2011), when a dike meets a stress barrier, such as layers with greater horizontal compressive stress than vertical compressive stress, three likely scenarios can occur: (1) the dike will become arrested at the barrier, (2) the dike will penetrate the contact, or (3) the dike will be deflected at the contact (Fig. 3). Field observations demonstrate all three scenarios to be well known, however the third scenario (Fig. 3C & 3D) is representative of the initial stages of sill formation.

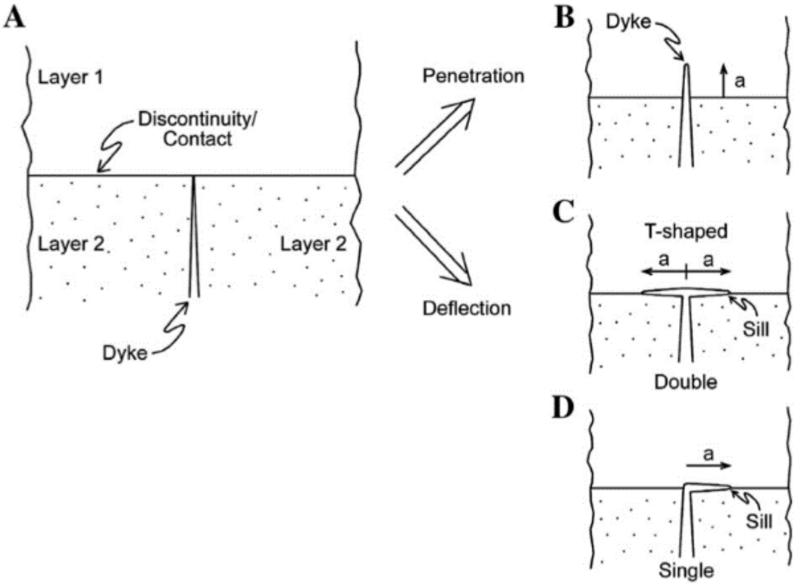

Figure 3. Scenarios for when a dike meets a discontinuity. **(A)** dikes become arrested, **(B)** dike penetrates the layer above the contact or dike is deflected to form a double **(C)** or single **(D)** sill (Gudmundsson, 2011; Hutchinson, 1996).

2.2 Sill Formation Through Lateral Emplacement of Magma

Once a dike is arrested, vertical ascent ceases, and the lateral movement of magma commences. According to Menand (2011), the lateral flow of magma is affected by multiple factors such as: buoyancy controls, rheology, stress controls, and rigidity anisotropy. It was initially thought (e.g. Gilbert (1877), Corry (1988)) that neutral buoyancy was the main factor that led to emplacement of magma at a specific depth in the crust. This follows from the assumption that the density of the ascending magma has reached the same density of the surrounding host rock. Later work showed that the idea of neutral buoyancy contradicts field observations (Johnson and Pollard, 1973), and that granitic magmas do not achieve neutral buoyancy in the shallow crust (Vigneresse and Clemens, 2000).

Rheology contrast controls and stress controls are two other mechanisms that Menand (2011) suggested as factors for lateral movement of magma. Rheology contrast controls refer to the mechanical differences between relatively brittle and ductile layers to allow dike arrest and promote lateral propagation. Stress controls refer to the tectonic environment where dikes may become arrested due to the transition from a favored extensional environment to a less favorable compressional environment.

Lastly, Menand (2011) refers to a final mechanism of rigidity anisotropy control. This refers to the difference in competence of two host rock layers and would allow magma to intrude between them. Experimental investigations have demonstrated that a dike will typically favor deflection into a sill if the overlying host rock layer is more competent that the underlying layer (Kavanagh, 2006; Gudmundsson, 2011). Menand (2011) suggests that this is likely the most dominant control of the four mechanisms.

2.3 Lateral Termination and Vertical Thickening

As discussed, sills form from arrested dikes that propagate laterally between the rigidity anisotropy contrasts of two host rock layers (Menand, 2011). Early models suggested the vertical inflation of sills to form laccoliths begins when a sill reaches a critical lateral extent, allowing inflation into a laccolith (Johnson and Pollard, 1973; Pollard and Johnson, 1973). With increasing evidence that larger igneous intrusions are formed through an amalgamation of multiple magma pulses, our understanding on how laccoliths grow are evolving.

Once a sill has solidified it can provide a favorable rigidity anisotropy for the emplacement of other sills (Menand, 2008). Based on field observations (see the Case Studies section), many laccoliths appear to grow vertically by the stacking of additional sills while the lateral extent of the laccolith is comparable to the initial sill. The overall thickness of the laccolith is the cumulative thickness of all sills within the laccolithic body. The stacking of these additional sills can occur in multiple fashions including over-accretion, under-accretion, or mid-accretion (Horsman et al., 2005, 2006; Morgan et al., 2005; Menand, 2008).

3. Magmatism in the Shallow Crust: Laccolith Formation

This section provides information about laccoliths, including some background information, laccolith geometry, and timescale construction.

Additionally, several case studies address the growth of laccoliths and other sheet-like igneous intrusions in the upper crust using geological, geochronological, and geophysical data, and analogue models. These case studies focus on different laccolithic intrusions that provide details on the time scale for laccolith formation, how laccoliths can form from amalgamated lobes and sheets, and the complexity of their construction over time.

3.1 Evolving Model for Laccolith Assembly

The initial interpretations of a laccolith provided by Gilbert (1877), Hunt et al. (1953), Corry (1988), and Jackson and Pollard (1988, 1990) are essential building blocks for defining the term laccolith. In much recent years, these building blocks have been essential, but collective evidence has changed our views on how these laccoliths are emplaced. Although Gilbert's (1877) interpretations were upheld by recent data, his concept of a laccolith is regarded as single contiguous liquid body. We now know that many igneous intrusions of various spatial scales, including laccoliths, can form through sequential injections of separate magma pulses. This does not preclude an intrusion forming from a single magma pulse, however, in larger volume intrusions, supporting evidence shows that laccoliths form through stacked sheets or an amalgamation of multiple pulses (Cruden et al., 2001; Coleman et al., 2004; Glazner et al., 2004; de Saint Blanquet et al., 2006, 2011; Michel et al., 2008; Morgan et al., 2008; Broda, 2014; Ward, 2014; Maurer, 2015; Thorton, 2015; Horsman et al. 2005, 2010, 2018) Through this succession of pulsed assembly, a laccolith can be defined as an igneous intrusion with a flat base, a convex-up roof that is formed from one or more amalgamated pulses of magma, and generally emplaced at a crustal depth of 3 km or less (Gilbert, 1877; Johnson and Pollard, 1973; Corry, 1988).

3.2 What is a Magma Pulse?

A magma pulse can be defined as a single injection of magma that contributes to the overall construction of an igneous intrusion. However, as discussed in the introduction, pulsed construction is scale and time dependent. For the purpose of this research, we are concerned with the individual stacked sheets that compose a laccolithic intrusion. These stacked sheets can be composed of multiple component pulses themselves (Fig. 4), however, at the scale of a laccolithic intrusion, these individual pulses may be difficult to distinguish. So, for this research I use the term “magma pulse” at a coarser scale, to distinguish on a first order, the number of pulses that contribute to the construction of a laccolithic intrusion.

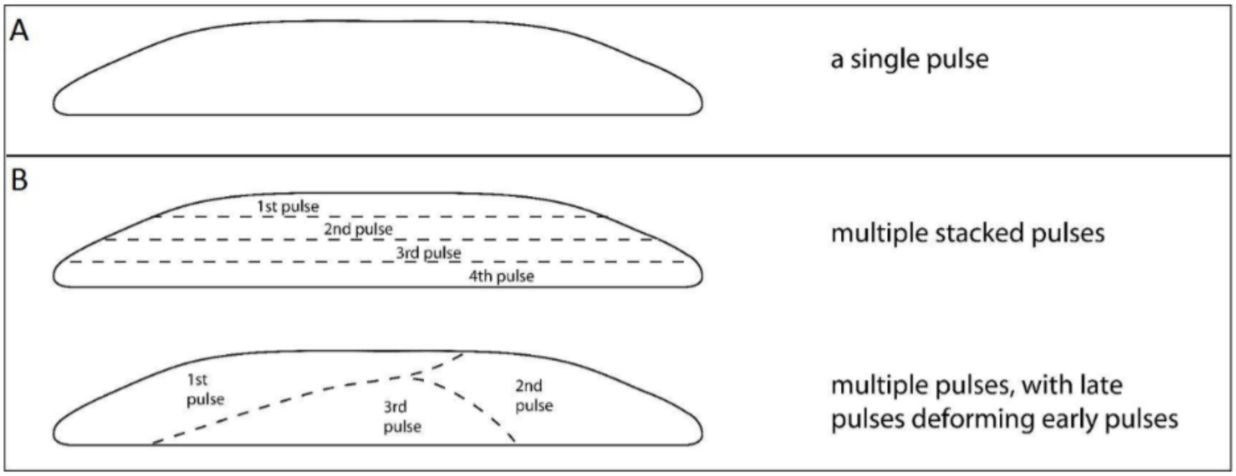

Figure 4. Diagram showing pulsed assembly through multiple magma pulses. Pulses can be singular or sequential. If pulses are sequential, there is no general pattern for how they are injected. Pulses can be stacked or amalgamated. Revised from Horsman et al. (2006).

3.3 Laccolith Geometry Upon Emplacement

As discussed above, there is no single means of emplacement for a laccolith. However, laccoliths are described by their overall geometry after emplacement. A laccolith generally has a flat base, steep sides, and an arched to flat roof (Gilbert, 1877; Johnson & Pollard, 1973; Corry, 1988). They tend to have a flat base due to lateral propagation concordantly between two sedimentary strata. As for their steep sides and roof shape, Gilbert (1877) and Koch et al. (1981) both predicted that the length of an intrusion should scale with the thickness of the overburden.

To attempt to quantify the overall geometry of a laccolith, McCaffrey & Petford (1997) suggest a scale invariant relationship between the length (*L*) and the thickness (*T*) of tabular laccoliths by using an empirical power-law relationship:

$$(2) \qquad T = \mathrm{b}L^{\mathrm{a}}.$$

T represents the thickness of the intrusion, *b* is a constant (y-intercept), *L* is the length of the intrusion, and *a* is the power-law exponent (slope) (McCafrey & Petford, 1997). Using the aspect ratio of *L*/*T* of known intrusions, Cruden et al. (2017) plotted on a log (*L*) versus log (*T*) scale dimensional data for various size/shaped plutons ranging from dikes to laccoliths (Fig. 5). The solid and dashed lines on the graph represent a range of power scaling curves that demonstrate the bifurcation between laccoliths and other smaller bodied intrusions. The exponent *a* distinguishes between the following three different growth behaviors in relation to the aspect ratio *L/T* of a tabular laccolith. (1) If $a=1$, the aspect ratio is equal, then the length and thickness are equal, (2) $a < 1$, the aspect ratio increases, then lateral spreading is dominant, or (3) $a > 1$, the aspect ratio decreases, then uplifting (vertical inflation) is dominant (McCafrey & Petford, 1997; Cruden & Bunger, 2010; Cruden et al., 2017). Laccoliths generally fall along a fit line of approximately a = 1.5, while other smaller bodied intrusions fall along a fit line of approximately a = 0.5 and are more sill-like in geometry.

Small intrusions and mafic sills tend to follow the same growth path (Fig. 4). Dimensional data from various sources (Cruden & Bunger, 2010; Cruden et al. 2017) demonstrate that large mafic sills and other smaller bodied plutons favor lateral spreading with $a < 1$. However, it is apparent that the dimensional data for laccoliths (generally intermediate to felsic composition) show a separation around L of 100 – 1000 m, and favor uplifting (vertical inflation) over horizontal spreading because the slope (a) is greater than 1 (Cruden & Bunger, 2010; Cruden et al. 2017). This suggests that laccoliths begin to follow a different growth path that contributes to a distinct geometry.

Additionally, with the availability of three-dimensional data, Cruden et al. (2017) also proposed a power-law relationship between the thickness (T) of an intrusion in meters and the total rock volume of the intrusion (V) with the following equation:

$$(3) \qquad T = dV^c,$$

where d is a constant, V is the total rock volume in cubic meterss, and c is the power-law constant. Cruden et al. (2017) graphed this power-law relationship using the same intrusions from the previous graph to demonstrate an approximation of volume to thickness ratios for various bodied plutons (Fig. 6). The resulting values produced should be viewed as an approximation based on the assumption that horizontal tabular intrusions are disk shaped (Cruden et al. 2017). This allows for a reasonable first-order calculation for various bodied intrusions. Laccoliths show a separation between volume values of 1 x 10^7 to 1 x 10^8 m^3 (0.01 – 0.1 km^3) and between slopes of approximately $c = 0.3$ to 0.4 (Cruden & Bunger, 2010; Cruden et al. 2017).

Both plots reveal important differences between different intrusion geometries. Laccoliths appear to share a similar range of thickness values with sills, but laccoliths generally are one order of magnitude smaller than sills in length and one to two orders of magnitude smaller in total rock volume than sills.

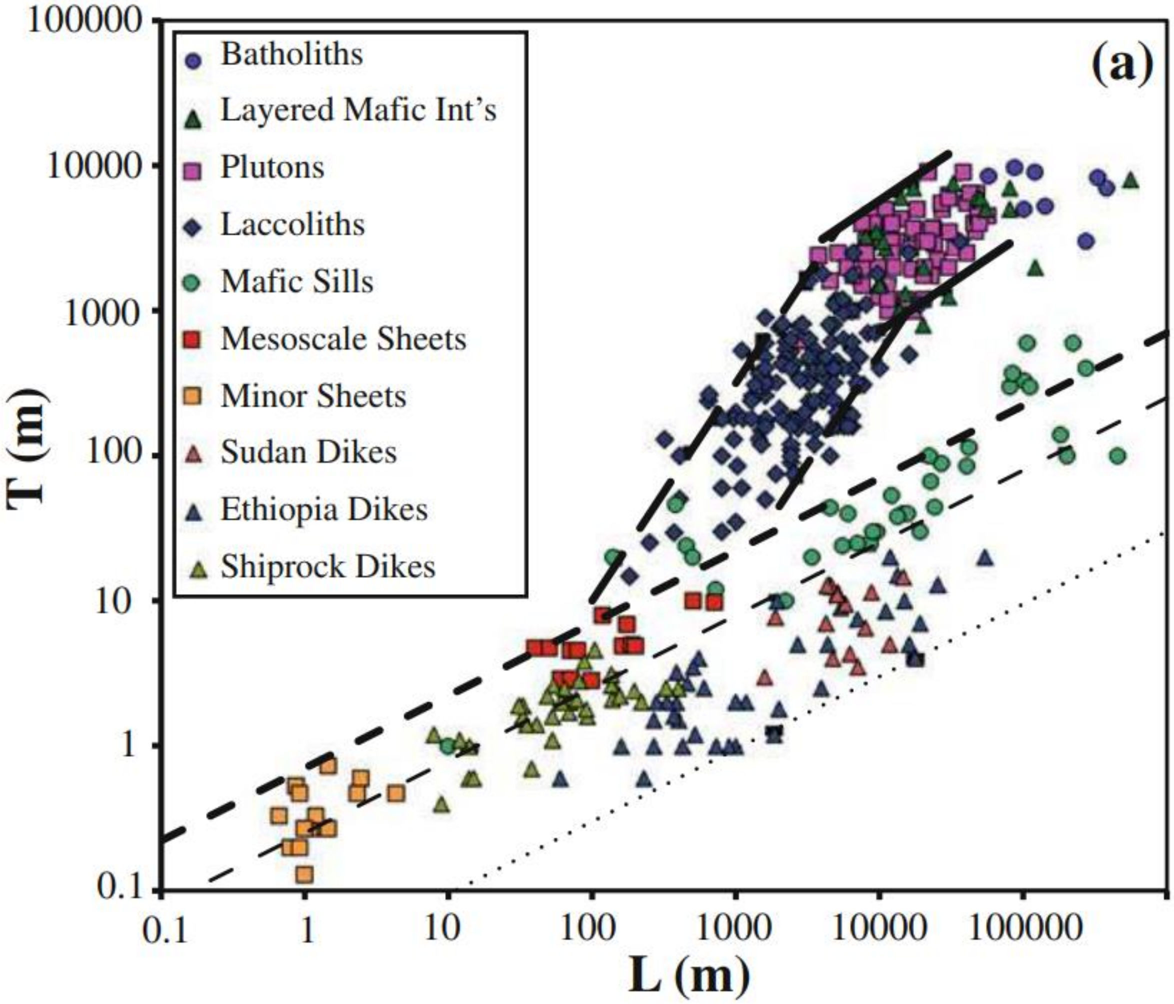

Figure 5. Log thickness (T) versus Log length (L) of dimensional data for dikes, sills, and laccoliths from various sources. Solid and dashed lines are bounding curves for different intrusion types (Cruden et al., 2017).

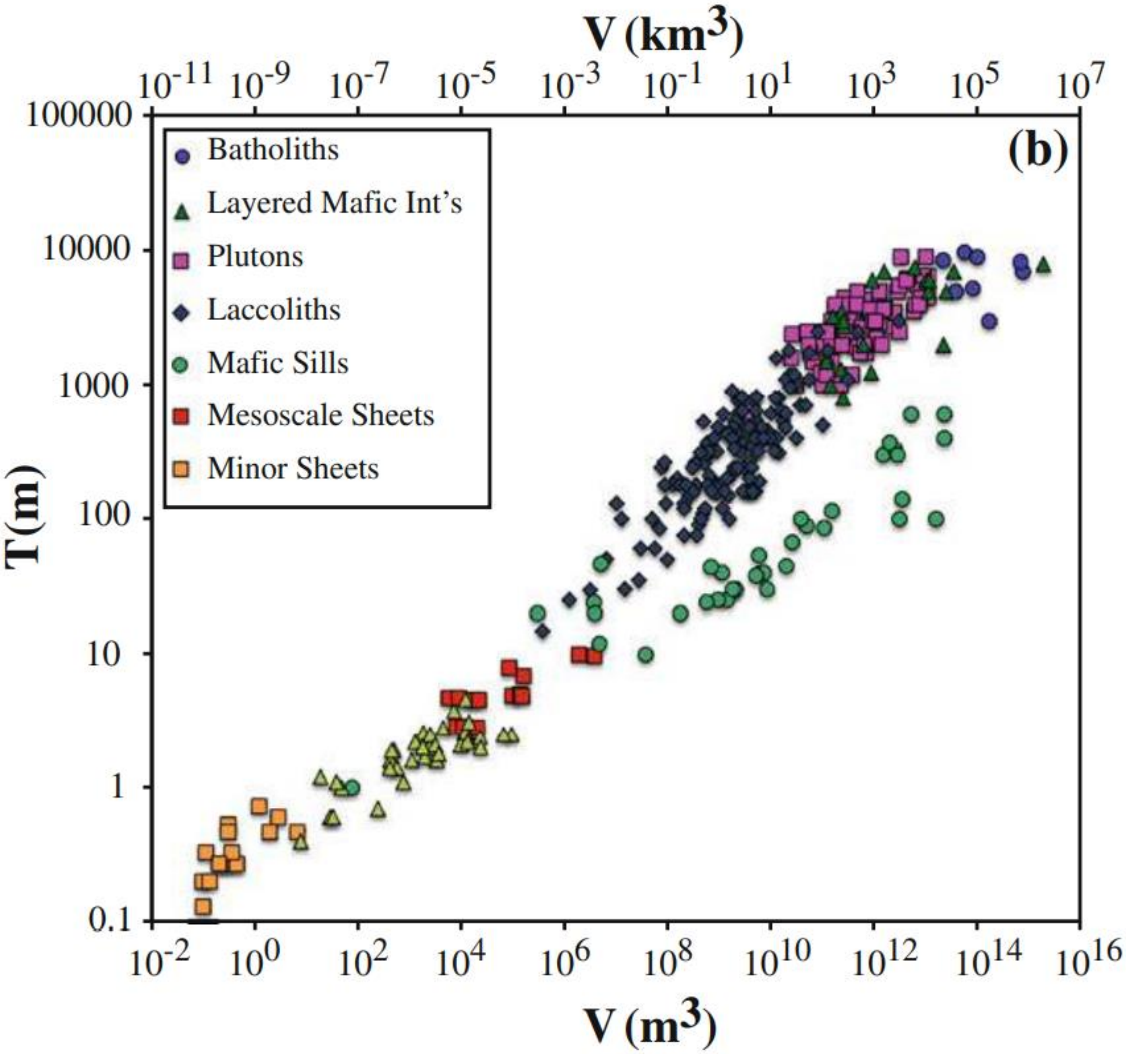

Figure 6. Log thickness (T) versus Log volume (V) of dimensional data for dikes, sills, and laccoliths from various sources. (Cruden et al., 2017).

3.4 Timescale Construction of Igneous Intrusions

Saint Blanquat et al. (2011) demonstrated that the duration of pluton construction correlates, on a first order, to the volume of a pluton. The larger the pluton, the longer the duration of construction. Using a compilation of various size plutons, they calculated estimated magma flux rates (Fig. 7). Data were sorted based on tectonic setting (active and inactive plutons). This model provided some of the following interpretations: (1) a positive correlation between duration and volume for pluton construction; (2) no correlation between the tectonic setting and the duration and rate of pluton construction; (3) the annual magma flux for pluton construction covered three orders of magnitude from 10^{-1} to 10^{-4} km^3 yr^{-1} and; (4) a significant correlation exists between data for modern systems and ancient systems.

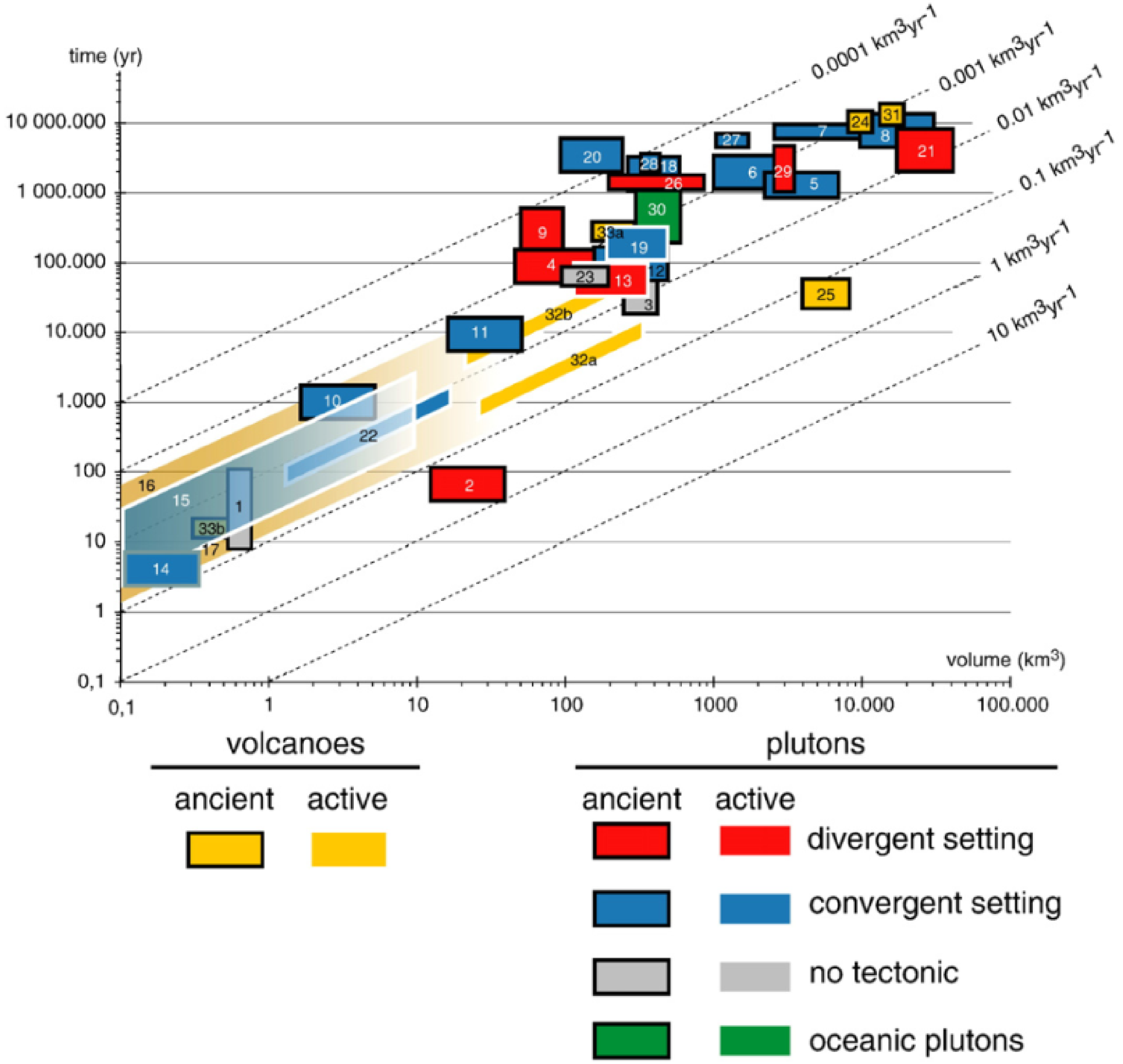

Figure 7. Compilation of duration and rates of pluton construction for various pluton sizes for both active and ancient systems (Saint Blanquat et al. 2011).

4. Case Studies

4.1 Torres del Paine Laccolith

The Torres del Paine laccolith of Chile (Fig. 7) is a part of a lineament of intrusive bodies east of the Patagonian Batholith. This Neogene laccolith has a total igneous rock volume 88 km^3 and intrudes concordant sedimentary host rock above and below. The laccolith is oriented from west to east that extends approximately 2 – 4 km (Putlitz et al., 2001). The Torres del Paine laccolith is an exceptional case because of its spectacular exposure and clear construction from multiple magma bodies. Each sheet that constructs the Torres del Paine laccolith is clearly recognizable in the field and are compositionally distinct.

Recent work by Michel et al. (2008), and additional work performed by Leuthold et al. (2012), used zircon U-Pb dating, geochemistry, and field observations to study the laccolith. They found that this laccolith was built from four basal mafic sills that are overlain by an additional three granitic units. The granitic units were emplaced at approximately 2 – 3 km depth and each unit was successively added by under-accretion over a time scale of 121 ka with a total igneous rock volume of 80 km^3 (Fig. 8). The mafic units were emplaced below granite unit III by over-accretion over a timescale of 41 ka with a total igneous rock volume of 7 km^3 (Fig. 9). Overall, the Torres del Paine intrusive complex was built on a timescale of approximately 162 ± 11 ka, from 12.593 ± 0.009 Ma to 12.431 ± 0.006 Ma (Leuthold et al. 2012). Leuthold et al., (2012) also determined that the average growth rate for the Torres del Paine laccolith was 0.0005 $km^3\ y^{-1}$ with an overall igneous rock volume of ~88 km^3 (including in total, the granitic units, mafic complex, and feeder zone).

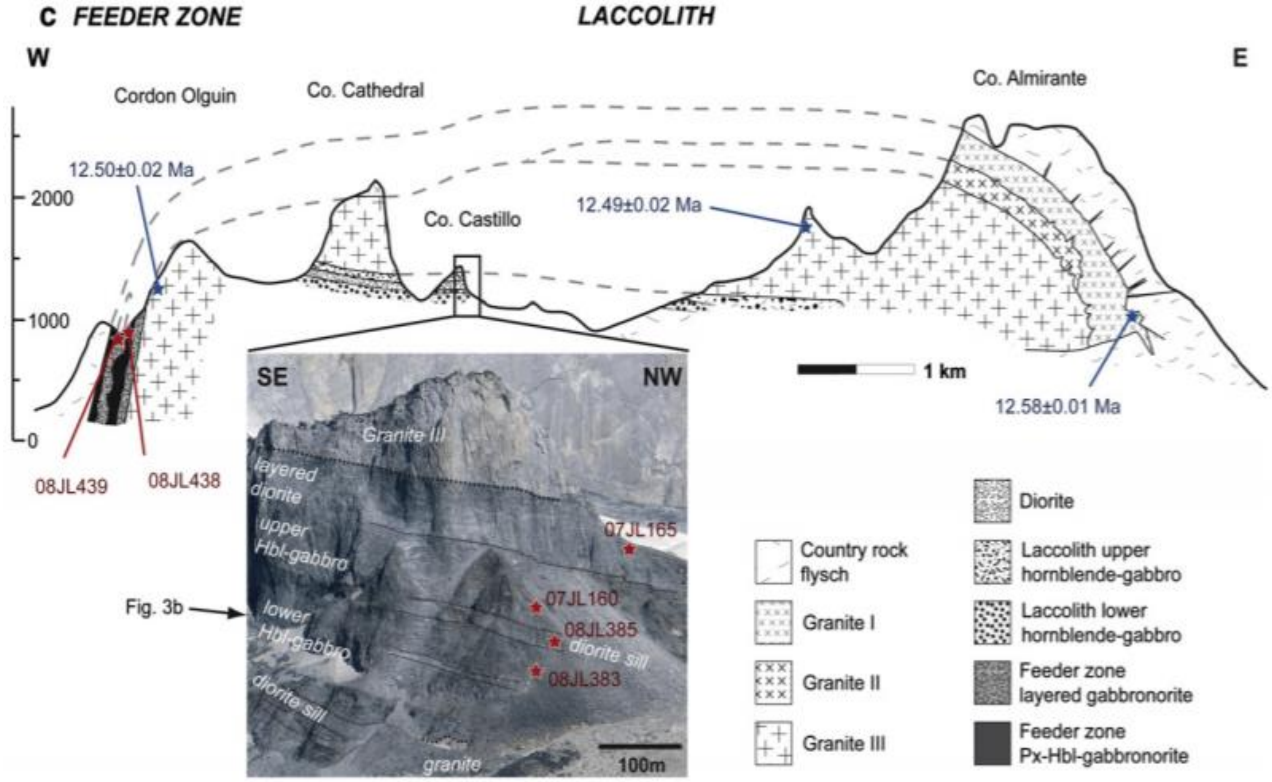

Figure 8. The Torres del Paine intrusive complex. West to East cross-section demonstrating the three different granitic sheets that make up the laccolithic body. Ages have been determined for each granite unit and are noted with blue arrows (Leuthold et al., 2012).

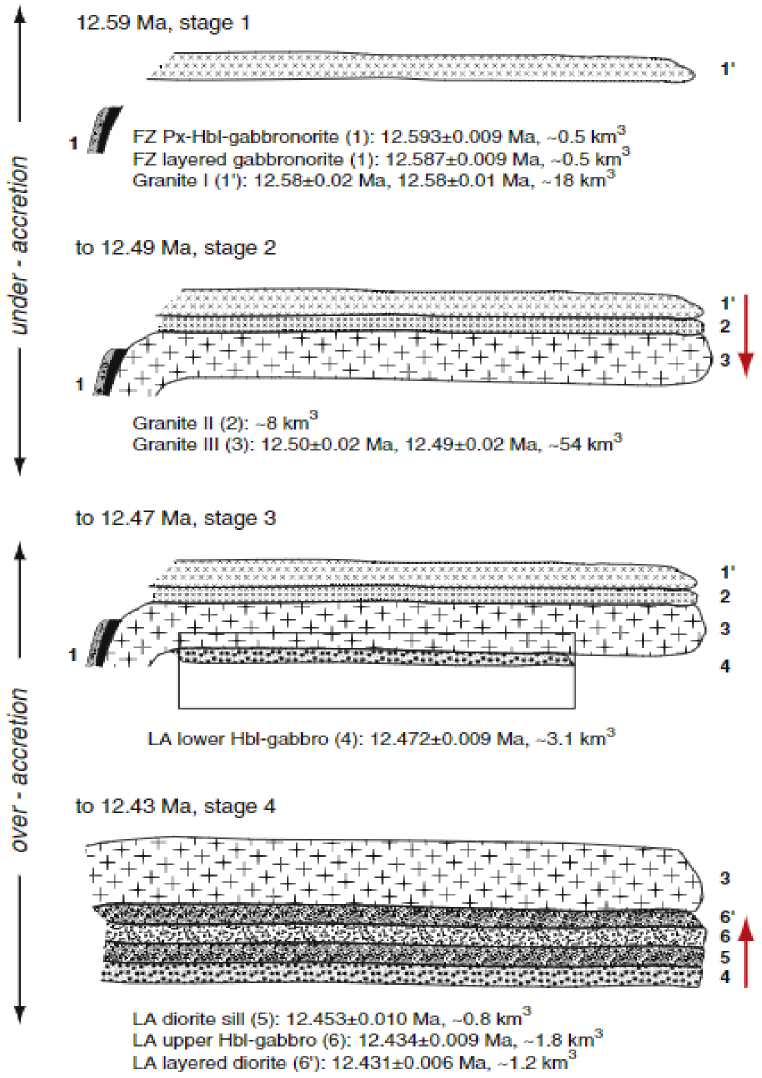

Figure 9. Schematic diagram showing emplacement of the seven units of the Torres del Paine intrusive complex including geochronological data and mode of emplacement. (Leuthold et al., 2012).

4.2 Elba Island Laccoliths

The Elba island laccoliths are located at the northern end of the Tyrrhenian Sea in Tuscany, Italy. These laccoliths were emplaced at depths between 2 – 3 km (Rocchi et al., 2010) and consist of Micoene granite porphyry sheets that formed Christmas-tree laccoliths over a time span of approximately 1 million years (Rocchi et al., 2010). A Christmas-tree laccolith is a term to describe a suite of intrusions that are emplaced between various sedimentary horizons at different depths. The intrusions are generally larger with depth and progress upward to smaller intrusions, so the overall geometry appears like that of a Christmas tree in cross-section. The two main laccoliths are the Portoferraio laccolith (four sheets) and the San Martino laccolith (three sheets) (Rocchi et al., 2002). The intrusive sheets of these laccoliths range from 50 to 700 m thick, with diameters between 1.6 and 10 km, and an approximate total igneous rock volume of 37 km^3 (Fig. 10).

To investigate the construction history of the laccolith, Rocchi et al. (2002, 2010) calculated the dimensional parameters for the main Portoferraio and the San Martino intrusions and component sheets using an empirical power-law ($T = bL^a$, as discussed in the introduction section of this paper). The sheets of individual laccoliths are thought to be only a portion of a complete laccolith, thus calculating separately, the length and thickness ratios for individual sheets and the cumulative thickness of sheets is crucial (Westerman et al. 2004). Using the scale-invariant distribution of McCaffrey & Petford (1997), the parameter data was plotted on a log T vs. log L scale (Fig. 11) for the Portoferraio and the San Martino Laccolith (Westerman et al. 2004). The resulting data can be interpreted as evidence for the vertical inflation stage of laccolith growth through sheet/ stacking (Rocchi et al., 2002). The cumulative thickness of the Portoferraio and San Martino laccoliths fit the power-law line for pluton dimensions of

McCaffrey and Petford (1997). This suggests the distinct Christmas-tree appearance of these two laccoliths can be attributed to failure of magma to coalesce into a single laccolithic body or pluton (Rocchi et al., 2002; Westerman et al., 2004; Rocchi et al., 2010). This then suggests that laccoliths and plutons can form through an amalgamation of sheet-like bodies (Westerman et al. 2004).

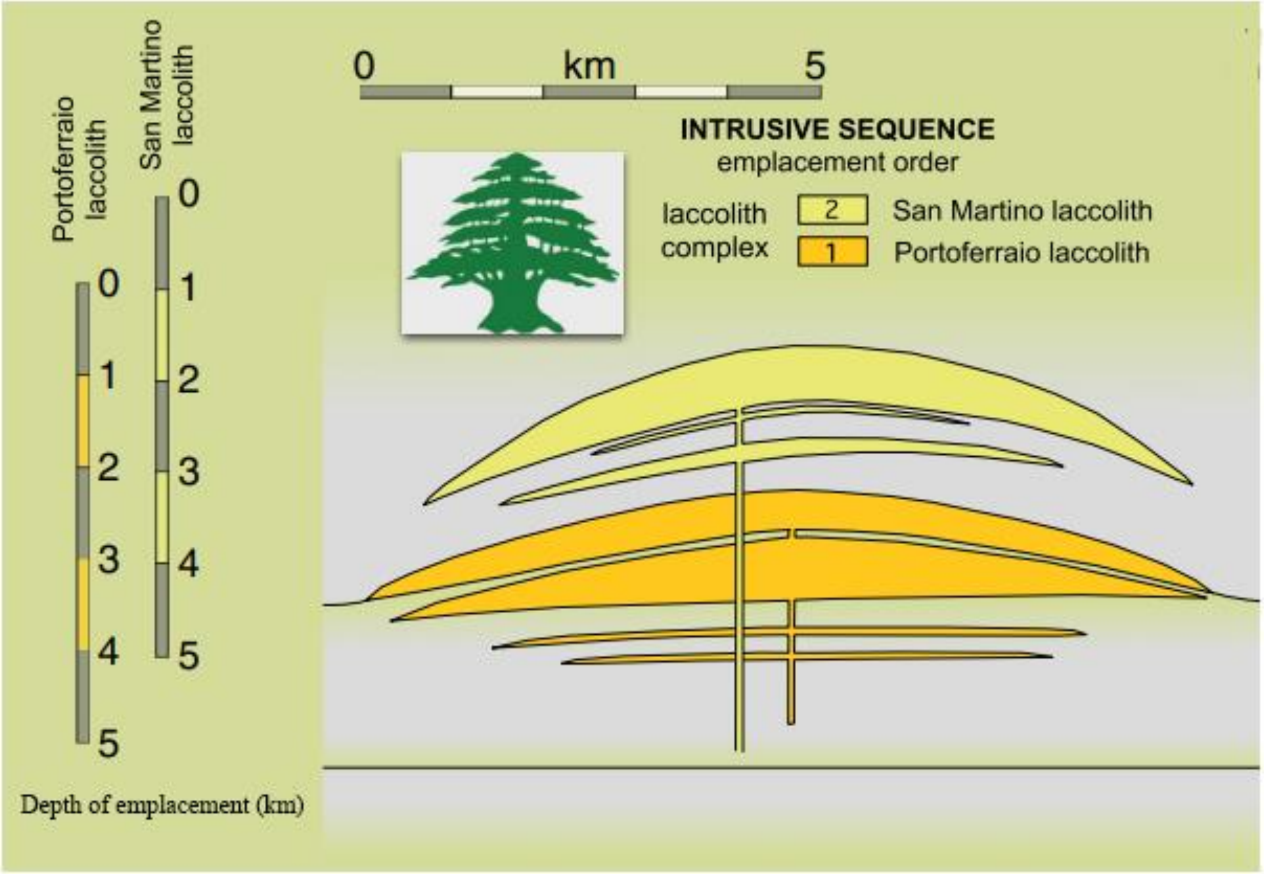

Figure 10. Schematic cross-sectional diagram of the San Martin laccolith and the Portoferraio laccolith demonstrating the Christmas-tree geometry. Depth of emplacement and diameter of each laccolith can be noted (modified from Rocchi et al., 2010)

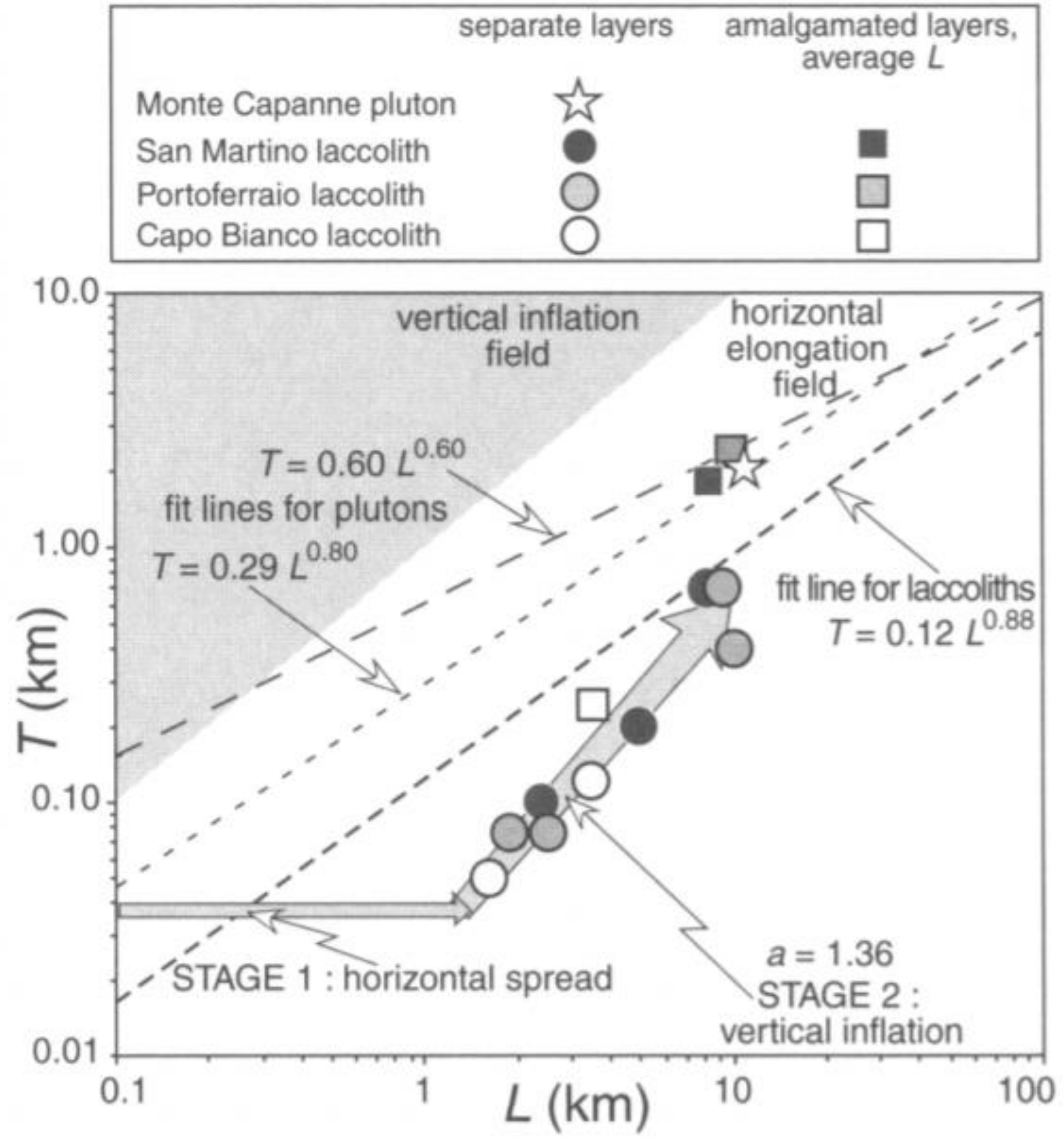

Figure 11. Scale-invariant distribution of laccolith and pluton shape of McCaffrey & Petford (1997) with dimensional data for the San Martino laccolith and Portoferraio laccolith. The Capo Bianco laccolith and Monte Capanne pluton are shown for reference (Westerman et al. 2004).

4.3 Erland Volcano Plumbing System

The Erland shield volcano is located in the northeastern Faroe-Shetland Basin (Fig. 12A) and is currently overlain by approximately 1100 m of sedimentary strata. The Erland volcano was active, along with many other volcanoes, between 62 and 55 Ma along the pre-rift northeastern Atlantic margin (Ritchie et al., 2011). Recent work by Walker et al. (2020), used 3-D seismic data and gravity modeling to study intrusions of the underlying plumbing system of the Erland volcano along with the volcano edifice. Their study allowed for examination of an entire multicomponent plumbing system for an ancient volcanic system.

Seismic data revealed a plumbing system that comprises a large laccolithic body with hundreds of radiating sills (Fig. 12B). The sills are saucer shaped and are distributed around and away from the main laccolithic body. The main body of the laccolithic intrusion is approximately 15 km in diameter with a total igneous rock volume of approximately 200 km^3. The main intrusive body is interpreted as a large laccolithic complex with a network of amalgamated intrusions with hundreds of radially distributed sills. These findings are similar to geometries describes in previous work from the Henry Mountains (Jackson and Pollard, 1988) and support a similar Christmas-tree geometry like that of the Elba Island laccolith (Fig. 13).

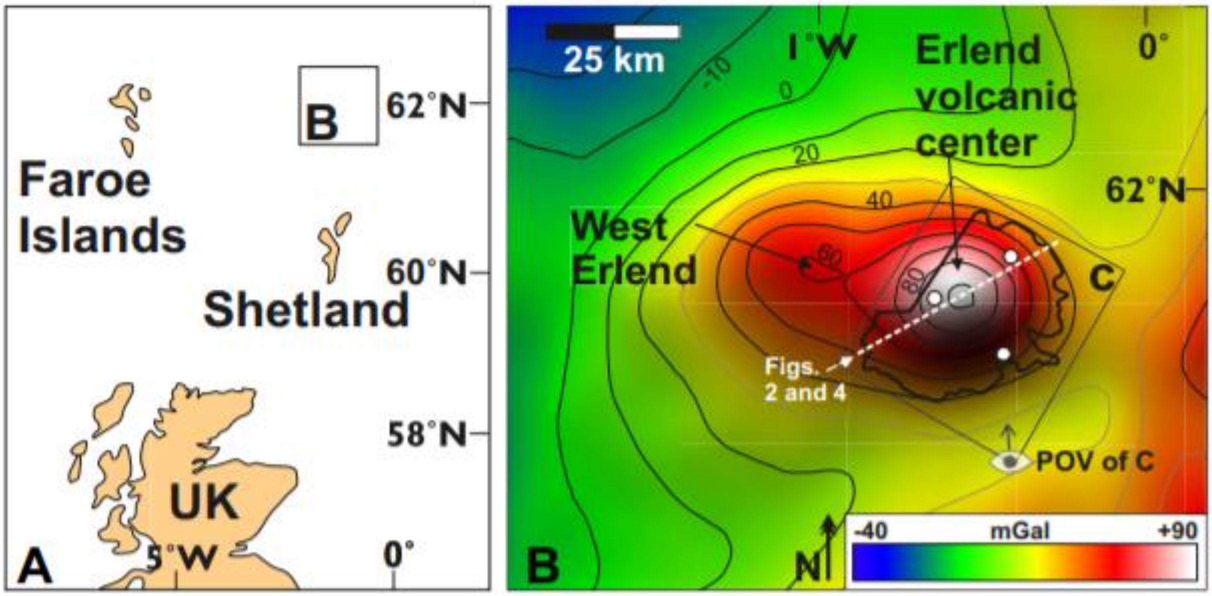

Figure 12A. A. Location map of study area located in the Faroe-Shetland Basin. **B.** Free-air gravity anomoly over Erland volcano (Walker et.al, 2020)

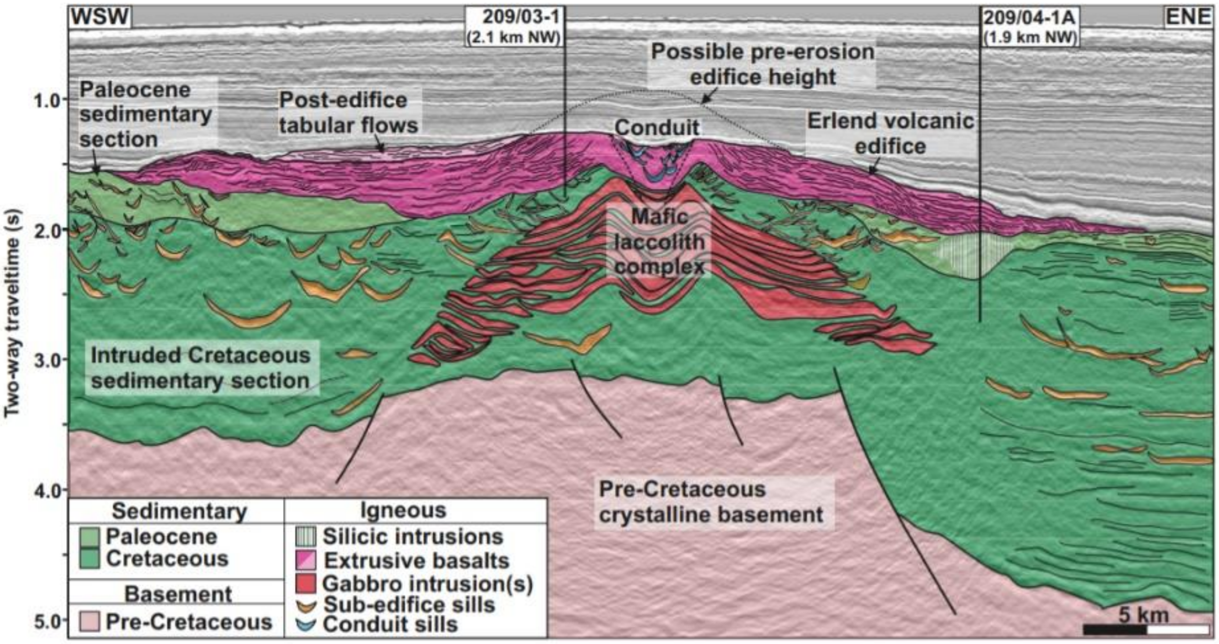

Figure 12B. Seismic cross section of the Erland volcano demonstrating volcano edifice and underlying laccolithic complex with associated sills (Walker et al., 2020).

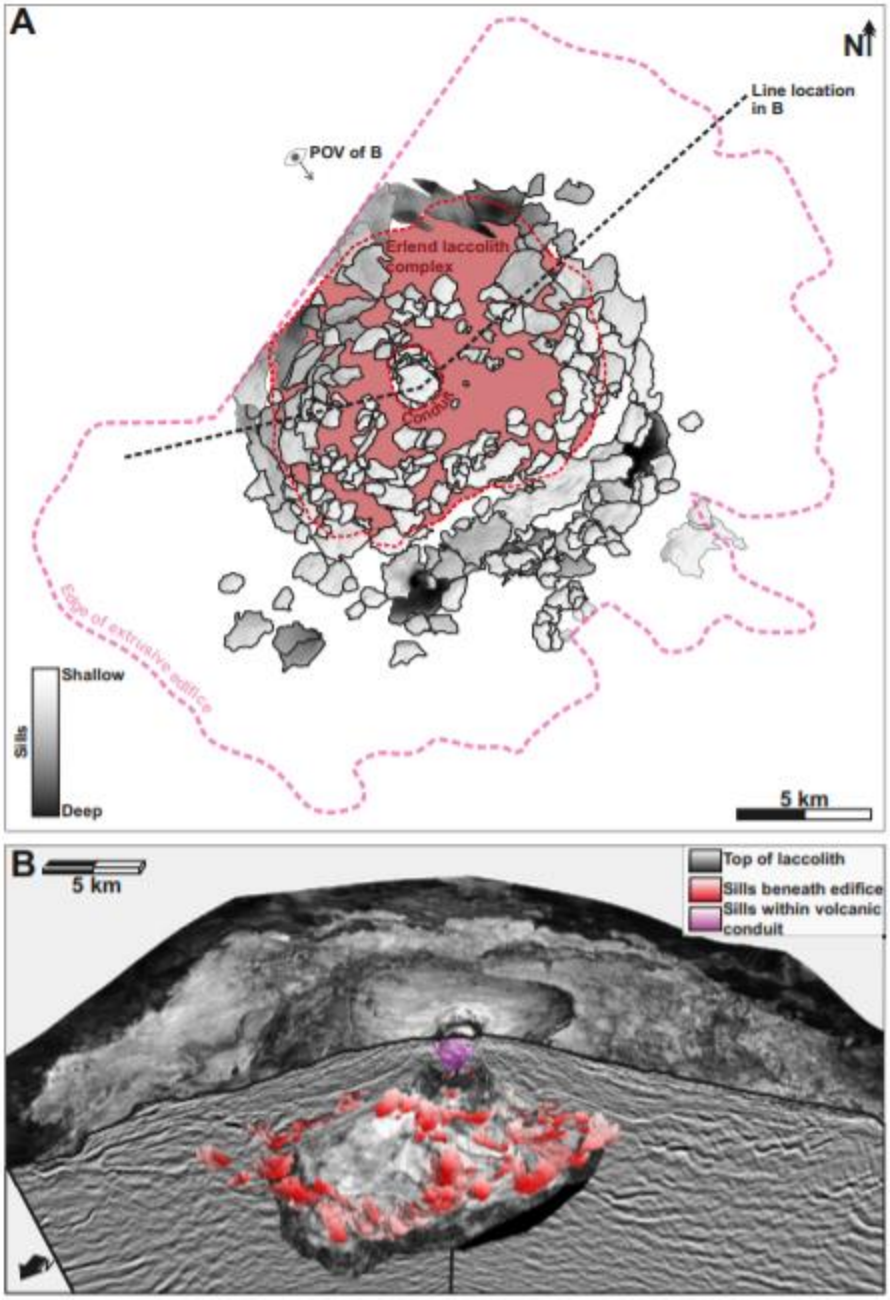

Figure 13 A. Map view of Erlend volcano plumbing system with edifice outlined in pink dashed line. All mapped out sills from seismic data are shown radially distributed around main body of the laccolithic complex. **B.** 3-D rendering of seismic data showing sill distribution and laccolith body.

4.4 North Rockall Trough

The North Rockall Trough is a sedimentary basin that separates the Rockall Plateau (offshore Ireland and Scotland) from the northwestern part of the European continental margin. During the late Cretaceous to early Eocene, extensive magmatic activity occurred as doleritic sill complexes along the axis of the basin and smaller intrusions at various locations throughout the basin (Mussett et al. 1988; Upton 1988; Hitchen and Ritchie 1993).

Thomson & Hutton (2004) used 3D seismic reflection data to observe the complexity of the North Rockall sill complexes and interpret sill geometries, magma flow patterns, and sill growth histories. Based on their observations, they were able to determine two different types of sill geometries for these sill complexes: bilaterally symmetrical sills and radially symmetrical sills. Bilaterally symmetrical sills have a trough-like geometry and radially symmetrical sills have an inner saucer-like geometry with curved inclined sheets connecting to an outer rim. Both sill geometries generally have similar internal architecture and morphology (lobes and branching) but differ in the way they are fed from their magma source. The bilaterally symmetrical sills are fed from magma diverted from a conduit feeding an overlying volcano. The radially symmetrical sills are fed independently from an underlying feeder source.

Thomson & Hutton (2004) also observed that within these sill complexes, the 3D seismic data demonstrated a dendritic network of lobes radiating from the central portion of the sill complex outward towards the complex margins (Fig. 14). The branching nature of primary magma tubes from the central sill, allowed secondary magma tubes to form and branch from the primary flow tubes, creating a hierarchy of magma flow networks within the sill complex. Similar geometries were noted by Pollard et al. (1975) as “finger-like” lobes that coalesce into sheets (Fig. 15).

Thomson and Hutton (2004) concluded that many of their findings supported earlier work by Pollard and Johnson (1973) for Henry Mountains intrusions and Burger et al. (1981) for the Karoo intrusions of South Africa. Specifically they concluded: (1) for sills, magma flow may occur in channels; (2) each of the radially symmetrical sills complexes are fed from a central feeder beneath the sill; (3) sills grow from the center and propagate outward. Their observations and conclusions demonstrate the complexity of sill growth and how branching of magma flow networks promote lobate growth. These lobes can further coalesce into a contiguous sheet as demonstrated with the sill complexes of the North Rockall Trough.

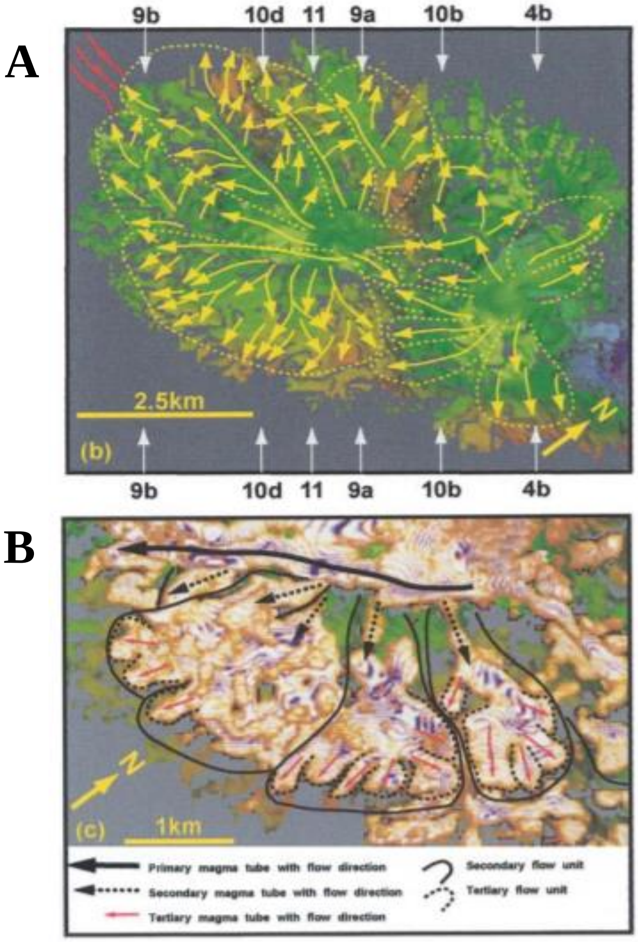

Figure 14. **A.** Rendered pattern of amplitude data to illustrate the branching nature of sill complexes, and how lobes of magma coalesce and form additional lobes. A. Yellow arrows indicate the inferred position of magma tubes and flow direction. **B.** Demonstrates a primary magma tube that flows SW that feeds secondary magma tubes flowing to the South. These lobes coalesce to form amalgamated sheet intrusions (Thomson & Hutton, 2004).

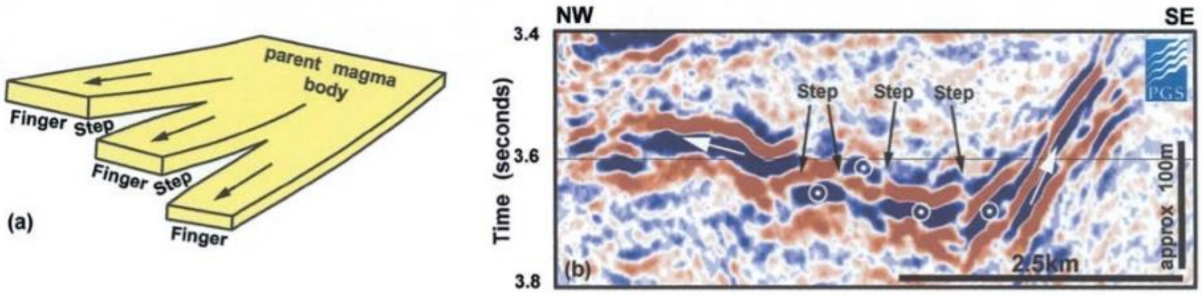

Figure 15. a. Illustration of finger-like geometry and connection to parent sill **b.** seismic data of finger geometry with flow direction depicted by white circles flowing normal to page (Thomson & Hutton, 2004).

4.5 Analogue models

Kavanagh et al. (2006) modeled laccolith formation using dyed water injected into gelatin molds. The water was an analogue for magma and the gelatin for the surrounding host rock. They concluded that under hydrostatic conditions, sill formation requires a presence of layers with rigidity contrasts. Specifically, a competent layer must overlie a less competent layer.

Expanding on the work of Kavanagh et al. (2006), Currier and Marsh (2015) used two separate analogue models to test different emplacement styles with and without solidification of the magma analogue. They used water (no solidification present during the experiment) and liquid paraffin wax (solidifies as it cools during the experiment) as magma analogues and layers of clear gelatin with different densities to represent the host rock. Using video snapshots, they were able to map growth of the analogue intrusions at one-second intervals to study a progressive construction (Fig. 16A).

In the Currier and Marsh (2015) experiments, the water intrusion models show a consistent lateral spreading that is relatively smooth and simple. In contrast, the paraffin wax intrusion models show more complexity in their morphology. The wax models demonstrate a radial growth pattern from the source of injection (feeder zone). Currier and Marsh (2015) noted that because of solidification present in the wax models (not present in water models), that the propagation direction of the wax varied considerably in between time steps (Fig. 17) and would at times show irregular growth patterns (less semi-circular). However, continued growth from additional injections generally resolved the irregular growth patterns and the intrusion trending back towards a semi-circular shape. This allowed Currier and Marsh (2015) to infer that the overall geometry of a radially symmetrical modelled laccolith is a product of multiple lobes that coalesce to form a cumulation of thin sheets.

Of the two analogs, the wax intrusions are most comparable to the overall characteristic shape of a laccolith with a relatively flat base and a convex roof that can be seen in cross-sectional view (Fig. 16B). Currier and Marsh (2015) concluded that the solidification of magma (paraffin wax analogue) at the intrusions margins allows for thicker growth of the intrusion. They also concluded that the growth of intrusions from pulsed assembly occurs over various timescales and this is a significant factor to take into consideration.

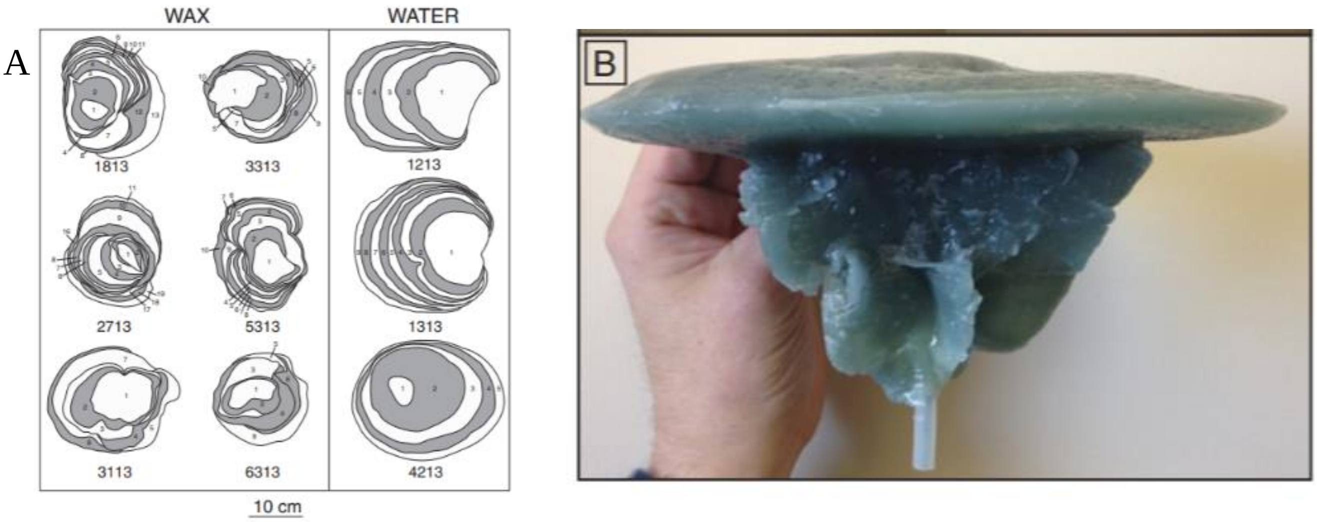

Figure 16. A. Snapshots of growth contours at 1 second intervals for six wax models and three water models **B.** Physical result of the wax injection models showing the overall characteristic shape of a modelled laccolith. (Currier & Marsh, 2015)

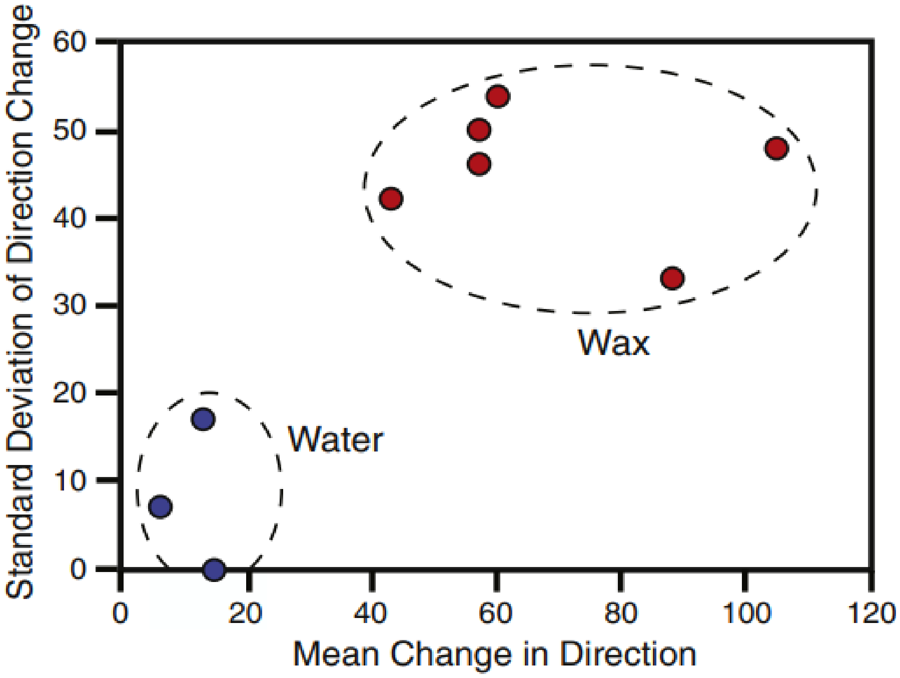

Figure 17. Statistical data for directional propagation of water and wax models. Demonstrates that wax models propagate in various directions and water models propagate relatively in the same direction.

5. Geologic Setting

5.1 Colorado Plateau

The Colorado Plateau is a geologic province that extends over 350,000 km^2 in the North American Cordillera (Fig. 18) (Hunt, 1956), bounded by the Rocky Mountain orogen, the Basin and Range province, the Rio Grande Rift province, and the Mogollon Rim (Trexler, 2014). It consists of 45 to 50 km thick cratonic crust (Thompson and Zoback, 1979) largely composed of Phanerozoic sedimentary rock deposited on top of Precambrian basement rock (Fig. 19). Although much of the North American Cordillera underwent intense deformation several times during the Phanerozoic, the Colorado Plateau remained relatively intact and stable. This may be due to earlier crustal thickening beneath the Colorado Plateau (Thompson and Zoback, 1979; Nelson and Davidson, 1992; Flowers, 2010).

A major late Paleogene magmatic event affected much of the Cordillera. This magmatism was significantly more voluminous at the margins of the Colorado Plateau than on it (Armstrong & Ward, 1991). However, the Henry, La Sal, and the Abajo Mountains (32 – 23 Ma, Nelson et al.., 1992), were emplaced as laccolithic intrusive complexes withing the Colorado Plateau (Gilbert, 1877; Witkind, 1964; Jackson and Pollard, 1988; Ross, 1992). The igneous rock volume of the magmatism that occurred within the Plateau is mainly accounted for by these three laccolithic intrusive complexes.

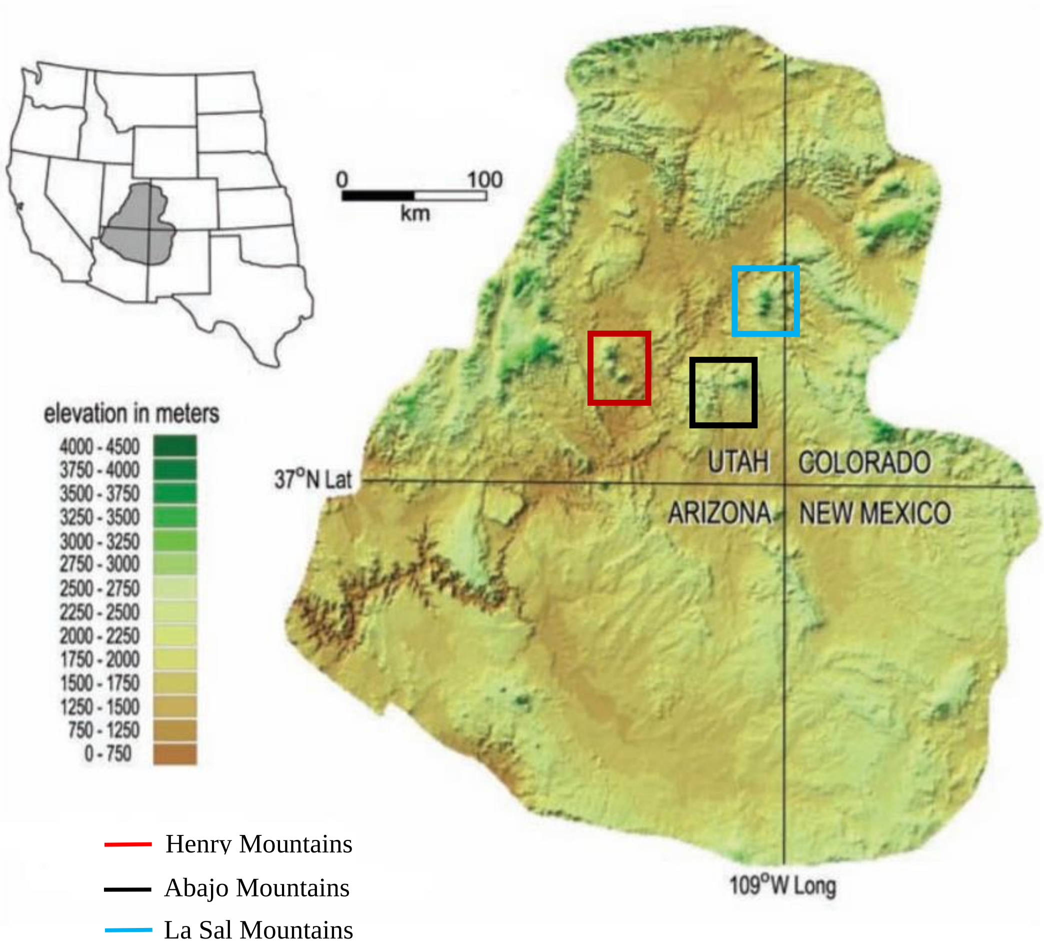

Figure 18. Location (on inset) and elevation map of the Colorado Plateau. Henry Mountains are marked by the red rectangle (modified from Pederson et al., 2002).

5.2 The Henry Mountains

The Henry Mountains of southern Utah are composed of five separate igneous intrusive centers that intruded the Colorado Plateau (Fig. 19) during the Oligocene (Murray et al., 2016). Murray et al. (2016), using zircon U/Pb dating and apatite thermochronology, determined the oldest porphyry to be found within Mount Ellen to be 27.8 ± 0.58 Ma and the youngest at Mount Pennell and Mount Hillers to be 25.5 ± 0.37 Ma. The five intrusive centers were emplaced at approximately 2 - 4 km depth and uplifted the overlying sedimentary strata a maximum of ~ 2000 m. The exposed sedimentary strata are Paleogene in age (Fig. 20) and are predominantly subhorizontal (dipping ~ 2° to the west) away from igneous intrusions like the Henry Mountains and localized structures like the Waterpocket Fold monocline (Gilbert, 1877; Hunt et al., 1953; Jackson and Pollard, 1988).

Collectively, the five intrusive centers in the Henry Mountains preserve a total igneous rock volume of ~ 200 km^3 (Horsman et al, 2018). Each intrusive center can be interpreted as a stage in the progressive growth of a generalized igneous system in the shallow crust due to emplacement of additional magma. Mount Ellsworth and Mount Holmes have the least igneous rock volume (~18 km^3 to ~23 km^3) and are interpreted as an early stage in the development of the system. Mount Hillers and Mount Pennell have a greater igneous rock volume (~24 km^3 to ~ 35 km^3) and are interpreted as an intermediate stage. Mount Ellen, with the largest igneous rock volume (~ 100 km^3), is interpreted as a late stage in the development of a laccolithic intrusive center in the shallow crust (Horsman et al., 2018).

Most of the exposed igneous rock in the Henry Mountains is predominantly bulk andesite-to-trachyandesite composition, with 58-63% SiO_2 and 5-7% $Na_2O + K_2O$. Texturally, the igneous rock is classified as a plagioclase-hornblende porphyry (Hunt et al., 1953; Hunt, 1988; Nelson & Davidson, 1993). The matrix is generally fine-grained and makes up 50% or more of the total rock volume and phenocrysts consist of 20-35% of the total rock volume. Plagioclase phenocrysts constitute 15-25% and hornblende phenocrysts 5-15%. Accessory minerals including clinopyroxene, titanite, apatite, oxides, quartz, and calcite make up 1-2% (Horsman et al., 2018).

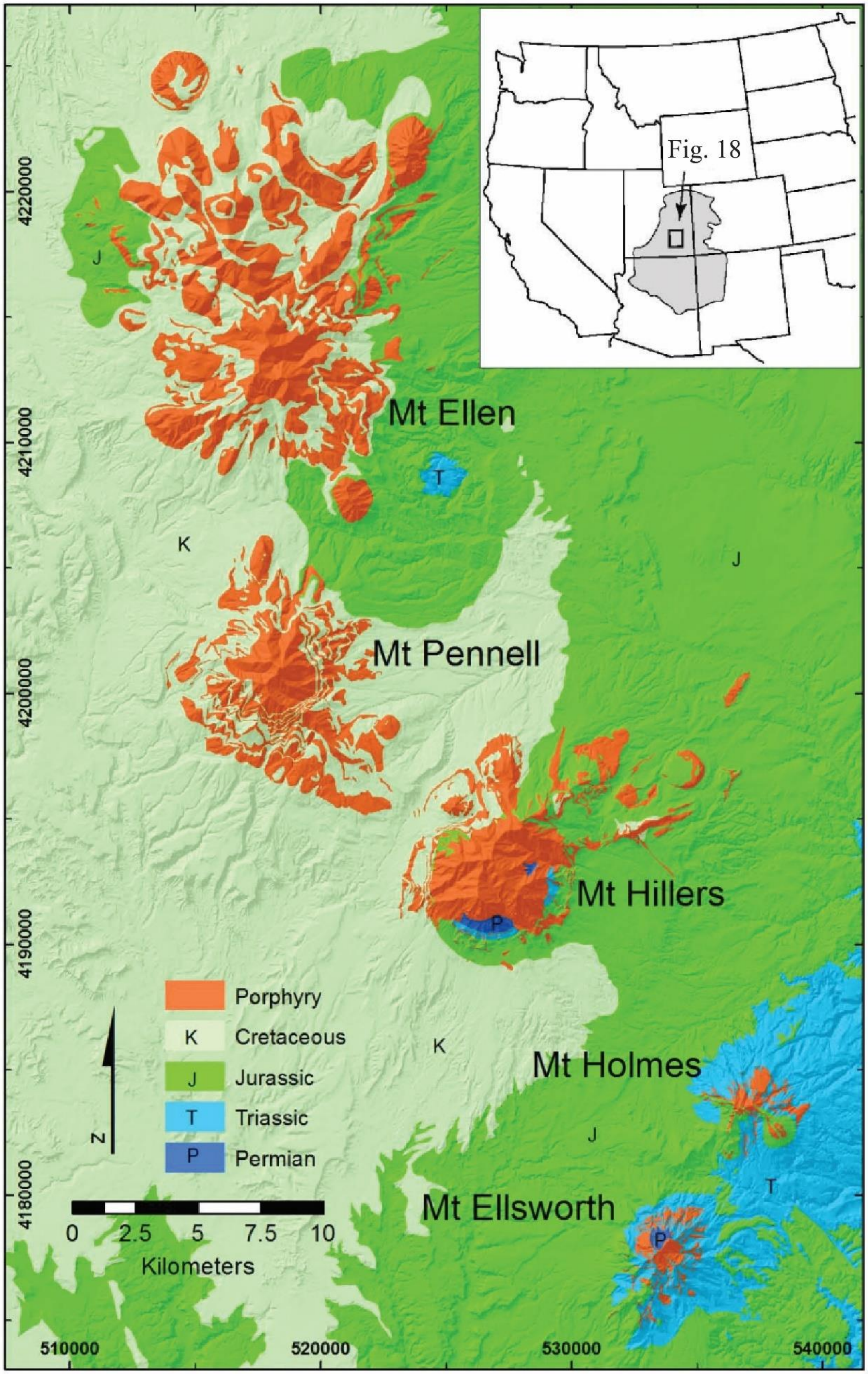

Figure 19. Geologic map of the Henry Mountains of Utah. Igneous rock is marked by orange. The surrounding sedimentary strata is marked by blue and greens. UTM coordinates, zone 12, datum NAD83 (modified from, Horsman et al., 2018).

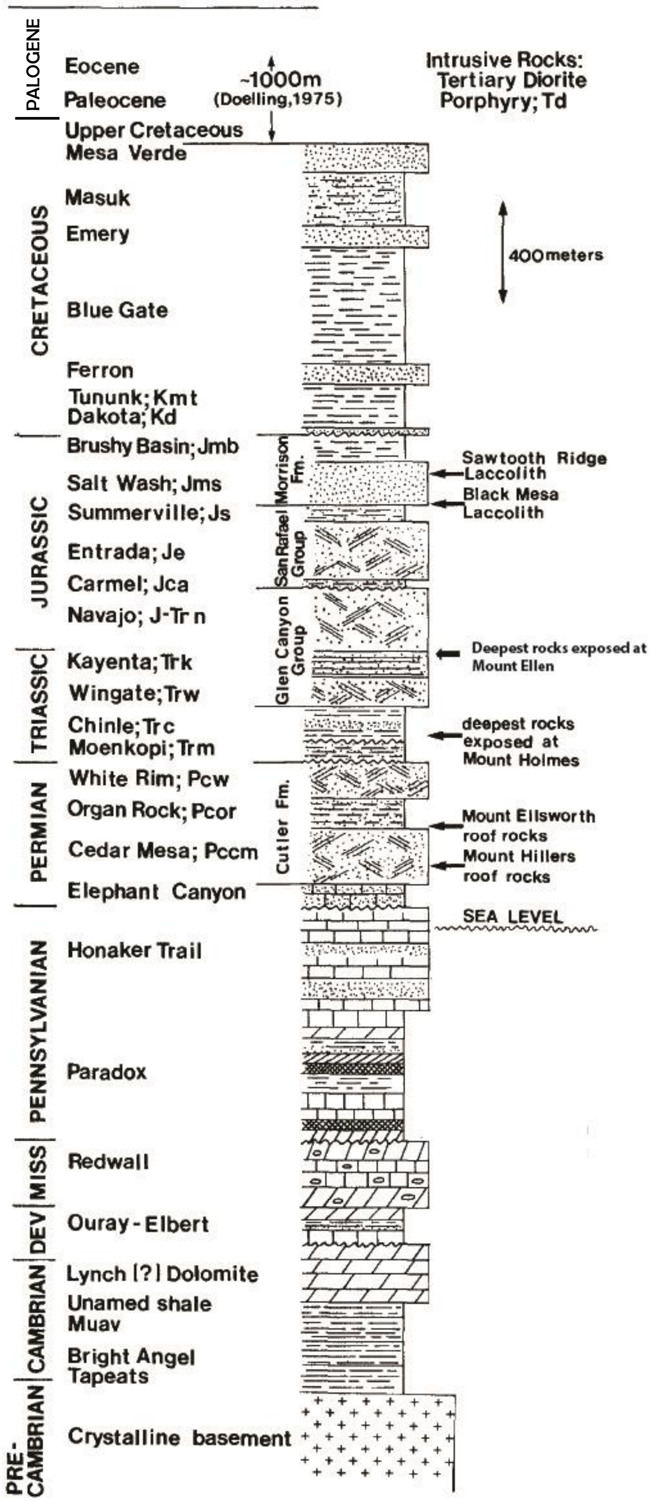

Figure 20. Stratigraphic column of the Colorado Plateau in the region of the Henry Mountains (modified from, Jackson and Pollard 1988).

5.2.1 Previous Work in the Henry Mountains

Gilbert (1877) made initial observations and interpretations of the Henry Mountains geology and recognized the significance of the structural uplift of host rock due to igneous rock emplacement. He coined the term “laccolite” to describe the geometry of what is now referred to as a laccolith. Based on these observations, Gilbert (1877) described an idealized laccolith based on means of formation. According to Gilbert (1877), laccoliths initiate from magma that forcefully emplaces itself concordantly between two strata as a sill. The magma then creates a space for itself by uplifting and deforming the overlying host rock (Fig. 21A). In map view, an idealized laccolith would appear generally circular in shape, in cross-section a convex lens shape. He also noted smaller dikes and sills were generally associated with the formation of laccoliths and postulated the small intrusions fed magma to the larger. Additional observations demonstrated that multiple laccoliths could form above or below one another, causing further displacement of the overlying burden.

Through extensive mapping of the Henry Mountains, Hunt et al. (1953) postulated a different view of laccolith emplacement. The term laccolith was used by Hunt et al. (1953) in a different way than Gilbert (1877). Hunt et al. (1953) proposed that the intrusive centers of the Henry Mountains formed from a discordant stock (Fig. 21B) that fed magma laterally, forming tongue-shaped lobes. Hunt et al. (1953) referred to these tongue-shaped lobes as sills, and inflated tongues as laccoliths.

The major difference to note about the interpretation of a laccolith noted by Gilbert (1877) and Hunt et al. (1953) is how magma is fed to the laccolith. In Figure 21A, Gilbert (1877) suggested a vertical dike that fed magma into a laccolith from below. Hunt et al. (1953) suggested laccoliths were fed laterally from a discordant stock.

Corry (1988) broadened the definition of a laccolith based on numerous studies of igneous intrusions. He determined that laccoliths generally have a minimum thickness of 30 m and this allows them to be distinguishable from sills that are generally 1 m to 10 m thick. He also noted that laccoliths can range in diameter from 1 km to 100 km or greater and have a thickness from 30 m to 15 km. As previously discussed in the Formation of Laccoliths by Successive Sill Accumulation section, the stacking of sills can result in the formation of a laccolith. Corry (1988) concluded that the diameter of a laccolith is dependent on (1) the number of sills contributing to the formation of the intrusion (2) the compression of the overlying strata (3) the depth of intrusion emplacement, and (4) the horizontal stresses. He also noted that there is no simple relationship between the depth of the intrusions and the diameter, therefore, there is no single laccolithic intrusion that suits Gilbert's (1877) idealized model. However, there is some general agreement on certain laccolith characteristics such as: (1) laccoliths form from intrusions of magma; (2) laccolith contacts generally follow the bedding planes of host strata; (3) in cross-sectional view a laccolith may appear to be symmetric or asymmetric, and in map view circular or elliptical.

Jackson and Pollard (1988, 1990) tested both the Gilbert (1877) and Hunt et al. (1953) interpretations of the Henry Mountain intrusion geometries through detailed geologic mapping and structural analysis. Based on their observations, Jackson and Pollard (1988, 1990) found the Gilbert (1877) model to be more representative of how these intrusions were emplaced. The stock interpretation of Hunt et al. (1953) would form buckle folds with geometries different from the bending folds observed in sedimentary strata deformed during the Henry Mountains magma emplacement.

A

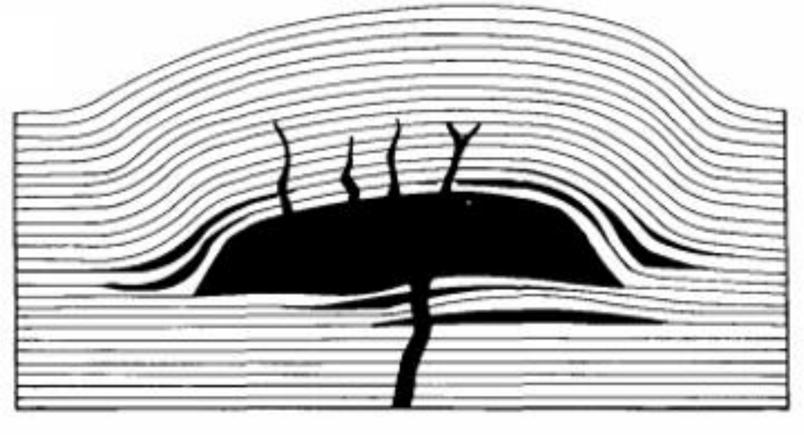

Figure 21 A. Gilbert's (1877) representation of an idealized laccolith in cross-section with a concordant base and convex roof.

B

Figure 21 B. Hunt's (1953) representation of a stock formed laccolith that is discordant with a tongue like lobe expelled from a central stock.

5.2.2 Progressive Intrusion Growth in the Henry Mountains

Recent work compiled by Horsman et al. (2010) provided insight on incremental growth of smaller satellite zone component intrusions on the eastern flank of Mt. Hillers. The three intrusions in this study include the Maiden Creek sill (< 0.03 km^3), the Trachyte Mesa Laccolith (~ 0.05 km^3), and the Black Mesa bysmalith (~0.4 km^3) (Fig. 22). These three small igneous intrusions are interpreted as progressive snapshots of upper crustal plutons evolving from a sill to laccolith to bysmalith. What is notable about these three component intrusions is the total volume of magma that was emplaced. Saint Blanquat et al. (2011) recognized that there was a correlation between the size of an intrusion and its construction time. Intrusions with larger volumes of magma are constructed over longer periods of time. Horsman et al. (2010) proposed an evolutionary model for the construction of these smaller intrusions via pulsed assembly (Fig. 22). Essentially, magma will intrude as a sill that spreads laterally. Additional pulses of magma can promote the sill to evolve into a laccolith with associated uplift and deformation of host rock. Subsequent pulses or an increased magma supply can lead to the formation of a bysmalith, also known as a punched laccolith (Corry, 1988), with associated faulting of host rock to accommodate vertical inflation of the igneous body.

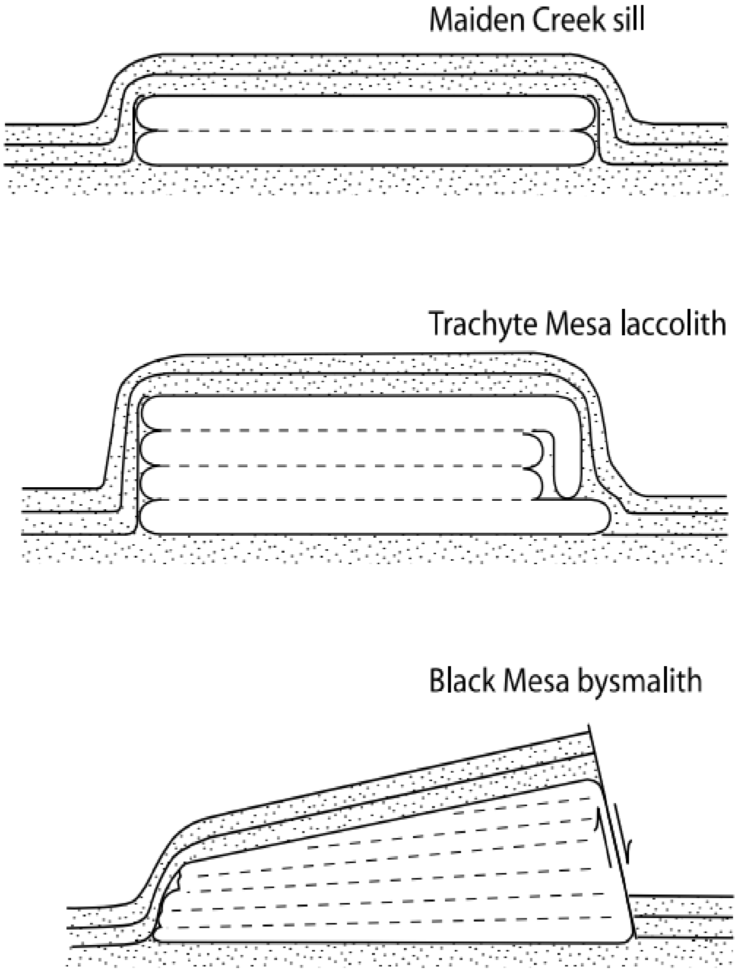

Figure 22. Schematic cross-section of the Maiden Creek Sill, Trachyte Mesa Laccolith, and the Black Mesa Bysmalith. Diagram demonstrates idealized construction of successive pulses for each pluton size. These intrusions are not to scale.

Where detailed work has been done for other intrusions in the Henry Mountains, clear evidence does exist for incremental igneous assembly across multiple spatial scales (Horsman et al., 2005; de Saint Blanquat et al., 2006; Morgan et al., 2008; Horsman et al., 2010; Broda, 2014; Ward, 2014; Maurer, 2015; Thornton, 2015; Horsman et al., 2018). For example, the Copper Ridge Laccolith is constructed from smaller component pulses (each approximately 1 km^3). These smaller component pulses are each constructed from component sheets (each < 0.5 km^3, depending on the volume of larger component pulses). At the scale of an intrusive center, such as Mount Pennell, multiple pulses (each several km^3) were emplaced during assembly.

The Copper Ridge laccolith, on the southeastern margin of the Mount Ellen intrusive center, is an additional example of a component intrusion within the Henry Mountains that demonstrates pulsed assembly. This intrusion is an order of magnitude larger than the previously mentioned intrusions (i.e. Maiden Creek sill, Trachyte Mesa, and Black Mesa), with an igneous rock volume of approximately 2.9 km^3 (Maurer, 2015). The intrusion is constructed from two geochemically distinct igneous sheets (Fig. 23) (Upper and Lower sheet) atop one another (Fig. 24). Each of these sheets may have been constructed from component pulses (Braunagel, et al., 2015).

Generally, a component intrusion within an igneous center in the Henry Mountains tends to have a consistent texture (Horsman et al., 2005; de Saint Blanquat et al., 2006; Morgan et al., 2008) but texture varies both between separate component intrusions and within larger igneous bodies. Horsman et al. (2018) suggests that there are three regions that make up the intrusive centers of the Henry Mountains: the satellite zone, the margin zone, and the central laccolithic body. Here will be discussed intrusions from all three zones.

The Mount Pennell Intrusive complex is approximately 35 km^3 in igneous rock volume. Detailed work on the Mt. Pennell intrusive center (Ward, 2014) demonstrates very clear textural and compositional differences. Nine igneous rock units were identified with distinct textures and compositions, and their spatial distribution had been mapped (Fig. 25). Ward (2015) grouped these nine igneous rock units into three communities (diorite, syenite, and monzonite) based on cross-cutting relationships with other units, assuming they are a part of the same magma pulse.

This previous work in the Henry Mountains demonstrates: (1) intrusions in the Henry Mountains are constructed from component pulses/sheets at multiple spatial scales; (2) as the total magma volume increases, it becomes harder to recognize evidence of incremental constructions, except for rare cases where compositional variations exist and; (3) most intrusions in the Henry Mountains show little compositional variation so it is difficult to demonstrate incremental construction.

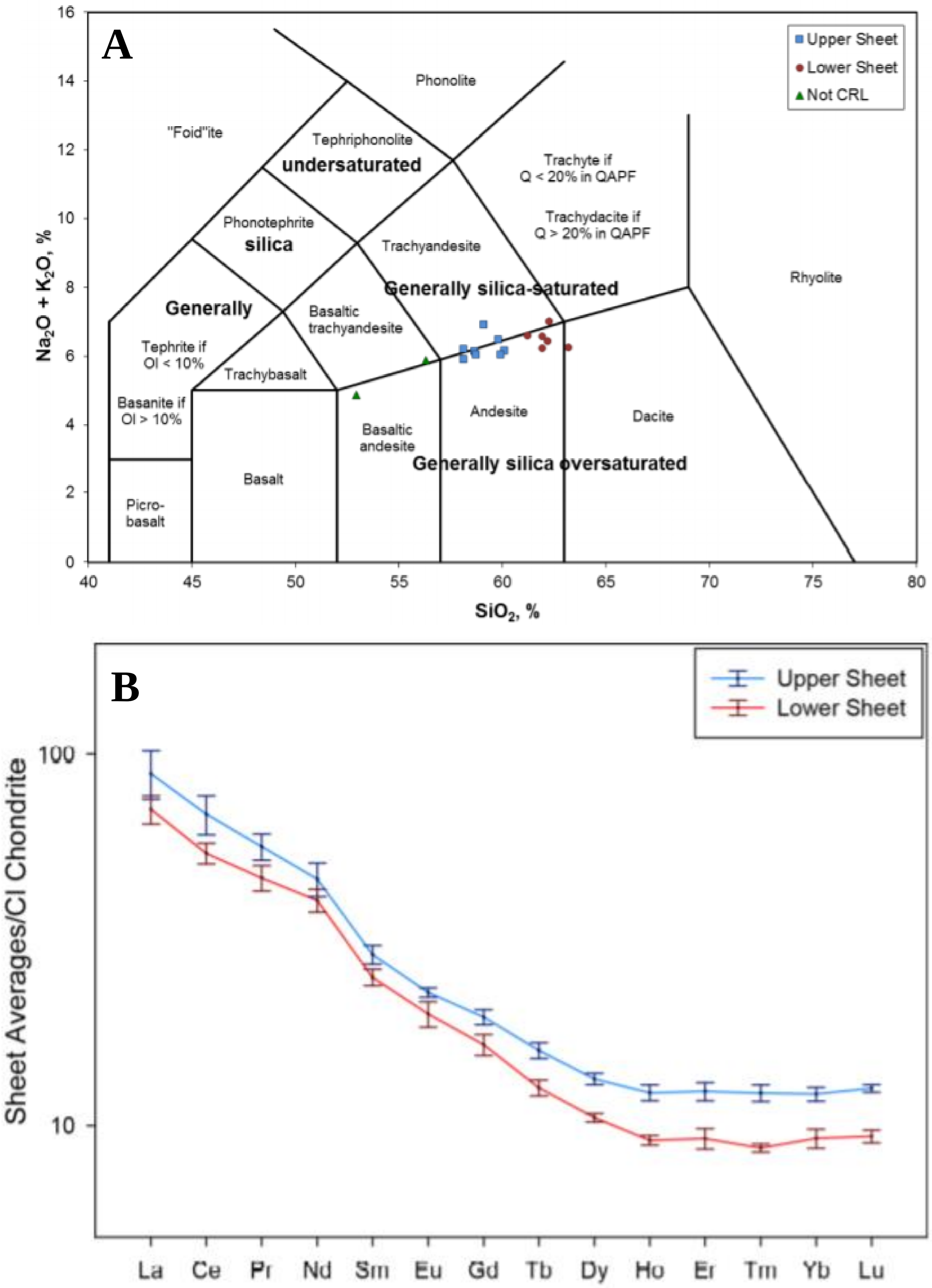

Figure 23. A. Whole-rock major element geochemistry data for the copper ridge laccolith**. B.** Trace element geochemical data for the copper ridge laccolith. Distinct compositional differences can be seen between the two sheets that make up this component intrusion.

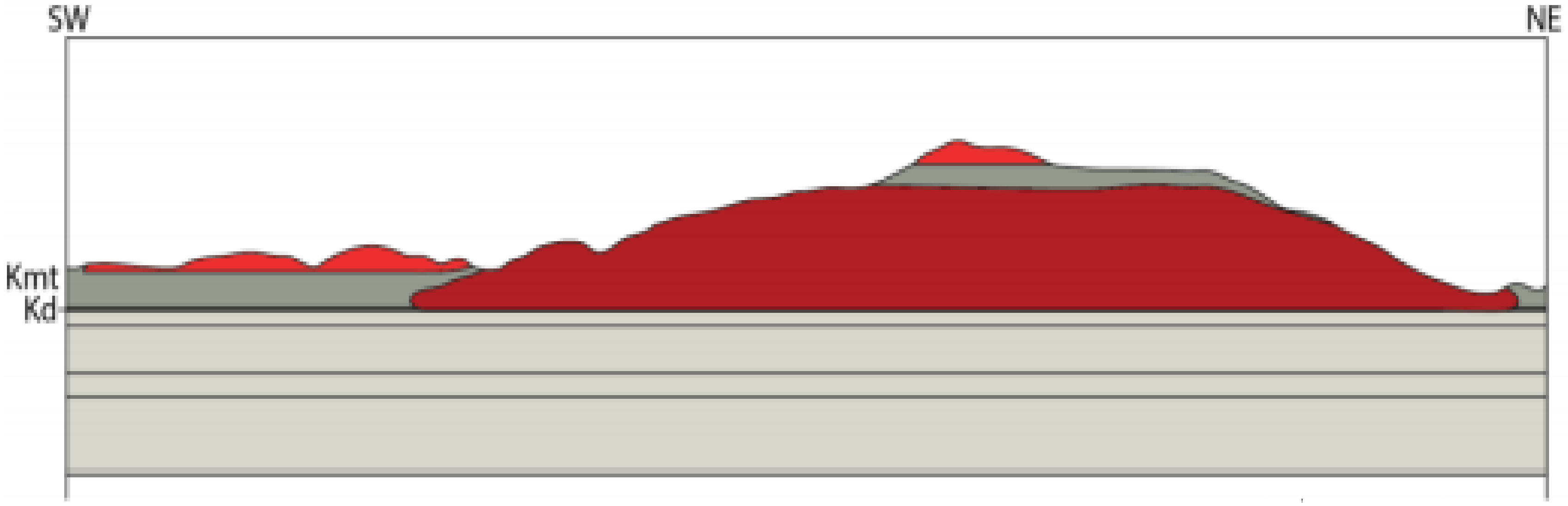

Figure 24. Schematic cross-sectional view of the Copper Ridge Laccolith demonstrating the distinct separation of the upper and lower sheet (Maurer, 2015).

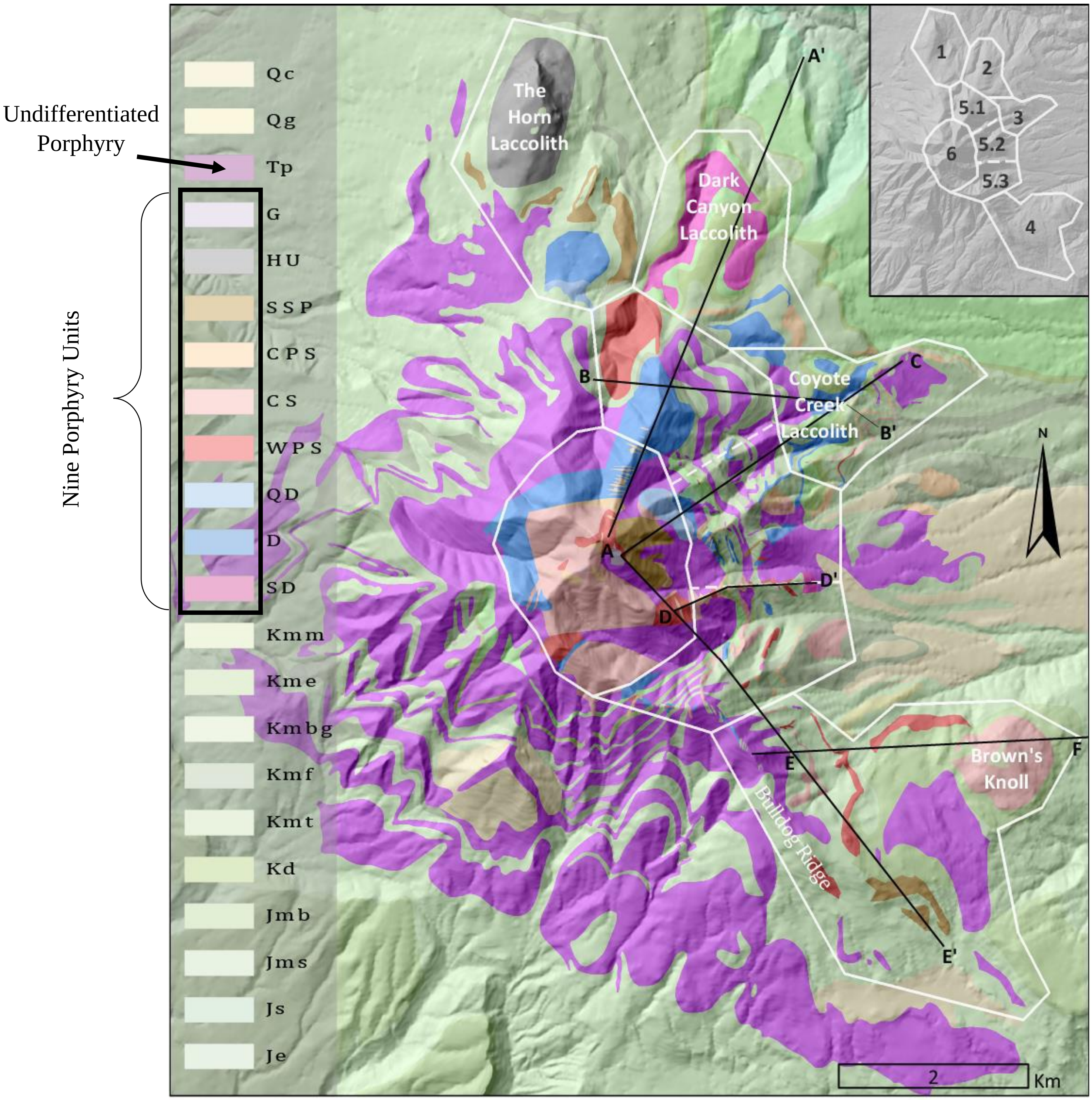

Figure 25. Geologic map of the Mount Pennell Intrusive center demonstrating various igneous units mapped out. The portion of the map outlined in white is the study area (Ward, 2014).

5.3 Mount Ellen

The Mount Ellen intrusive center is the largest of the five intrusive centers in the Henry Mountains both in spatial extent and igneous rock volume. Spatially, Mount Ellen trends NW to SE and extends approximately 15 - 20 km. Mount Ellen is interpreted as a snapshot of a late stage development of a generalized intrusive center (Horsman et al. 2018). Mount Ellen is composed of dozens of component intrusions, including three exposed bsymaliths (Bull Mountain, Table Mountain, and Ragged Mountain) surrounding the main body of the intrusive center (Hunt et al.,1953). Several of these component intrusions are interpreted as radiating lobes from the central portion of the intrusive center (Horsman et al., 2018). A recent study on one of Mount Ellen's component intrusions, the Copper Ridge laccolith, alludes to several of these radiating component intrusions being made up of multiple magma pulses themselves (Maurer, 2015).

Murray et al. (2016), using zircon U/Pb dating and apatite thermochronology, determined the oldest porphyry to be found within Mount Ellen to be 27.8 ± 0.58 Ma. The oldest sedimentary rocks exposed and deformed by the emplacement of the Mount Ellen intrusive center are uppermost Triassic to lowermost Jurassic in age. The stratigraphy has been deflected at a maximum of approximately 2000 m (Hunt et al., 1953; Johnson and Pollard, 1973; Jackson and Pollard, 1988; de Saint-Blanquat et al., 2006; Horsman et al., 2018). The overall igneous rock volume responsible for forming Mount Ellen's dome-like geometry (Fig. 27) is approximately 100 km^3 (Horsman et al., 2018).

Previously, Morton (1984, 1986) mapped the Mount Ellen 7.5' quadrangle and constructed a cross-section (Fig. 26) trending NE to SW. Morton (1984, 1986) followed interpretations by Hunt et al., (1953), by representing the central body of the Mount Ellen intrusive center as a discordant stock with a shatter zone that has satellite intrusions spreading laterally outward. However, interpretations of aeromagnetic data by Jackson and Pollard (1988) illustrate that the central body of the laccolith appears to be mainly concordant with generally sub-horizontal host rock. Horsman et al., (2018) reinterpreted the Mount Ellen intrusive complex geometry in cross-section based on the work of Morton (1984, 1986) and current interpretations on laccolith geometries.

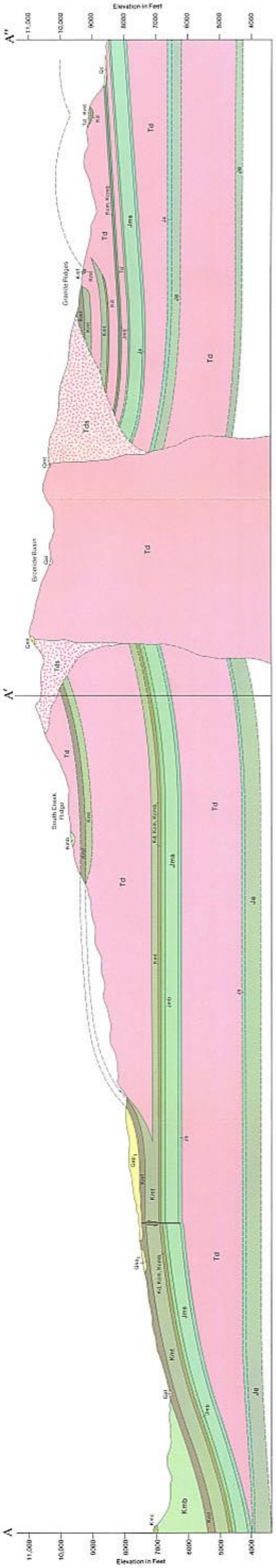

DESCRIPTION OF MAP UNITS

QUATERNARY

Qal	Qmt	Qms	Qc	Qap1	Qap2

Quaternary—Alluvium talus, landslide debris, colluvium, pediment gravels.

TERTIARY

Td	Tds

Tertiary—*Diorite porphyry of Mt. Ellen stock, light grey with abundant oligoclase phenocrysts, weathers to dark brown. Associated minor basalt sills, contact metamorphics, and shatter zone.*

UPPER CRETACEOUS

Mancos Shale

Kmm Masuk Shale Member—*Irregularly bedded, sandy grey shale, sandy carbonaceous shale and sandstone.*

Kmc Muley Canyon Sandstone Member—*(Upper) Interbedded sandstone, siltstone, carbonaceous mudstone, shale, and coal. (Lower) Sandstone, thick-bedded, cliff-forming unit.*

Kmb Blue Gate Shale Member—*(Upper) Interbedded yellowish-grey, very thin bedded to laminated, very fine grained, calcareous, quartzose sandstone and medium grey, gypsiferous shale. (Lower) Dark grey, calcareous shale, upper portion bentonitic.*

Unconformity

Kmf Ferron Sandstone—*(Upper) Lenticular carbonaceous shale; coal; olive-grey marine shale; light-grey, fine-grained, quartzose sandstone. (Middle) Grayish-orange, fine- to medium-grained, quartzose sandstone with minor coaly and carbonaceous horizons. (Lower) Very thin-bedded, greyish-orange, calcareous, kaolinitic siltstone, sandstone, and shale; coarsening upward.*

Kmt Tununk Shale Member—*Medium bluish-grey, thinly laminated to laminated, silty, calcareous, gypsiferous shale; minor thin beds of very fine-grained, quartzose sandstone.*

Kd Dakota Sandstone Formation—*Pale-orange to greyish-yellow, calcareous, very thin to medium grained; with minor interbeds of siltstone; ledge forming.*

Unconformity

LOWER CRETACEOUS

Cedar Mtn. Fm.

Kcm Upper Unnamed Member—*Interbedded, light-grey to brownish-grey, carbonaceous, laminated shale and siltstone with minor laminations of sandstone; coarsens upward.*

Kcmb Buckhorn Conglomerate Member—*Brownish-grey to yellowish-brown sandstone and conglomerate. (Upper) Thin-bedded, fine-grained, cross-laminated sandstone. (Lower) Massive-bedded conglomerate.*

Unconformity

UPPER JURASSIC

Morrison Fm.

Jmb Brushy Basin Member—*(Upper) Pale-greenish-yellow with minor, thin-bedded, fine-grained sandstone; mudstone; claystone. (Lower) Moderate-red mudstone and claystone.*

Jms Salt Wash Member—*Light-grey to brownish-grey, very fine- to granular-grained sandstone with subordinate reddish and greenish bentonitic mudstone. General upward coarsening in sandstone.*

Unconformity

Js Summerville Formation—*Pale-reddish-brown to light-brownish-grey siltstone, mudstone, and shale interbedded with occasional hematitic gypsum.*

Jc Curtis Formation—*Light-greenish-grey, glauconitic, calcareous siltstone, with minor greyish-purple shale.*

Unconformity

Je Entrada Sandstone—*Pale-red to pale-orange, very fine grained, thin-bedded to massive, calcite-cemented, sandstone and minor siltstone; minor gypsum. Weathers to ledges with minor slopes and low, resistant, rounded outcrops.*

Figure 26. Geologic cross-section of the Mount Ellen intrusive complex with stock and shatter zone for central portion of the intrusions (Morton, (1984,1986).

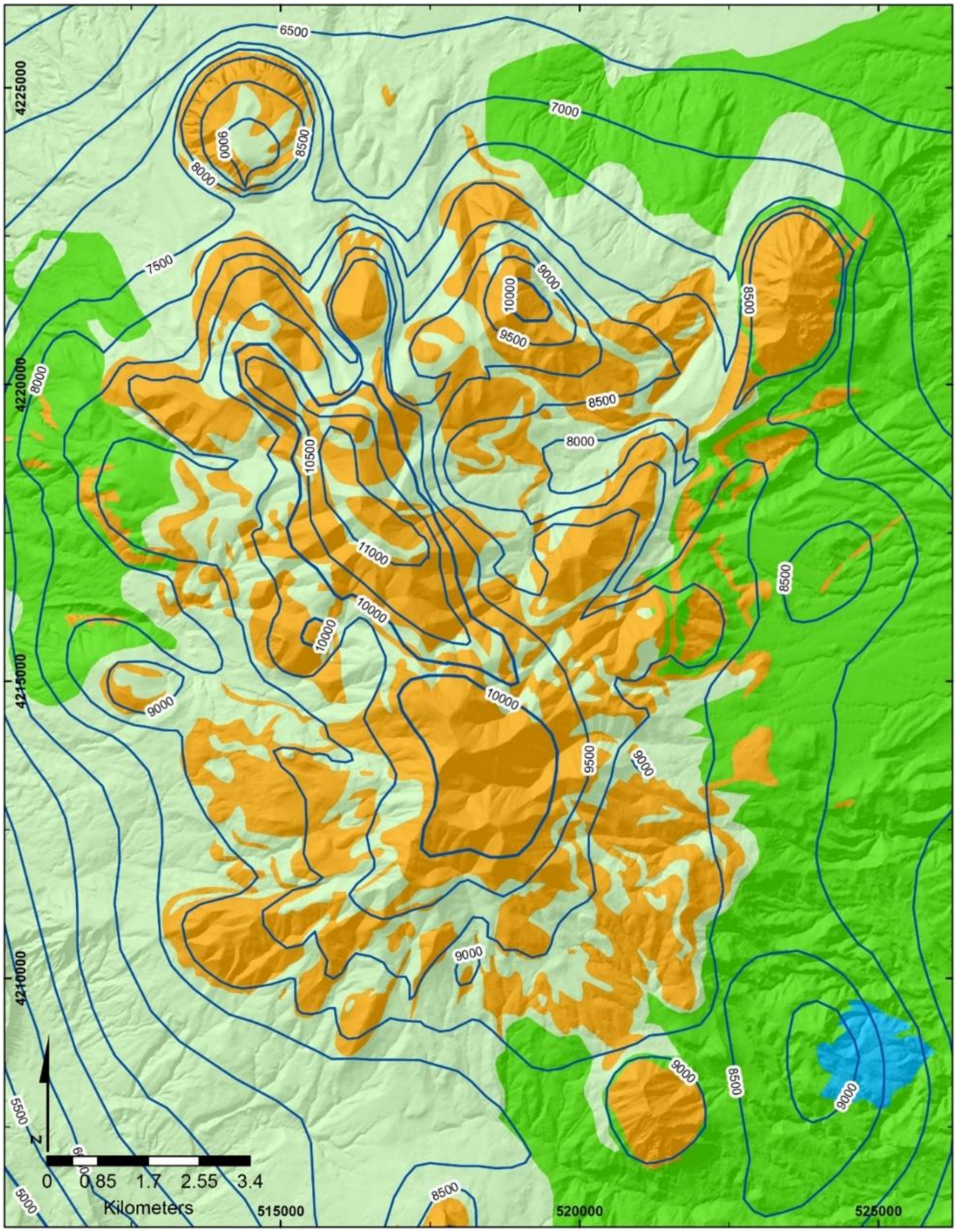

Figure 27. Structure contour map of the Mount Ellen intrusive center (500 ft contour interval), showing overall dome-like appearance. UTM coordinates, zone 12, datum NAD83

6. Methods

To address the research question, I used the following methods: field work, whole-rock major and trace element geochemistry, anisotropy of magnetic susceptibility, and crystal size distribution analysis. Each method provides a different aspect of analyzing the igneous rock of the Mount Ellen intrusive complex. Resulting data allows for interpretations on how Mount Ellen was constructed over time from multiple component magma pulses.

6.1 Data Compilation

In addition to collecting new data, supplementary data sets for geochemistry, anisotropy of magnetic susceptibility, and crystal size distribution (Morton, 1984; Nelson & Davidson, 1993; Maurer, 2015; and unpublished data) for the Mount Ellen intrusive complex were compiled for analysis. This allowed for a greater spatial distribution of data and for appropriate planning of samples collection for this study where samples were lacking spatially.

6.2 Field Work and Sample Collection

Field work was conducted during the summers of 2018 and 2019. Detailed observations of rock characteristics include measurements of lineations and foliations, size and abundance of phenocrysts and xenoliths present, color of rock matrix, observations on the interaction between the igneous rock and host rock, and presence of cross-cutting relationships.

Additionally, thirty oriented igneous rock samples were collected for laboratory analysis (Fig. 28). Sampling locations were chosen based on outcrop availability and to complement previously sampled locations. Location for all samples are provided in Appendix D. Care was taken to ensure the freshest possible sample at each location (Fig. 29).

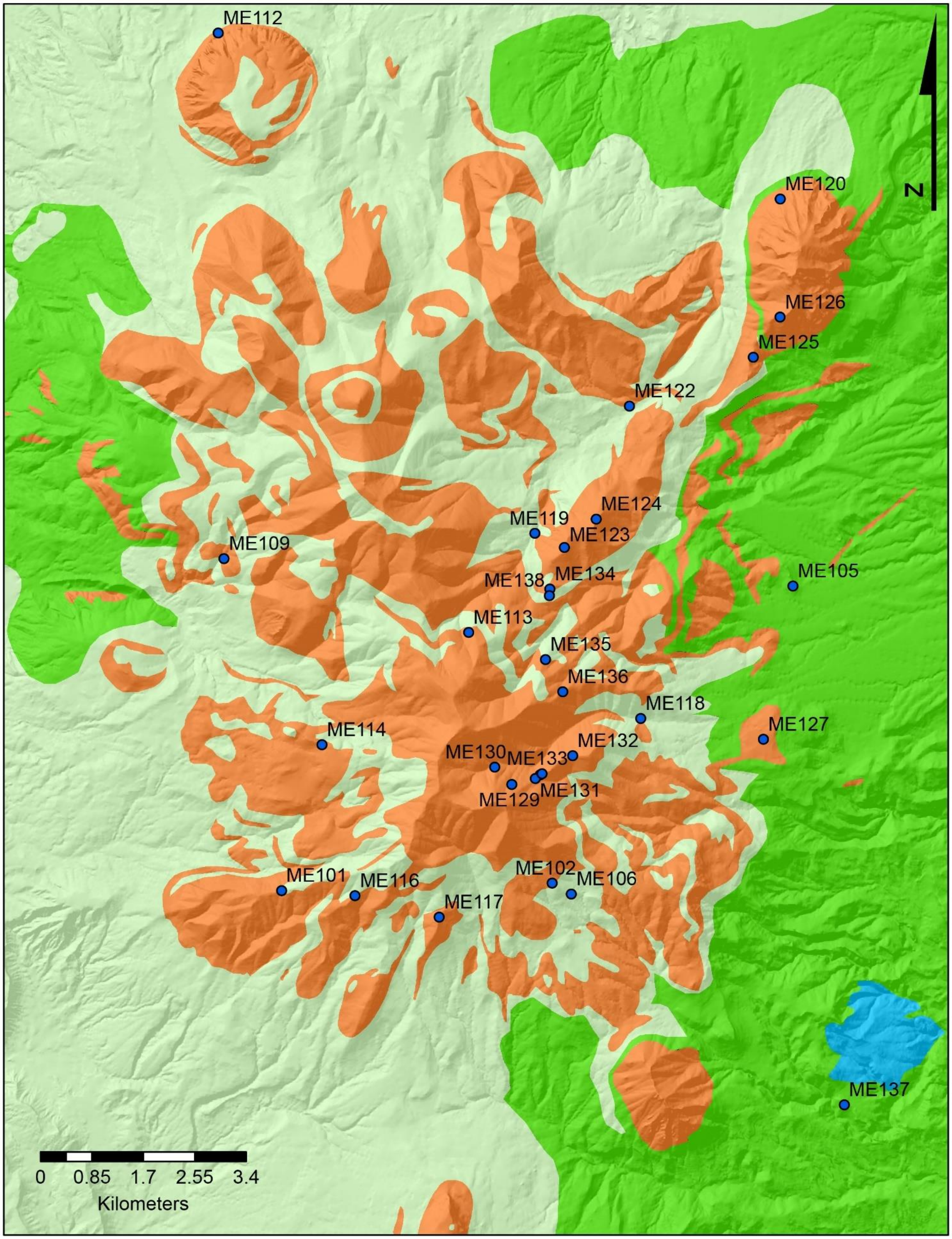

Figure 28. Geologic map of Mount Ellen showing new sample (2018, 2019) locations with blue dots.

Figure 29. Trevor Burns inspecting an oriented sample in the field.

6.3 Geochemistry

Whole-rock major and trace element geochemistry was used to test for any chemical variation that may help distinguish between samples and classified textures. Recent detailed studies on component igneous intrusions in the Henry Mountains suggest significant differences in the composition of the igneous rock (Gwyn, 2011; Broda, 2014; Maurer, 2015; Thornton, 2015). Samples were selected to capture a wide spatial distribution of data and provide multiple samples from each classified texture.

Whole-rock major and trace element geochemistry data were acquired through commercial analysis of 26 samples at Acme Analytical Laboratories (Vancouver, Canada). For each sample, three 22 mm core specimens were chosen for Acme Labs to process by ICP-MS for whole rock major element geochemistry and ICP-MS for whole rock trace element geochemistry (PRP70-250, LF202 procedures). Results of the analysis are presented in Tables 6 - 15 (Appendix A), along with data from all previously analyzed samples.

6.4 Anisotropy of Magnetic Susceptibility

Anisotropy of magnetic susceptibility (AMS) analysis provides information on the preferred orientation and distribution of minerals in a sample (Hrouda, 1982). Data were collected by placing a sample in a known magnetic field and measuring the characteristics of the magnetic field induced in the sample using an AGICO MFK1-A kappabridge. The magnetic field induced in a rock sample depends on the orientation, distribution, and magnetic susceptibility of all mineral grains within the sample. This method is beneficial in obtaining magnetic fabrics when field fabrics are difficult to measure or are weak. Previous studies have used AMS in igneous rocks to interpret magma flow direction (e.g. Horsman et al., 2005; Saint Blanquat et al., 2006; Stevenson et al., 2007; Morgan et al., 2008).

The AMS of a rock sample is represented with an ellipsoid and interpreted as a magnetic fabric. The resulting ellipsoid has three mutually perpendicular principal axes: long, intermediate, and short, noted as K_1, K_2, and K_3. The axis orientations and lengths provide a measure of magnetic fabric (e.g. foliation and lineation). The fabric orientations are not considered further in this thesis. The axis lengths can be used to calculate several scalar parameters that quantify aspects of magnetic fabrics. For this study, I use the AMS scalar parameters of the igneous rock in the Mount Ellen intrusive complex and interpret the bulk susceptibility.

For this research the following five parameters were used to interpret AMS results from Mount Ellen:

$$K_m = (K_1 + K_2 + K_3)/3 \tag{4}$$

$$T = [2\ln (K_2/K_3)/\ln(K_1/K_3)] - 1 \tag{5}$$

$$P_j = \exp (2[(\eta_1 - \eta_b)^2 +(\eta_2 - \eta_b)^2 + (\eta_3 - \eta_b)^2]^{½} \tag{6}$$

$$L = K_1/K_2 \tag{7}$$

$$F = K_2/K_3 \tag{8}$$

The mean susceptibility (K_m), is the measure of the abundance of magnetic minerals. The mean shape factor (T) quantifies the shape of the AMS ellipsoid, where a sphere has a shape factor of T=0, a perfectly prolate ellipsoid has a shape factor of T= -1, and a perfectly oblate ellipsoid has a shape factor of T=1. The mean degree of anisotropy (P_j) quantifies the intensity of the magnetic fabric within a specimen. In equation 6., $\eta_1 = \ln K_1$, $\eta_2 = \ln K_1$, $\eta_3 = \ln K_1$, and $\eta_b = \ln(\eta_1 \cdot \eta_2 \cdot \eta_3)$ respectively. Lineation (L) describes the fabric of mineral grains whose dimensional orientation are best represented the long axis of elongated minerals. The long axis of the AMS ellipsoid represents magnetic lineation. Foliation (F) describes the alignment of minerals parallel to the internal or external pluton contacts. The short axis of the AMS ellipsoid represents the pole to magnetic foliation.

AMS was measured on 30 oriented samples collected in the field at various locations on the Mount Ellen intrusive center. Each sample was drilled in the laboratory to extract 25-mm diameter cores (Fig. 30). The orientation of each core was measured relative to marks made in the field on each sample. Each core was cut into 22-mm long specimens (Fig. 31). At least 6 specimens per sample were measured using an AGICO MFK1-A magnetic susceptibility bridge at East Carolina University. The resulting data for all specimens from each sample were processed through software AniSoft, providing the magnetic parameters previously mentioned (K_m, T, P_j, L and F) for each sample. The summarized results can be found in Table 3.

Figure 30. Drill used for coring all samples to extract 25-mm diameter cores.

Figure 31. Cores drying after they were cut into 22-mm long specimens.

6.5 Crystal Size Distribution

Crystal size distribution (CSD) analysis provides a quantitative measure of rock texture based on size, shape, orientation, position, and proximity of contact between crystals within igneous rocks (Cashman and Marsh, 1988; Marsh 1988;1998; Higgins and Roberge, 2003, Mock et al., 2003). Results provide information about kinetic and physical processes that affect crystallization of magmas (Marsh, 1988). Understanding petrographic characteristics such as grain size and modal abundance can be extremely useful in conjunction with geochemical studies to help constrain the thermal and crystallization history of igneous intrusions (Cashman and Marsh, 1988; Marsh 1988, 1998; Higgins, 2000; Higgins and Roberge, 2003; Mock et al, 2003). In recent studies in the Henry Mountains, on intrusions at different spatial scales, CSD analysis has proven useful in quantifying texture differences that potentially formed from distinct magma pulses (Gwyn, 2011; Broda, 2014; Thornton, 2015, Maurer, 2015).

For this study, 31 samples were measured for plagioclase CSD and 25 samples were measured for hornblende CSD. A slab was cut from each hand sample to expose a fresh surface. A qualitative analysis of the fresh surfaces resulted in an initial classification of five textures (Textures 1 – 5). Each slab was then scanned at a high resolution (3400 dpi) to obtain a clear image for CSD analysis (Fig. 32A).

Using Adobe Photoshop, the rock slab images were processed to isolate phenocrysts of plagioclase and hornblende as separate images based on color (plagioclase, generally lighter than matrix and hornblende, generally darker than matrix). Once isolated, the images of the crystals were converted to binary images, to present the crystals as a single color (black, Fig. 32B). These images were then imported into the software ImageJ before processing for CSD analysis. This software was used to remove parts of the image with an area less than 5 pixels (despeckling).

This ensured that the image was capturing solely the phenocrysts within the rock slab and not the groundmass. Then to fill in areas where crystals were incomplete, because of the limitations of selecting crystals by color in Photoshop, the “fill-holes” feature was used in the ImageJ software. This gave the crystals a more distinct shape and outline for analyzing. Obvious xenoliths present within samples were removed from the images, in addition to incomplete crystals near edges of the rock slab (Fig. 32C). ImageJ then measured the dimensions and area of each phenocryst. The resulting data from ImageJ were imported into the program CSD Corrections version 1.6 (Higgins, 2000) for each sample.

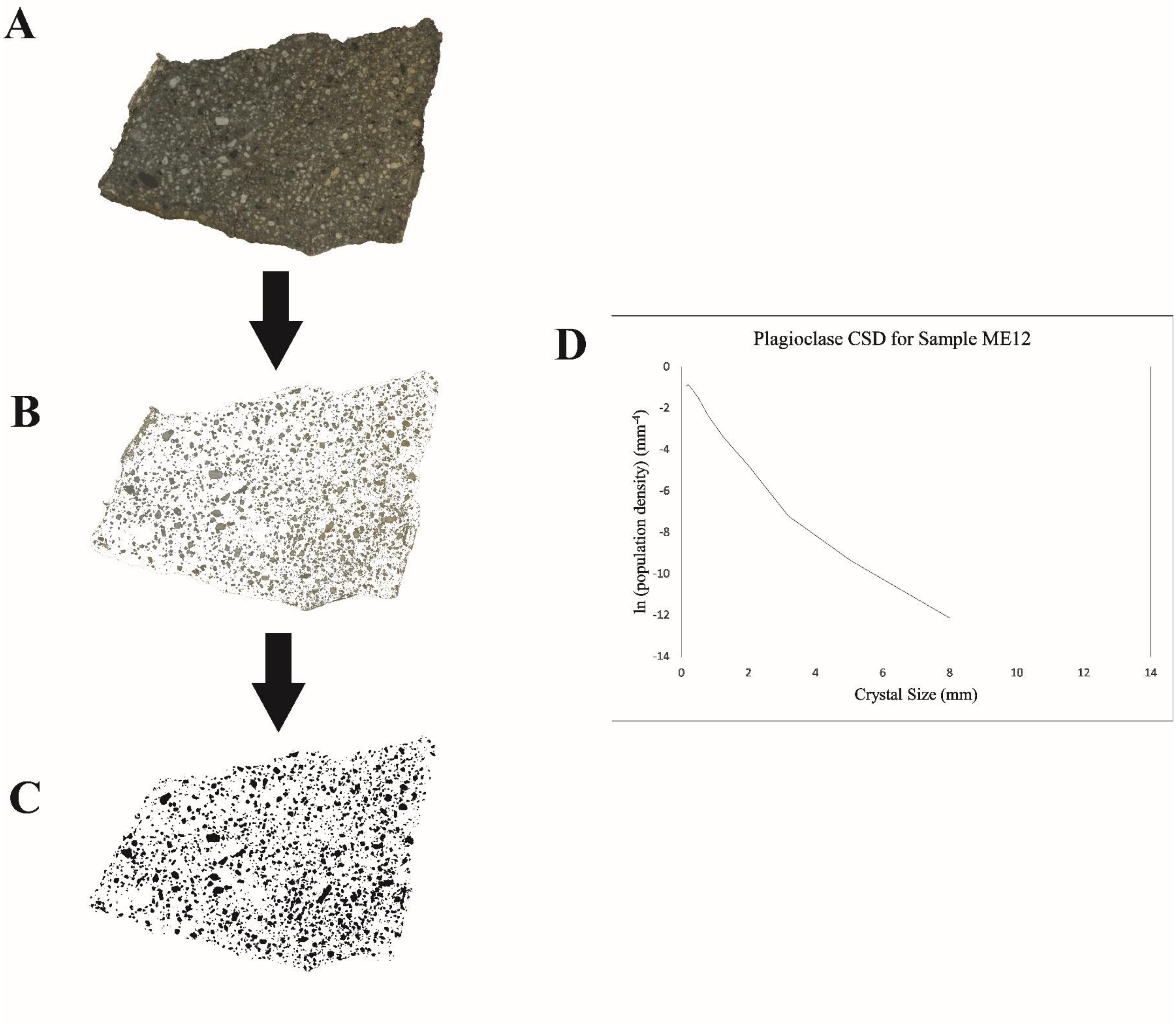

Figure 32. A. Rock slab image of sample ME12 analyzed for CSD of plagioclase phenocrysts. **B.** Resulting photoshop image after isolating crystals based on color. **C.** Resulting ImageJ photo after removal of image parts of 5 pixels or less and after filling in missing area of crystals and removal of incomplete crystals around edges **D.** Produced CSD curve for sample ME105.

Output from the CSD Corrections software included graphical and numerical results for each set of phenocrysts from each sample. CSD Corrections converts the 2D measurements of the crystal dimensions from a best-fitting ellipse to a 3D CSD. The resulting data indicate the number of crystals per unit volume within a series of defined crystal size bins. This produces a histogram with these different size bins (Higgins, 2000) and the CSD curve is defined from points connected at the midsection of each bin (Fig. 33). The resulting number of bins is dependent on each sample and crystal sizes for each sample. The abundance of crystals per each crystal size bin results in the population density for each interval. The natural logs of the population densities are plotted against the histogram midsection values for each size bin.

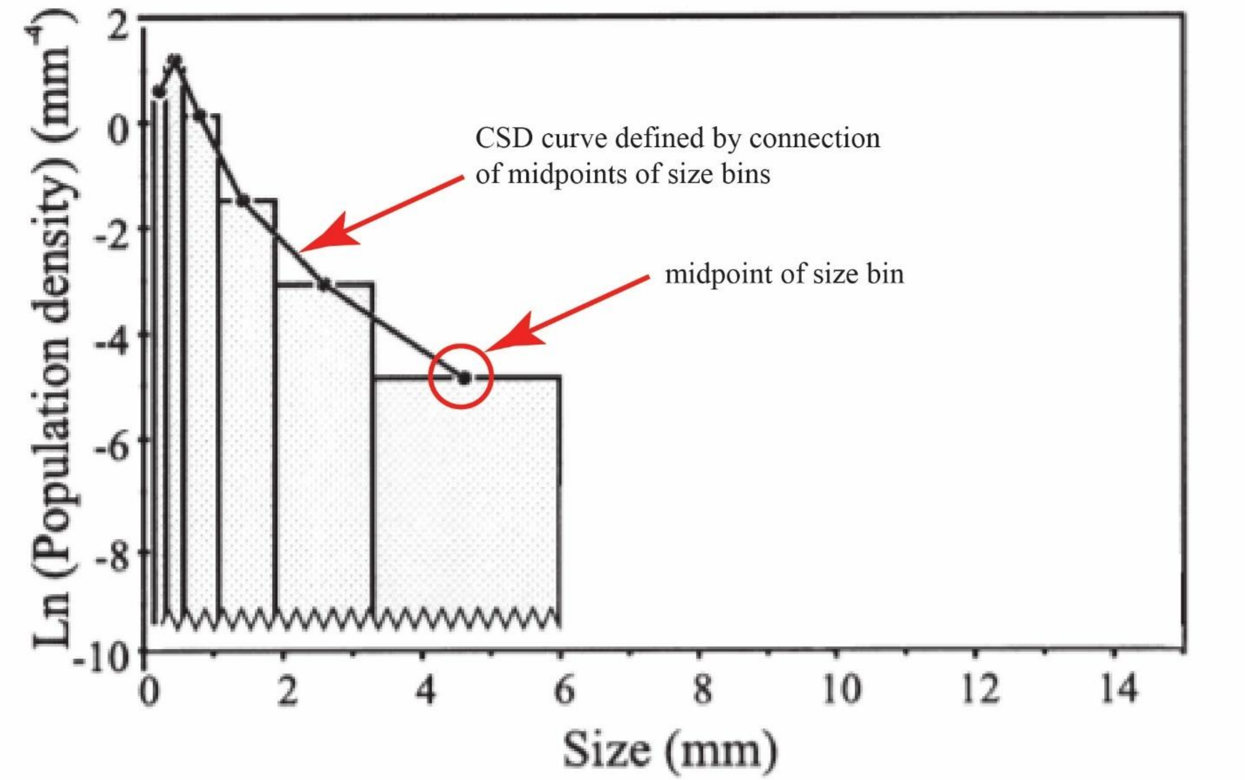

Figure 33. Diagrammatic representation of how a CSD curve is produced from mid-point of histogram bins (modified from Higgins, 2000).

Marsh (1988) modified the application of CSD theory from Randolph and Larson (1971) for geological application in magmatic systems. Marsh (1988) demonstrated that there is a linear relationship between the natural logarithm of the population density versus crystal size using the following equation:

$$(9) \qquad n'_V(L) = n'_V(0)e^{-L/G\tau},$$

where $n'_V(L)$ (mm^{-4}) is the population density of crystals for size L (mm), $n'_V(0)$ represents the nucleation density, G is the growth rate (cm/sec) and τ is the residence time (years). Characteristic length is defined by:

$$(10) \qquad C = G\tau.$$

The nucleation density is represented by the y-intercept as ln ($n'_V(0)$) and the slope is calculated by the negative reciprocal of the characteristic length ($-1/C$). The characteristic crystal length is the product of residence time (τ) and growth rate (G) for a straight lined CSD. Slopes were calculated for the averages of each textural group and the values were used to calculate the residence time (the amount of time crystals spent crystallizing) for these crystals in magma using the following equation:

$$(11) \qquad \tau = \left(-\frac{1}{G\mathrm{x}m}\right) / \ 31536000.$$

For this formula, the value of G is based on experimental values for growth rates of hornblende and plagioclase crystals. G value maximums and minimums from $3 \cdot 10^{-7}$ cm/s and $1 \cdot 10^{-8}$ cm/s are modeled for hornblende crystals after Bonechi et al. (2020). For plagioclase crystals, maximum and minimum values for G range of $1.7 \cdot 10^{-6}$ cm/s and $7 \cdot 10^{-10}$ cm/s were used after Cashman (1993). The value 31536000 converts seconds to years. Using these parameters from a produced CSD curve can then be used to interpret the crystallization history of the magma(s).

The shape of a CSD curve is related to the crystallization history and final crystal size. For example, if the growth rate (G) and residence time (τ) for crystals within a sample are constant, the resulting CSD slope would be a straight line (Fig. 34). This would indicate a steady-state system with continuous crystallization during monotonic cooling (Marsh, 1988, 1998; Higgins 2003). However, many rocks have a CSD curve with a concave up shape (Higgins 2003, 2006), which is the case for the samples of the Mount Ellen intrusive complex. Samples produced a nonlinear, concave up CSD with segments that have different slopes. Many crystallization histories could produce such curves. Textural coarsening and magma mixing (Fig. 36) are two mechanisms that are believed to influence the resulting shape of a concave up curve (Higgins, 2003; Higgins, 2006; Higgins; 1998).

Resulting CSD data were used to quantify the textural differences between the five different textural groups for Mount Ellen. In addition to examining the resulting CSD curves, the slopes ($-1/C$) and the y-intercepts ($\ln (n'_V(0))$) provide quantitative measures of rock texture. The slope can provide information about growth rate and residence time for each sample. The y-intercept provides a means of analyzing the final nucleation density for each sample (Mock et al, 2003). To quantify the slope changes of these CSDs, the changes in slope are broken into two separate components, late-stage (microphenocrysts) and early-stage (phenocrysts) crystallization (Fig. 36). The cut off crystal size to distinguish between the late-stage and early-stage boundary is approximately between 1 mm to 2 mm in size based on where the slope changes for the CSD for both plagioclase and hornblende.

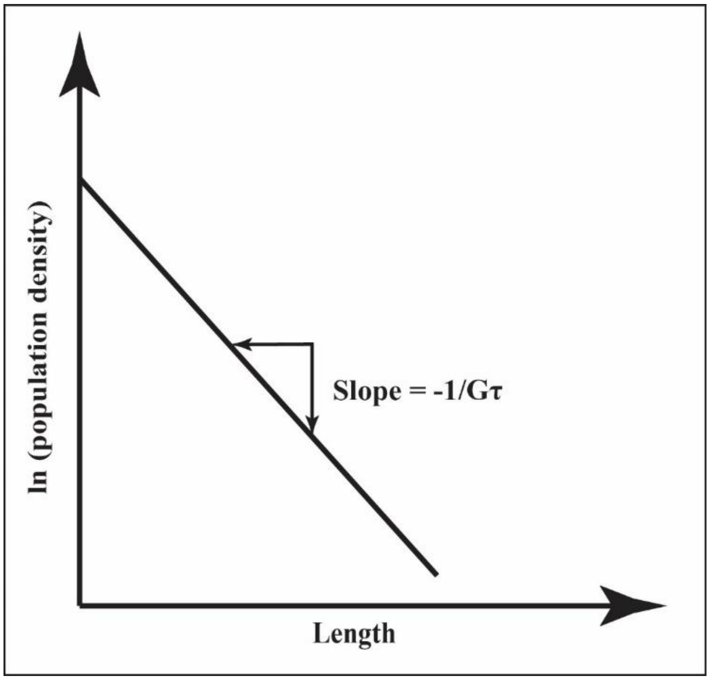

Figure 34. Schematic diagram of CSD curve produced from a single magma batch with monotonic cooling (Marsh, 1988).

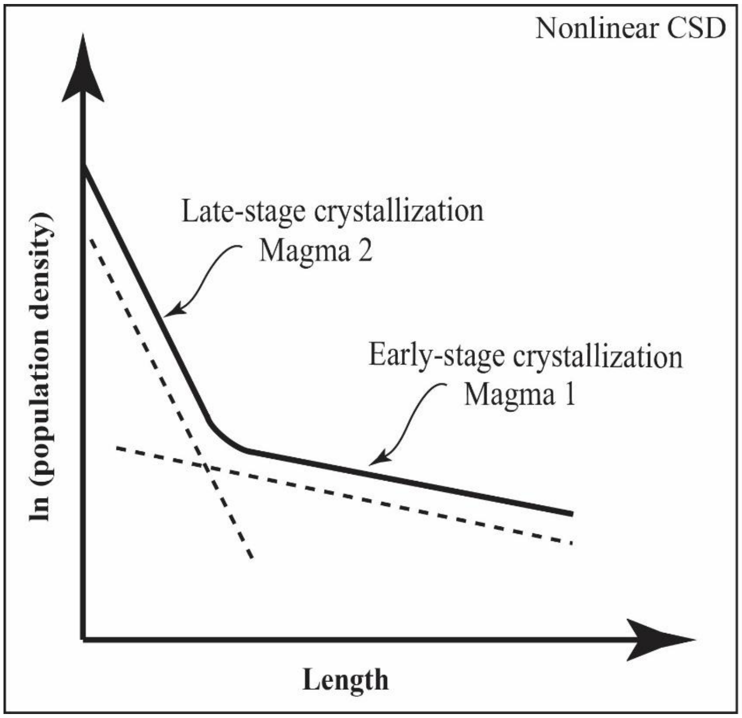

Figure 35. Schematic diagram of magma mixing or mixing of two crystal populations to produce a kinked CSD curve (Higgins, 2006).

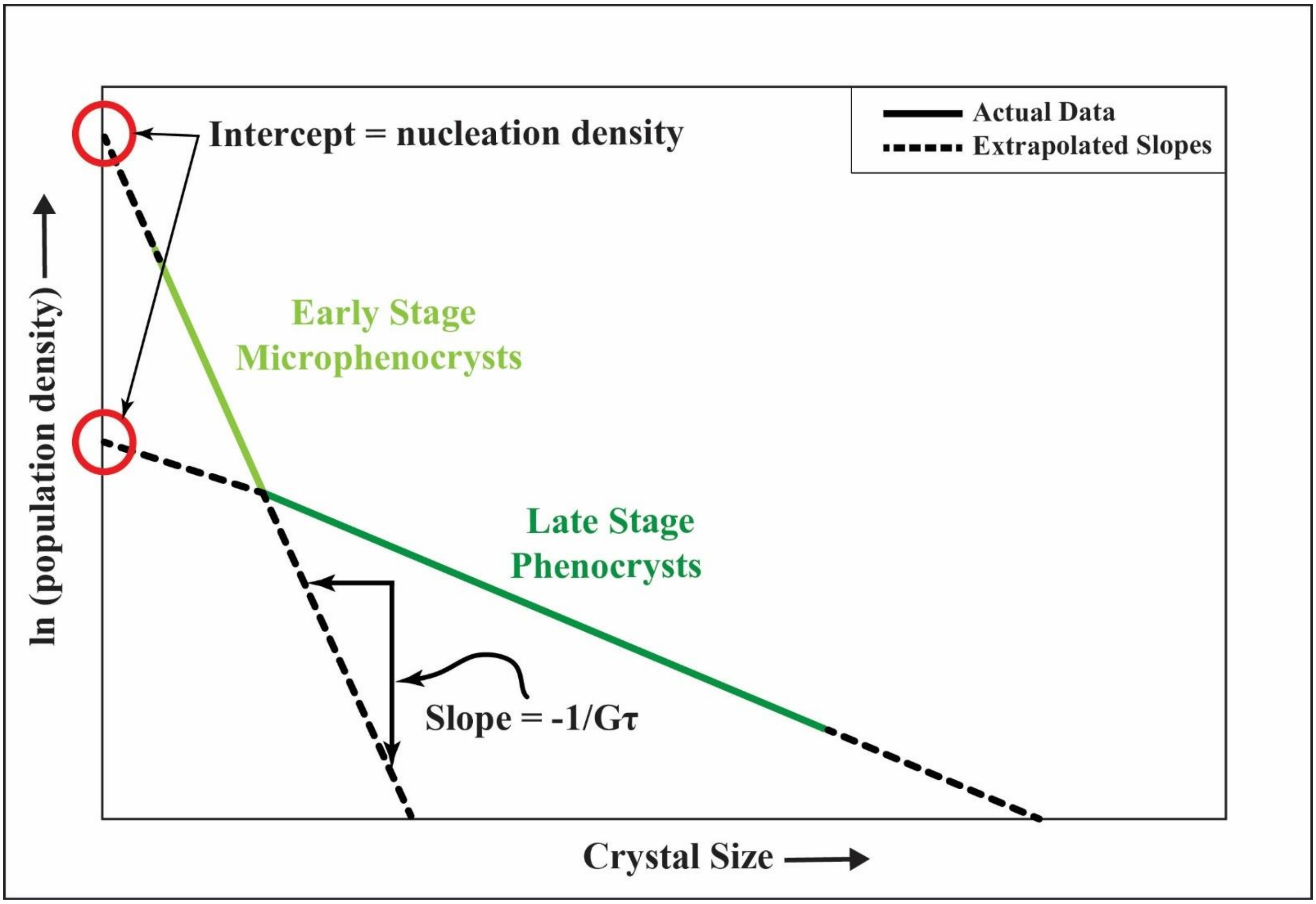

Figure 36. Diagrammatic example of CSD graph demonstrating variables.

7. Results

7.1 Field Work

Field work was used to construct a new geologic cross section of Mount Ellen (Fig. 37, 38), make note of rock compositions, texture, and observe contacts between intrusions and surrounding sedimentary host rock. Based on field observations and previous research (Hunt et al, 1953; Morton, 1986; Maurer, 2015; Horsman et al., 2018), the new cross section was constructed (Fig. 37, 38) where sampling was most prevalent and where contacts between sedimentary host rock and igneous rock were best exposed. Exposed contacts between sedimentary host rock and igneous rock can be observed in field photos (Fig. 39). Two of the contact exposures were observed near the central body of the intrusions (Fig. 39B, C). Exposure of a newly discovered dike is shown in Figure 39D. The location of this dike is found within the Maze Arch, far from the central intrusion of Mount Ellen. The Maze Arch is a dome-like feature of sedimentary host rock that is on the southeastern margin of Mount Ellen that can be observed in cross section A to A'. The Maze Arch is approximately 3 km in diameter and consists of a buried laccolith overlain by sedimentary strata uplifted approximately 150 m (Hunt et al, 1953).

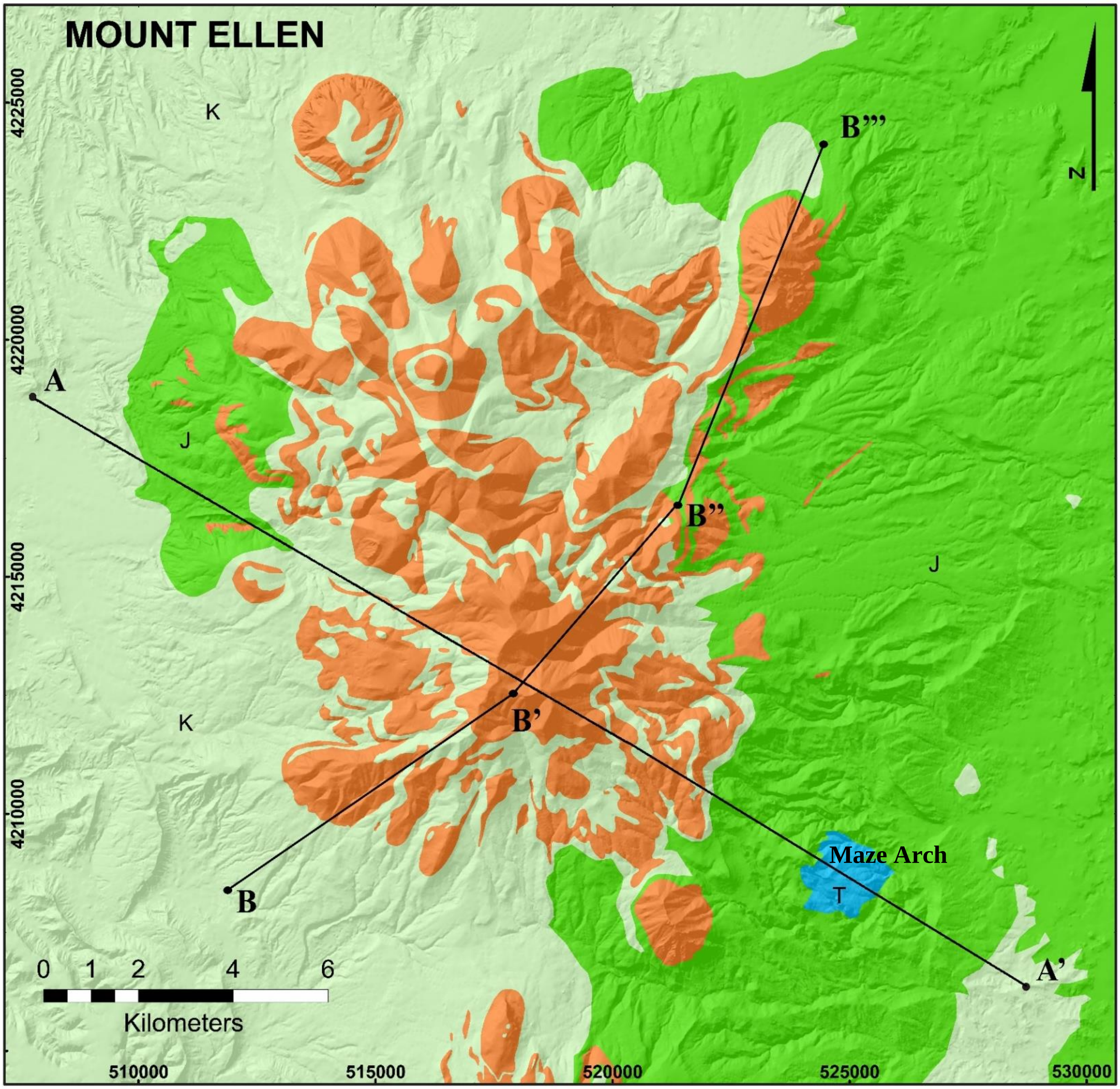

Figure 37. Geological Map with cross sections A-A' and B-B''' noted (modified from Horsman et al., 2018) UTM coordinates, zone 12, datum NAD83.

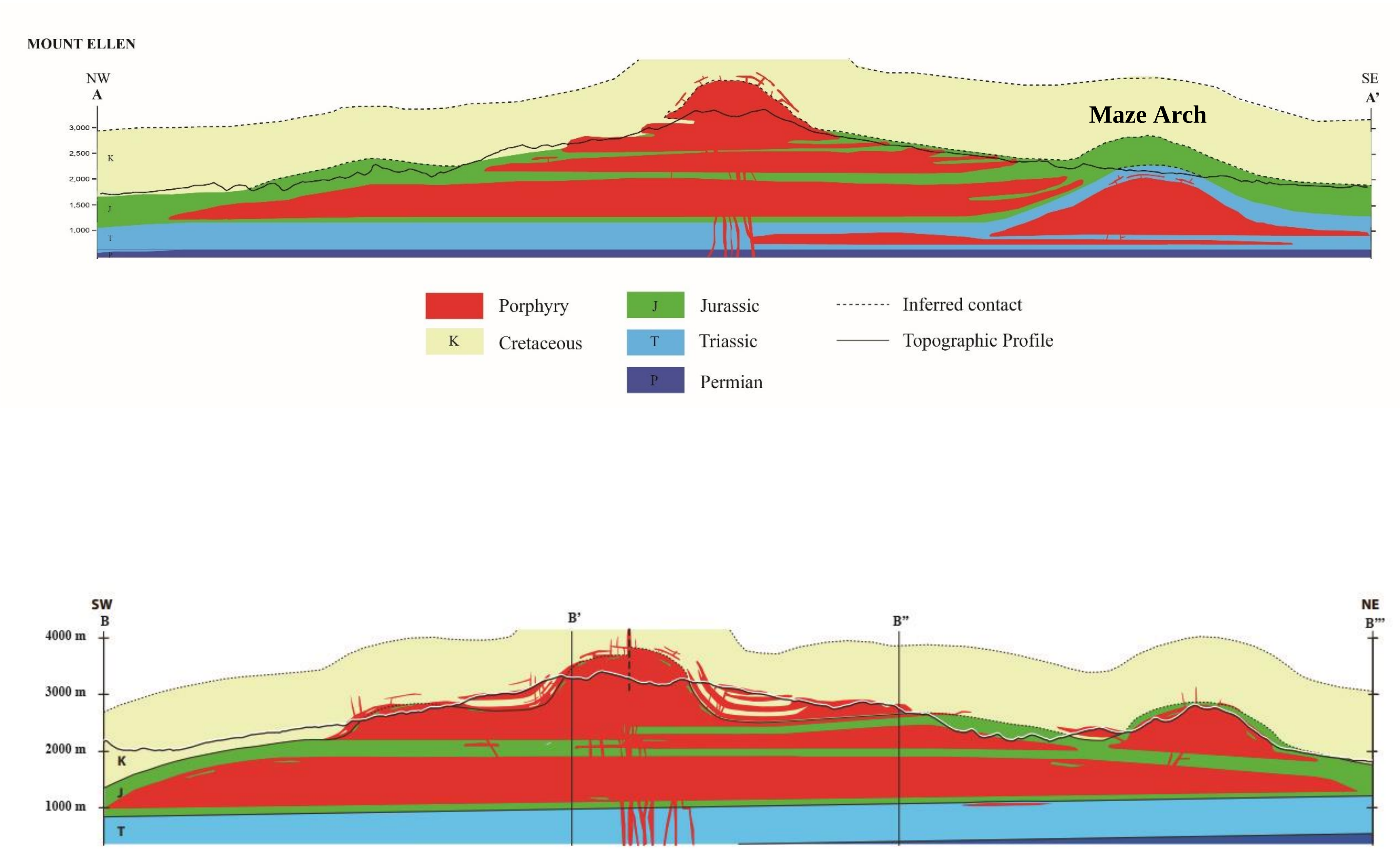

Figure 38. Cross sections (transects from figure 26) of Mount Ellen with no vertical exaggeration. Rock colors correlate with those from figure 26. Thick black lines show modern topography. Cross section A-A’ shows NW to SE profile. Cross section B-B’’’ shows SW to NE profile (modified from Horsman et al., 2018).

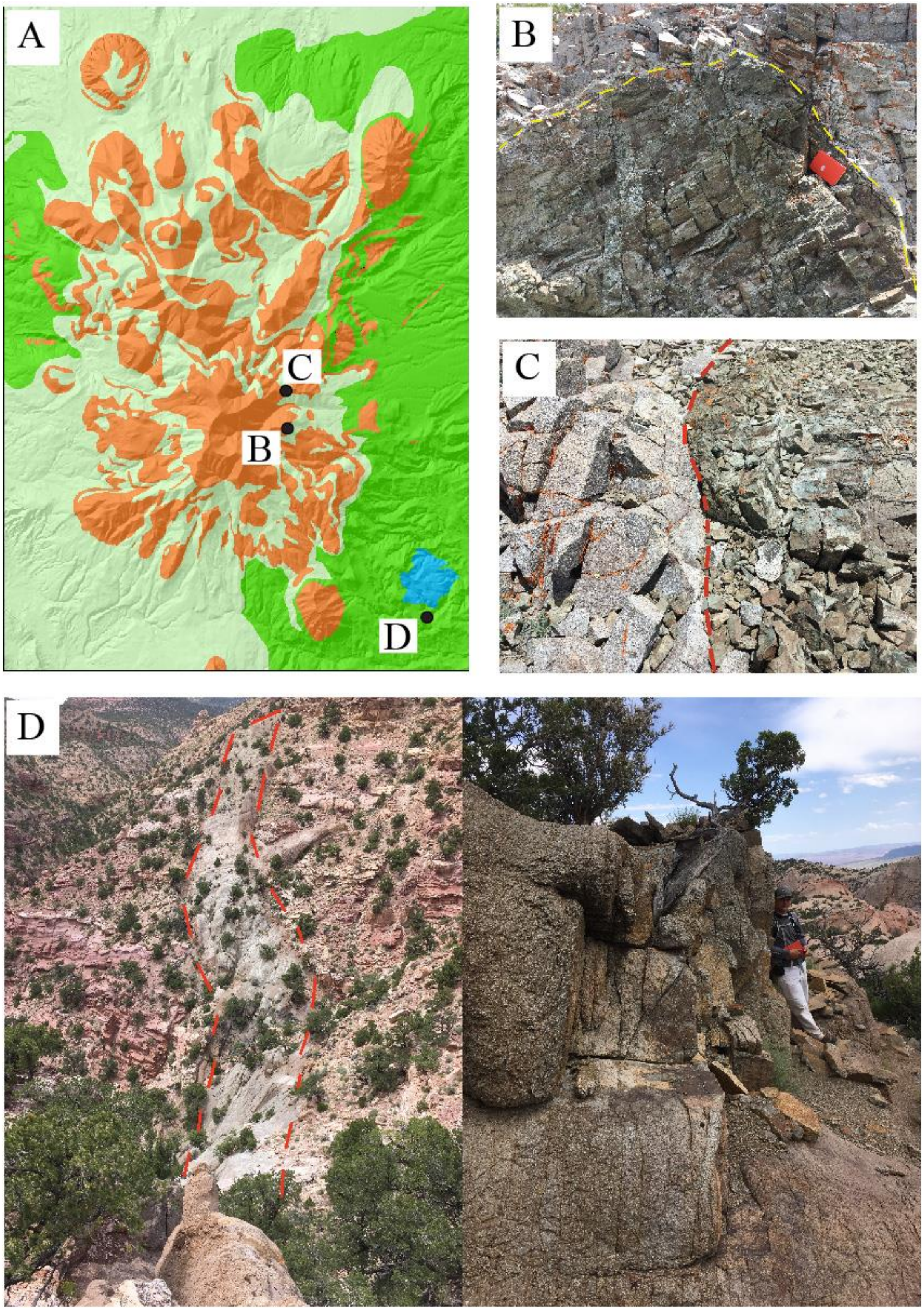

Figure 39. **A.** Geologic map of Mount Ellen with photo location points. **B**. and **C.** demonstrating contacts between sedimentary strata on the left and igneous rock on the right. **D.** A dike exposed in the Maze Arch with a view of the dike across a drainage (left photo) and an up-close photo of dike on other side of drainage (right photo). Note: dashed lines in photos highlight contact.

7.2 Lab Analysis and Data Compilation

With the addition of data from newly collected samples and data from previous studies, this new suite of data includes 72 samples for geochemistry (Fig. 40), 85 samples for AMS (Fig. 41), and 33 samples for CSD (Fig. 42). All sample locations were plotted on a geologic map of Mount Ellen using ArcGIS to show location and spatial distribution. Most samples are located on the eastern portion of Mount Ellen, where more roads allow better access.

As one means of distinguishing between possible distinct magma bodies, all samples were grouped based on their texture, as described in section 5.5, Crystal Size Distribution. These 5 texture groups (Fig. 43 & 44) are used as a basis to compare results from other methods applied to analyzing component intrusions within the Mount Ellen intrusive complex throughout this study. Each texture is plotted with a consistent color throughout all figures in this study. Texture 1 is red, Texture 2 is blue, Texture 3 is yellow, Texture 4 is orange, and Texture 5 is purple (Fig. 44). It's important to note, that all samples grouped into Texture 5 are considered the outliers. These samples did not fit within one of the other four textural groups. Additional work would need to be performed to determine further textural classification for these samples.

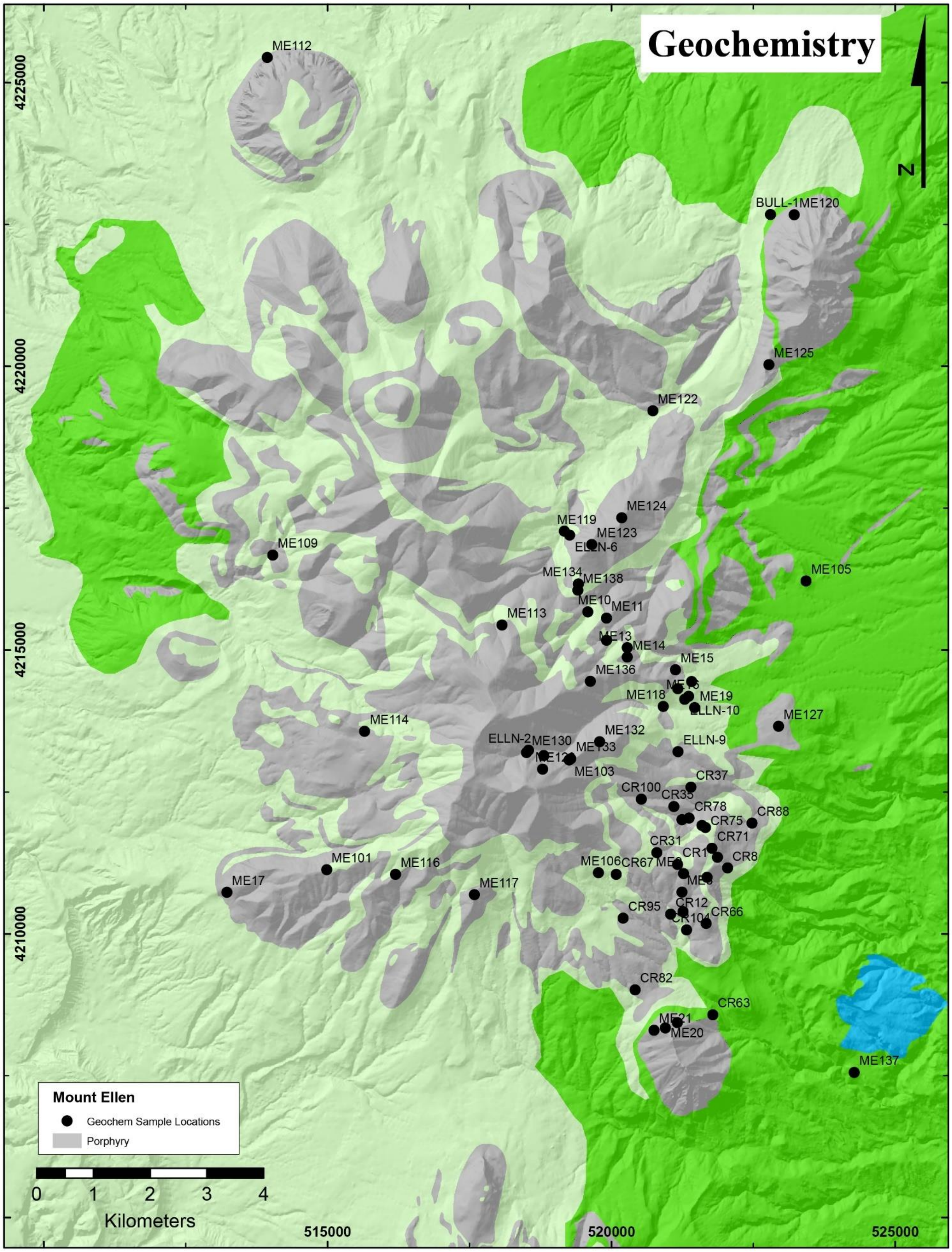

Figure 40. Map of Mount Ellen intrusive complex with locations for all geochemistry samples (72 samples). UTM coordinates, zone 12, datum NAD83.

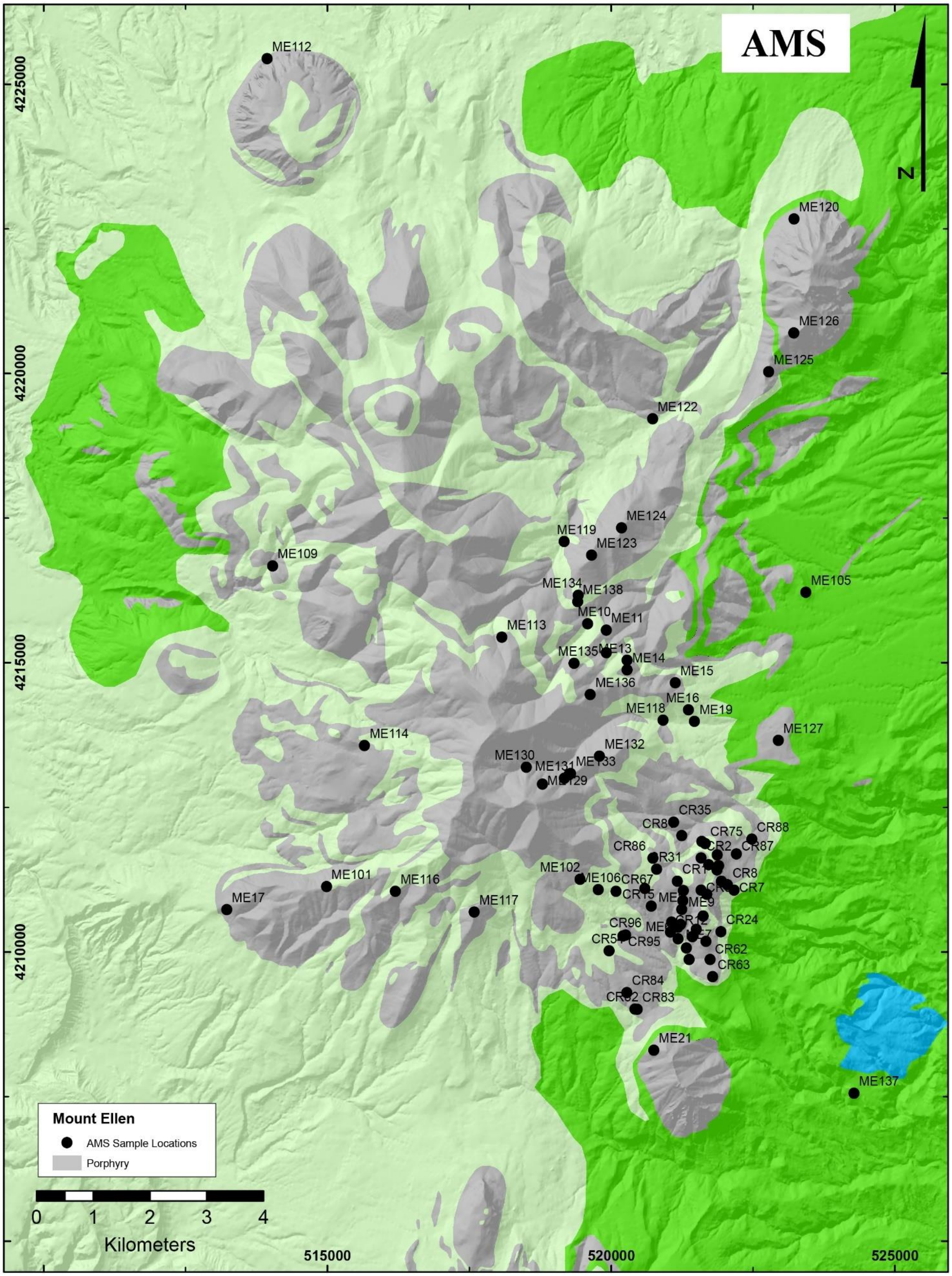

Figure 41. Map of Mount Ellen intrusive complex with locations for all AMS samples (85 samples). UTM coordinates, zone 12, datum NAD83.

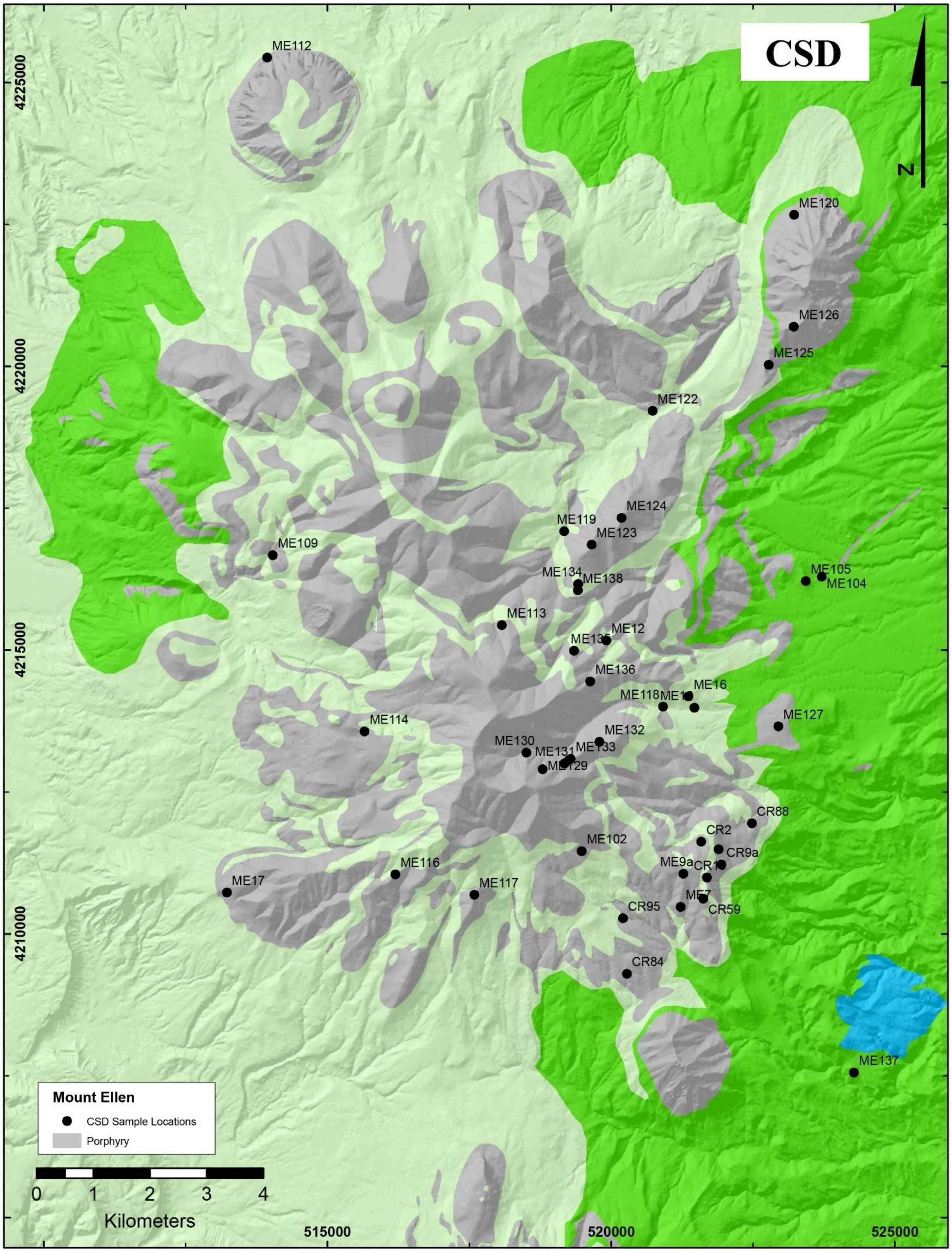

Figure 42. Map of Mount Ellen intrusive complex with locations for all CSD samples (33 samples). UTM coordinates, zone 12, datum NAD83.

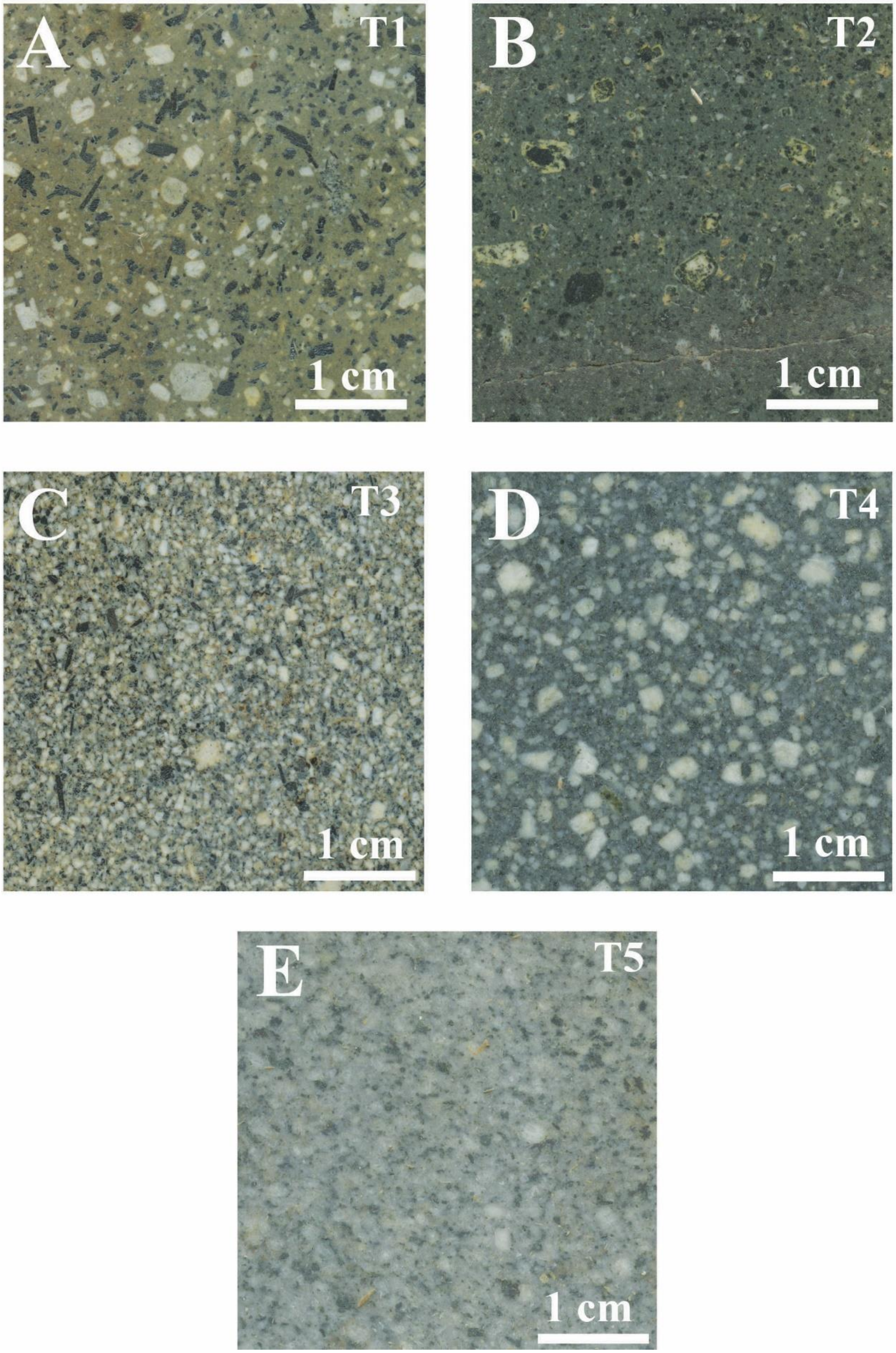

Figure 43. Representative images of each textural group. 4 cm by 4 cm sections of each texture analyzed by CSD. **A.** Texture 1, **B.** Texture 2, **C.** Texture 3, **D.** Texture 4, **E.** Texture 5.

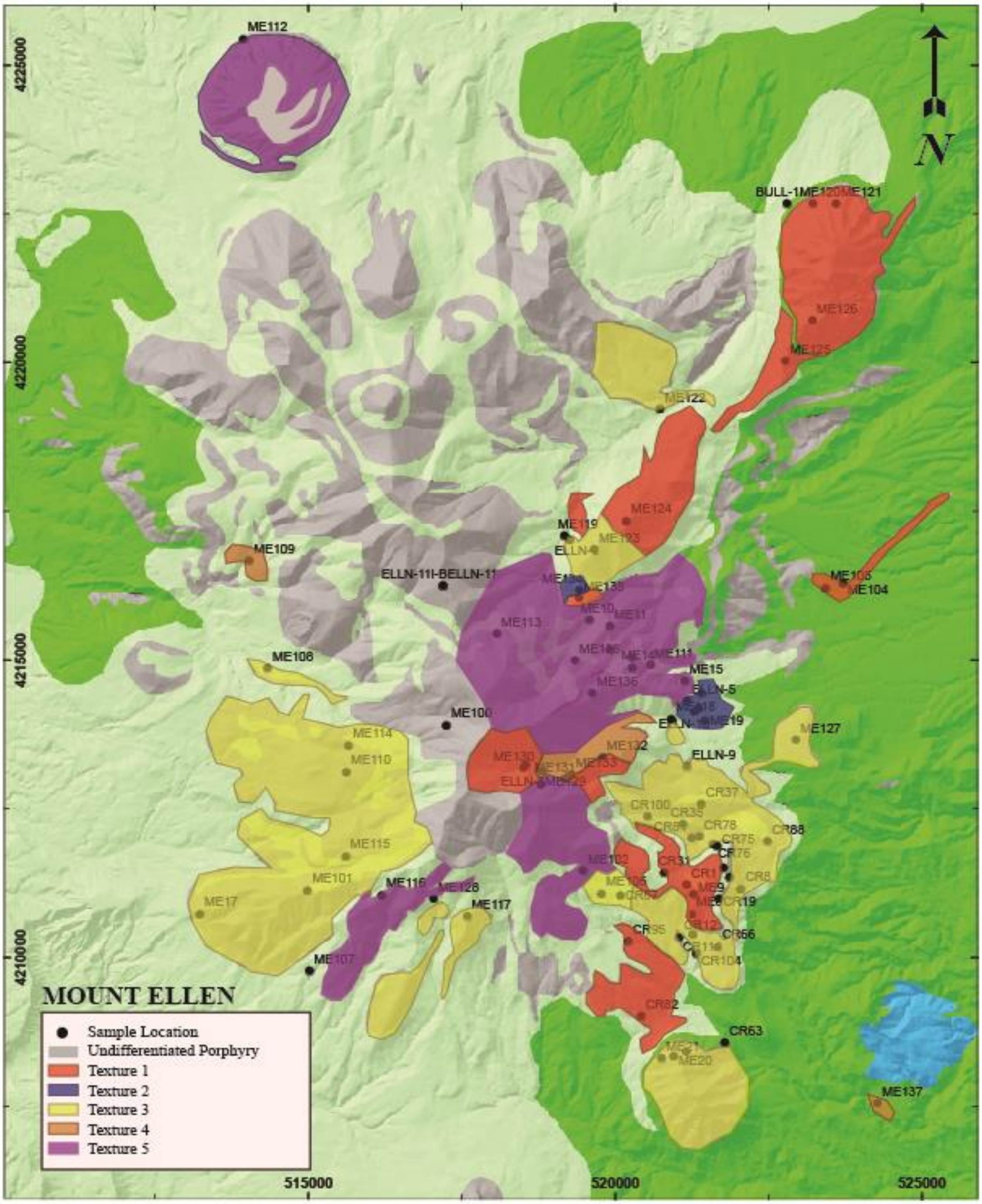

Figure 44. Geologic map of Mount Ellen with overlay of the five textural groups. Greens and blues represent sedimentary strata. UTM coordinates, zone 12, datum NAD83.

The modal abundance for phenocrysts and matrix in each texture group was determined by analyzing the rock slabs used for CSD. Using the ImageJ software, the percentage of area that the crystals occupied was calculated for each slab image. The average abundance of crystals for all rock slabs within each texture group was used to determine the overall modal abundance for each texture group and can be found in Table 1. Igneous rocks exhibiting texture 1 have plagioclase crystals up to 11 mm, and hornblende crystals up to 10 mm. Xenoliths are not present for this texture. (Fig. 43A). Texture 2 has the lowest phenocryst abundance for both plagioclase and hornblende crystals. Plagioclase crystals are up to 3 mm in size, and hornblende crystals up to 8 mm, bounded by a dark gray to black matrix (Fig. 43B). Xenoliths are also not present for this texture. Texture 3 is phenocryst rich with plagioclase crystals up to 6 mm, and hornblende crystals up to 5.5 mm (Fig. 43C). Few xenoliths are present within texture 3 igneous rock samples and have a size up to 13 mm. Texture 4 has less plagioclase crystals present. Hornblende crystals are far less ubiquitous. Plagioclase crystals are up to 5 mm in size and 3 mm for hornblende crystals (Fig. 43D). Texture 4 appears to have a higher abundance of xenoliths up to 6 mm in size. Texture 5 has plagioclase crystals up to 4 mm and hornblende crystals up to 2.5 mm (Fig. 43E). Several xenoliths are present, and this texture group presents the largest size xenoliths, up to 27 mm in diameter.

Table 1. Phenocryst modal abundance and characteristics

Phenocryst Modal Abundance by Texture					
	Texture 1	Texture 2	Texture 3	Texture 4	Texture 5
Plagioclase Phenocrysts	18%	3%	18%	15%	21%
Hornblende Phenocrysts	17%	5%	16%	11%	7%
Matrix %	65%	92%	66%	74%	72%
Matrix Color	Medium Gray	Dark Gray to Black	Light Gray	Dark Gray	Light Gray
Plagioclase Crystal Shape	Subhedral, Euhedral	Euhedral	Euhedral	Subhedral, Euhedral	Euhedral
Hornblende Crystal Shape	Euhedral, Bladed	Euhedral	Euhedral, Bladed	Euhedral	Euhedral

7.3 Geochemistry

All geochemical data can be found in Appendix A. Geochemistry data for all 72 samples are plotted on a total alkali versus silica diagram (Le Bas et al., 1986) to examine the geochemical composition for each sample based on their textural groups (Fig. 45). The suite of data resulted in the SiO_2 contents ranging from 51.17% to 67.89% with an average weight percentage of 58.22%. The $Na_2O + K_2O$ content ranges from 4.25% to 8.42% with an average weight percentage of 6.01% (Table 2). The samples generally plot along the boundary of silica saturated and silica oversaturated. Textures 1 and 4 predominantly plot along the andesite/trachyandesite boundary. Texture 1 has a few samples that plot within the dacite field. Textures 3 and 5 have a broader range of compositions ranging from basalt to dacite. Texture 5 tends to have more samples that are basaltic in composition and texture 3 shows the greatest variation from basalt to dactite. Texture 2 plots predominantly within the basalt field, with one sample in the trachyandesite field. There is generally overlap in silica concentrations between all texture groups. However, samples for Texture 2 and Texture 4 cluster separately from one another due to their differences in SiO_2 concentrations (Fig. 46) although these two textures have the least number of samples. The range of SiO_2 percentage and $Na_2O + K_2O$ percentage for each individual texture can be found in Table 2. On average, Texture 2 has the lowest SiO_2 percentage; Texture 4 has the greatest SiO_2 percentage; Texture 2 has the lowest $Na_2O + K_2O$ percentage; and Texture 4 has the greatest $Na_2O + K_2O$ percentage.

It's important to note that of the 72 samples plotted on the total alkali versus silica diagram, 11 samples are from Nelson & Davidson (1993). To classify these samples within the textural groups classified for this study, their samples were assigned to texture groups based on their sample locations and their proximity to samples with a known textural group. Of the 11 samples, 3 were classified as Texture 1, 3 as Texture 3, and 5 as Texture 5 (as these samples were not within proximity to a known sample with a classified texture).

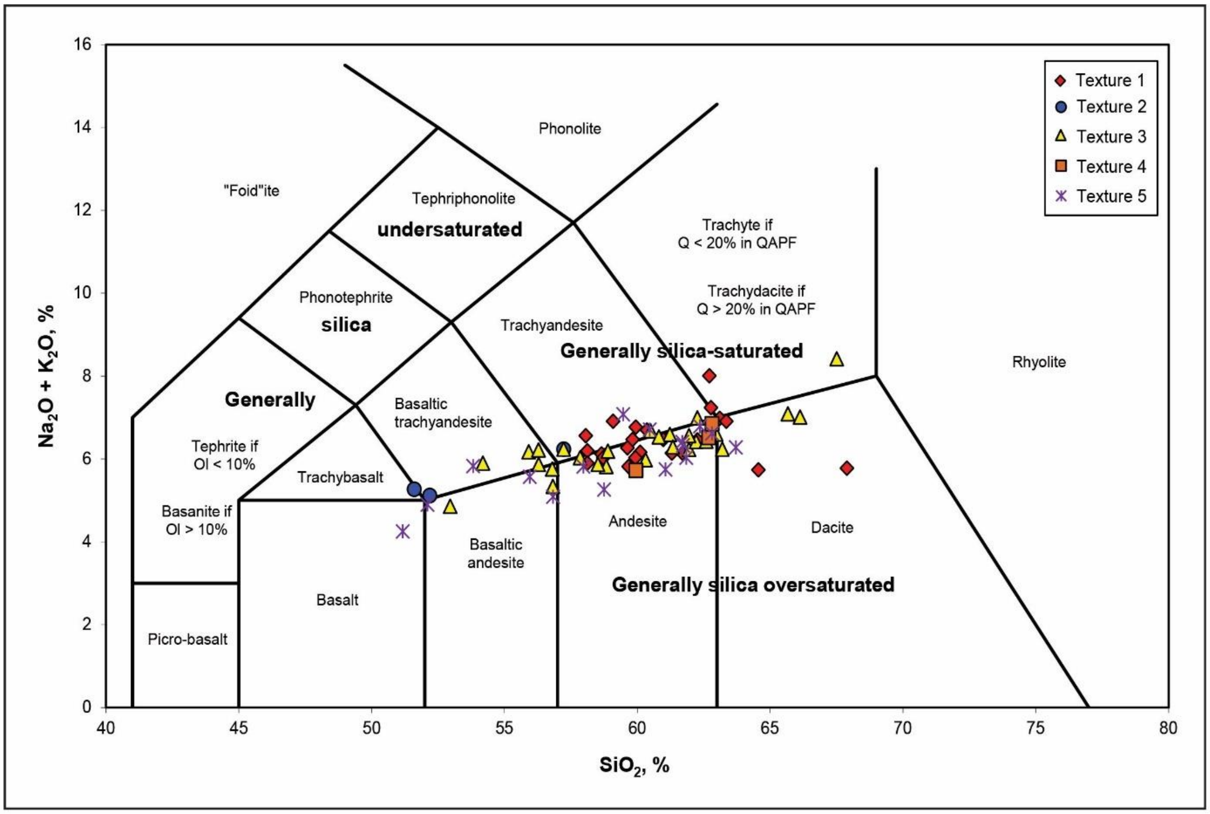

Figure 45. Total alkalis (Na2O+K2O) vs. silica (SiO2) diagram (Le Bas et al., 1986) for 72 samples: 24 from Texture 1, 3 from Texture 2, 26 from Texture 3, 3 from Texture 4, and 16 from Texture 5.

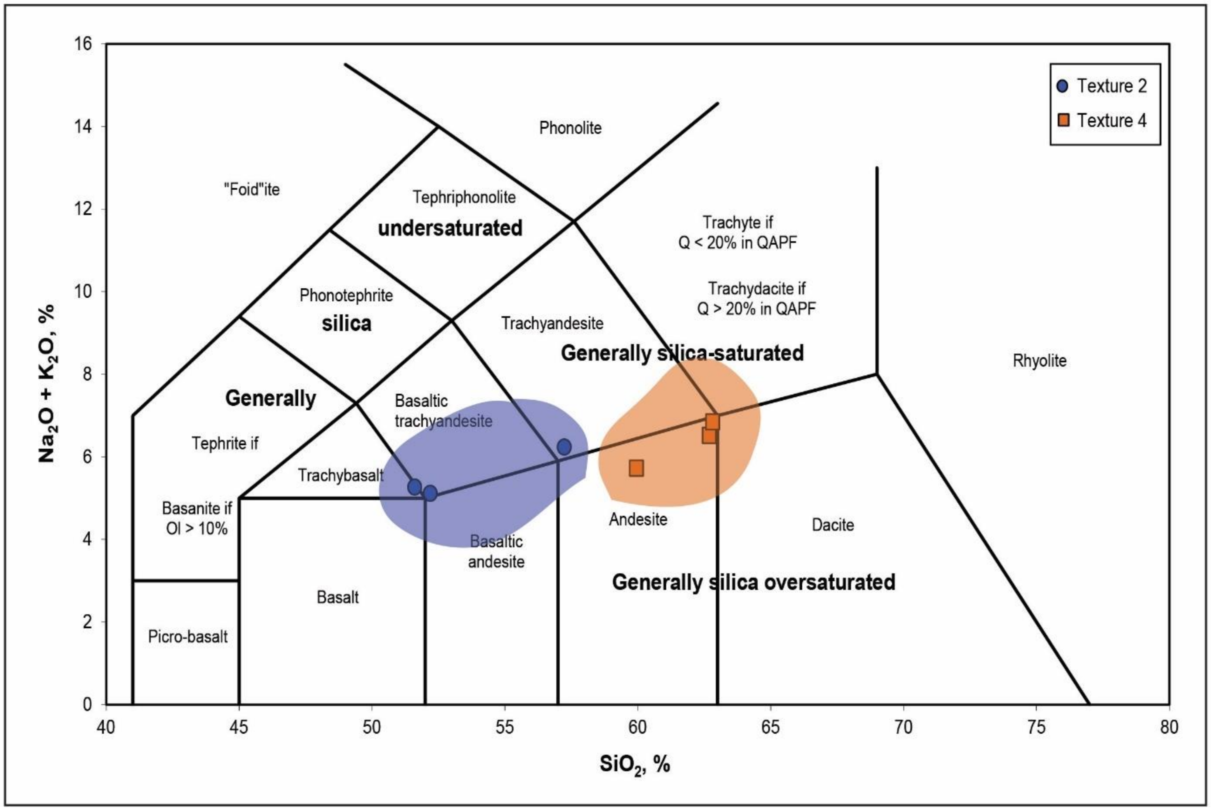

Figure 46. Total alkalis (Na2O+K2O) vs. silica (SiO2) diagram (Le Bas et al., 1986) demonstrating distinct cluster separation of Texture 2 and Texture 4.

Table 2. Silica (SiO2) and Total alkalis (Na2O+K2O) percentages for all five texture groups.

Resulting Data by Texture					
	# of samples	SiO_2 % range	Na_2O+K_2O % range	Average SiO_2%	Average Na_2O+K_2O
Texture 1	24	58.06 - 67.89	5.74 - 8.01	60.98	6.43
Texture 2	3	51.60 - 57.23	5.12 - 6.24	53.67	5.54
Texture 3	26	52.96 - 67.51	4.86 - 8.42	60.15	6.31
Texture 4	3	59.94 - 62.81	5.73 - 6.85	61.81	6.37
Texture 5	16	51.17 - 63.71	4.25 - 7.08	58.86	5.92

Major and trace element concentrations are plotted against total silica weight percent on Harker diagrams (Fig. 47): three oxides, three LILE (large ion lithophile elements), and three HFSE (high field strength elements). Not all texture groups can be differentiated from one another by composition; however, samples for Texture 2 and Texture 4 do show a distinction in SiO_2 concentrations. Texture 2 consistently has a lower SiO_2 concentration for all plots than Texture 4. For CaO, Th, and U concentrations, Texture 2 is more enriched than Texture 4. Nelson & Davidson (1993) samples were not included within the trace element diagrams due to lack of data.

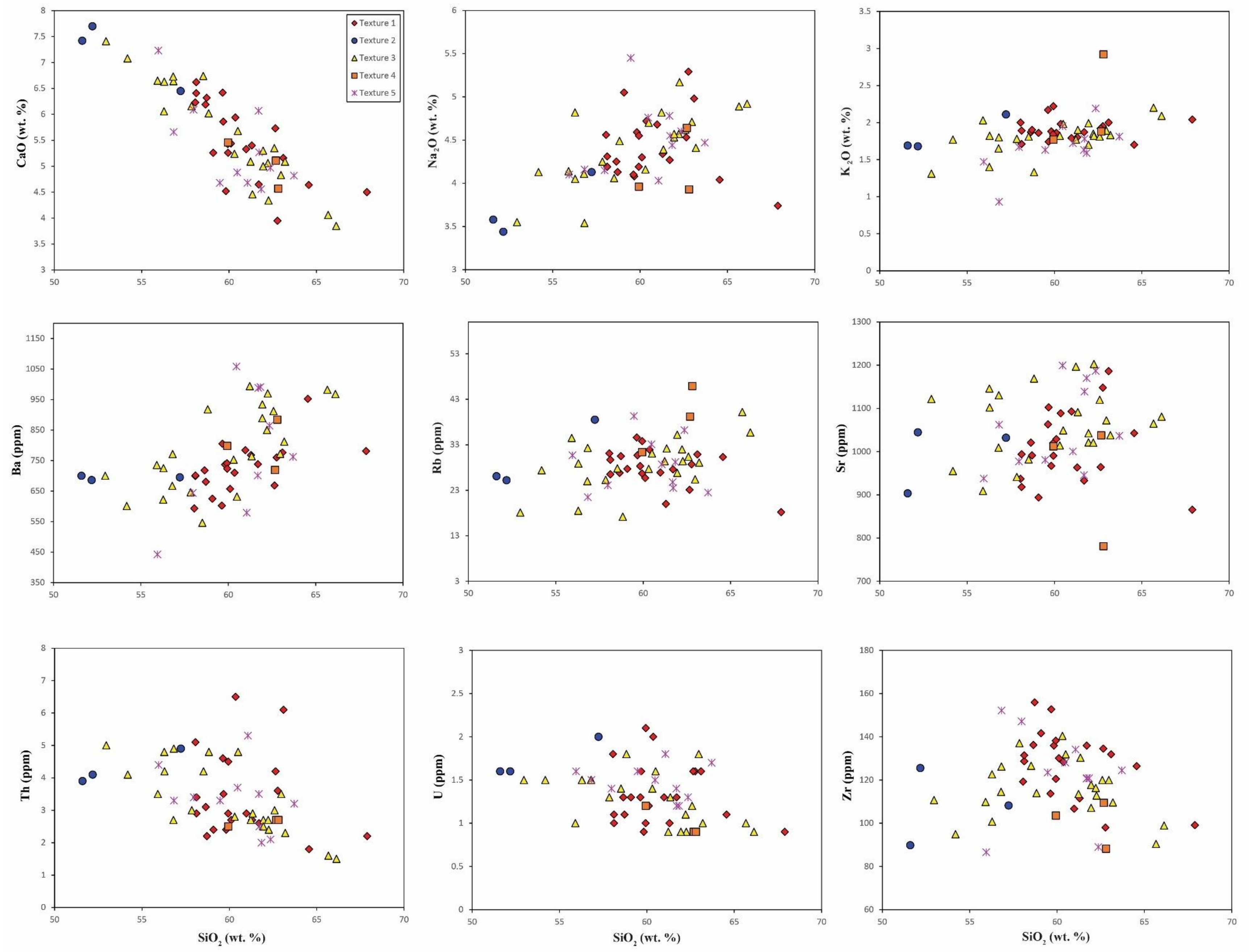

Figure 47. Harker diagram showing major and trace element concentrations vs. SiO2 for all five textures. Elements plotted versus silica include as followed: CaO, Na$_2$O, K$_2$O, Ba, Rb, Sr, Th, U, and Zr.

Rare earth elements (REE) are averaged for each texture and normalized to CI-Chondrite (Fig 48A) (McDonough and Sun, 1995) to observe variation between textures. The error bars plotted on each texture group plot represent one standard deviation. All textures show a general decrease in abundance from light to heavy REEs. Textures 1, 3, and 5 have no apparent trend that would distinguish a compositional difference between REEs. However, Textures 2 and 4 show a clear distinction in REE abundance (Fig. 48B). Texture 2 has a higher silica content and higher concentrations of REEs. All five textures have lower concentrations of heavy REE and there is no Eu anomaly. All samples were plotted individually to also observe variations (Fig. 49).

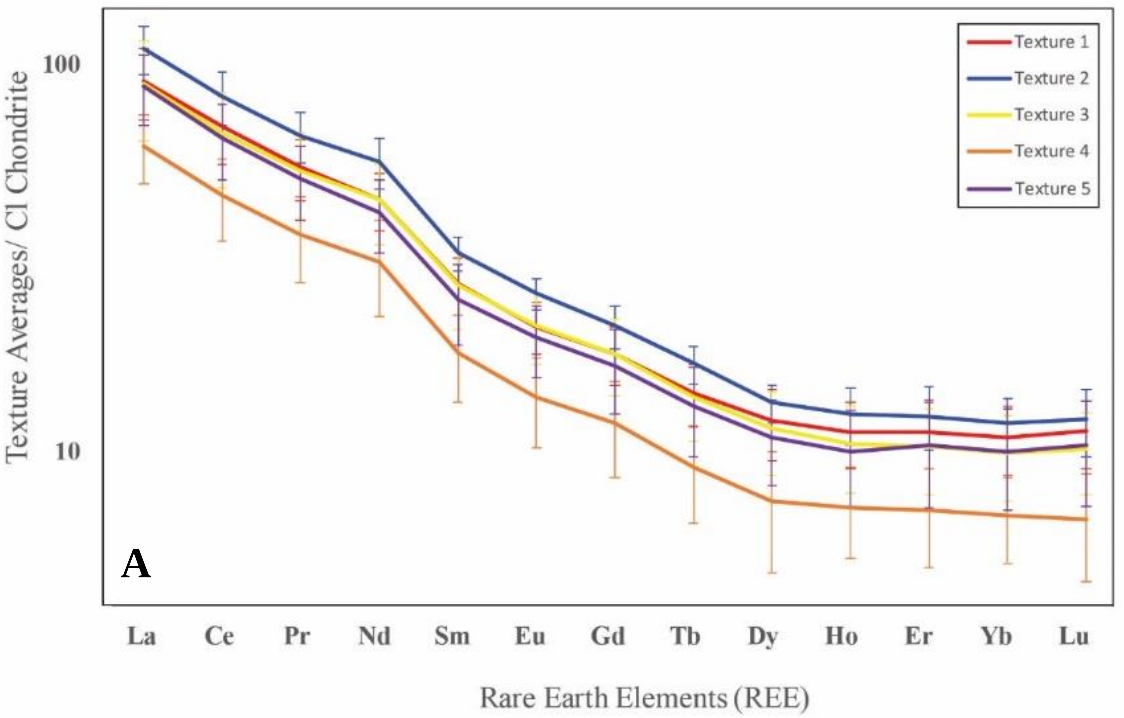

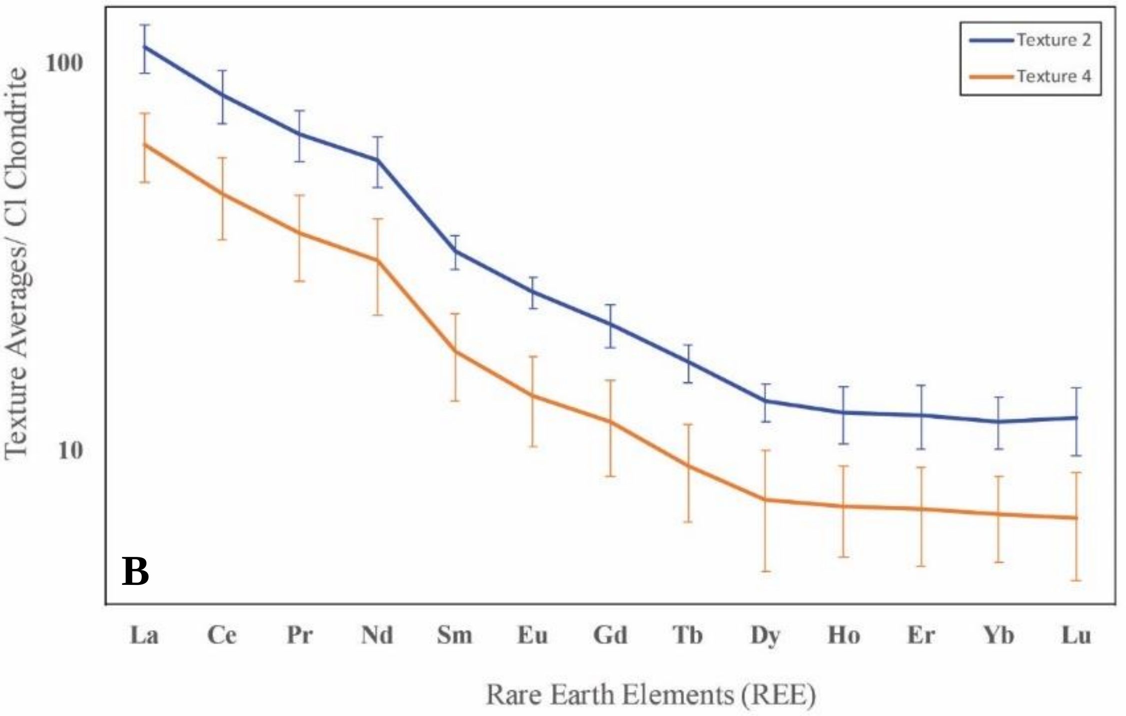

Figure 48. **A.** Chondrite-normalized (McDonough and Sun, 1995) REE plots for averages of all five texture groups. Error bars represent one standard deviation for each element in both the positive and negative direction. **B.** Isolated REE plot for Textures 2 and 4, demonstrating no overlap in data.

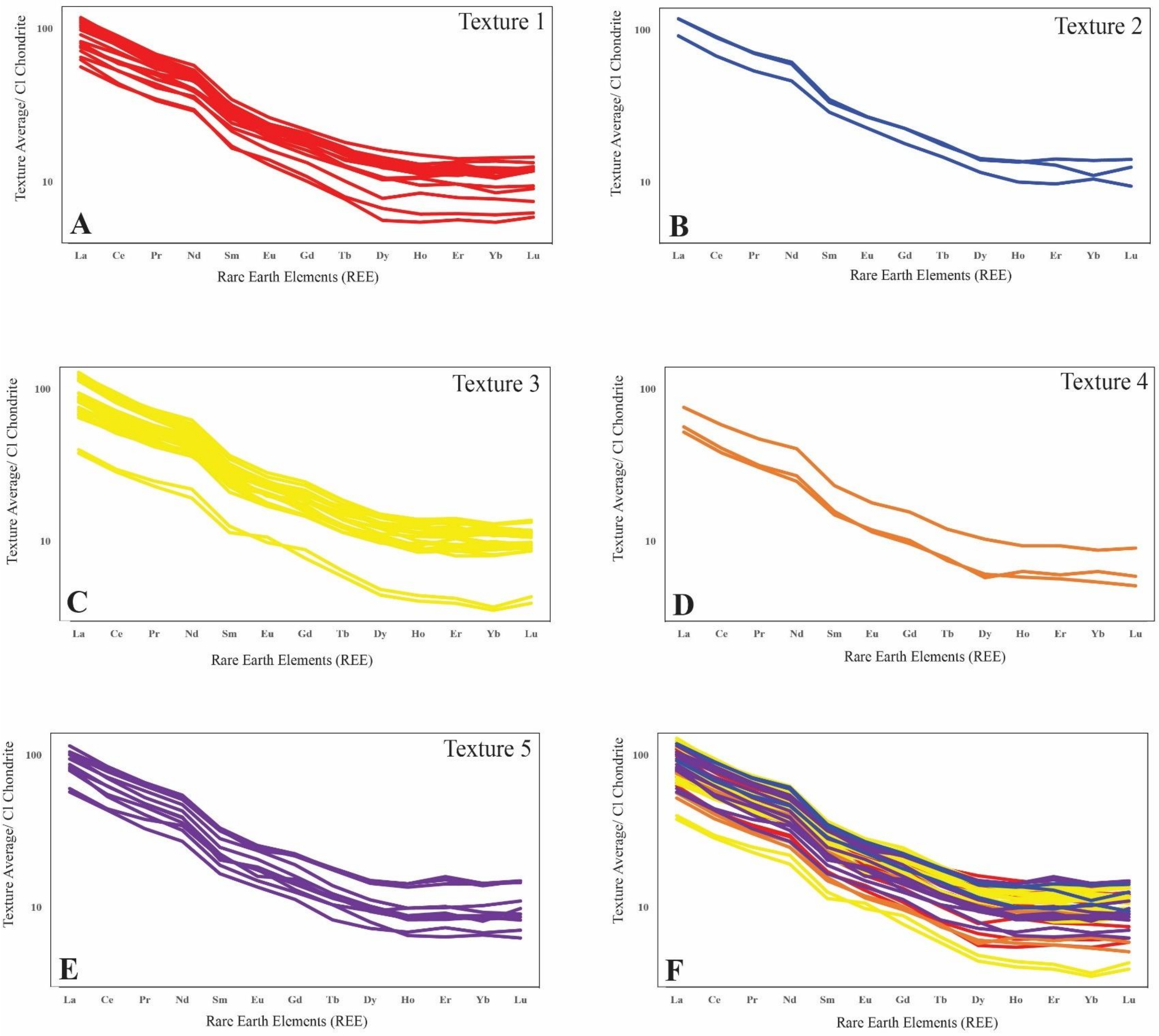

Figure 49. Chondrite-normalized (McDonough and Sun, 1995) REE plots for the **A:** Texture 1, **B:** Texture 2, **C:** Texture 3, **D:** Texture 4, E: Texture 5, and **F:** all textures combined to show range.

7.4 Anisotropy of Magnetic Susceptibility

AMS data for all samples can be found in Appendix B. Mean susceptibility values (Table 3) for Texture 1 range from 2.24×10^{-4} SI to 7.53×10^{-2} SI, with an average of 1.94×10^{-2} SI, and a standard deviation of 1.84×10^{-2} SI. Mean susceptibility values for Texture 2 range from 1.77×10^{-2} SI to 5.31×10^{-2} SI, with an average of 3.17×10^{-2} SI, and a standard deviation of 1.54×10^{-2} SI. For Texture 3, values range from 1.52×10^{-4} SI to 8.17×10^{-2} SI, with an average of 1.98×10^{-2} SI, and a standard deviation of 1.75×10^{-2} SI. For texture 4, values range from 2.99×10^{-4} SI to 1.14×10^{-2} SI, with an average of 7.04×10^{-3} SI, and a standard deviation of 1.15×10^{-3} SI. For Texture 5, values range from 1.97×10^{-4} SI to 3.54×10^{-2} SI, with an average of 9.54×10^{-3} SI, and a standard deviation of 1.06×10^{-2} SI.

Not all texture groups can be differentiated from one another with mean susceptibility (K_m) values. However, a difference in mean susceptibility values exists between Texture 2 and Texture 4 as seen in Figure 50. The minimum mean susceptibility value for Texture 2 is greater than the maximum mean susceptibility value for Texture 4. The limited number of samples for both these textures makes the statistical significance questionable. However, further evaluation of scalar parameters show that the shape factor (T) and the foliation (F) values are different at one standard deviation (Fig. 51) between Texture 2 and Texture 4.

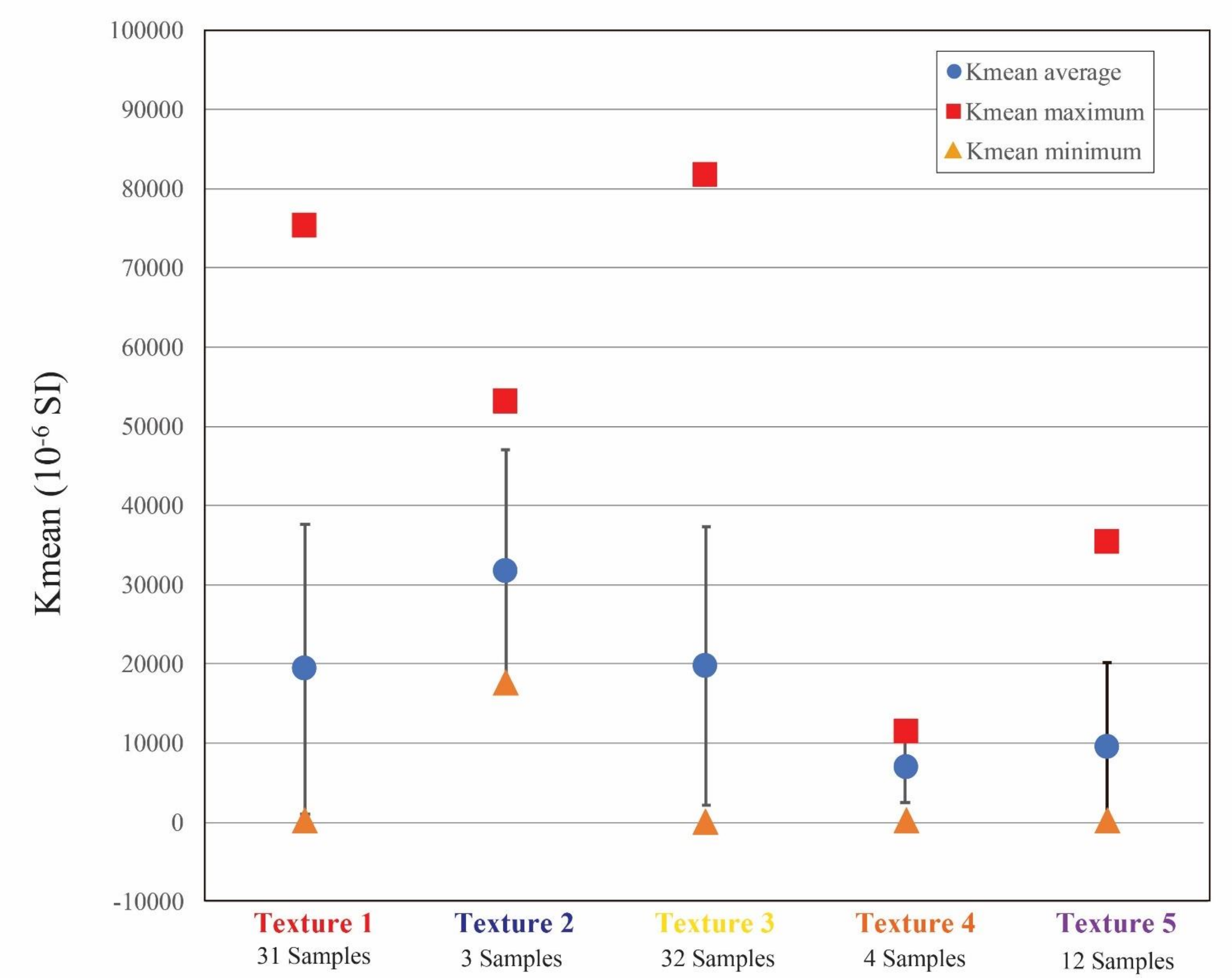

Figure 50. Mean Susceptibility plots for averages of all five textures. Error bars show one standard deviation.

To consider spatial variability, mean susceptibility values for all samples were plotted on a geologic map. These values were then interpolated using the natural neighbor function of ArcGIS and then contoured using a value of 0.005 (Fig. 52). The contoured mean susceptibility values, to a first order, demonstrate lobate geometries that are distributed around and radiate away from the central intrusive body.

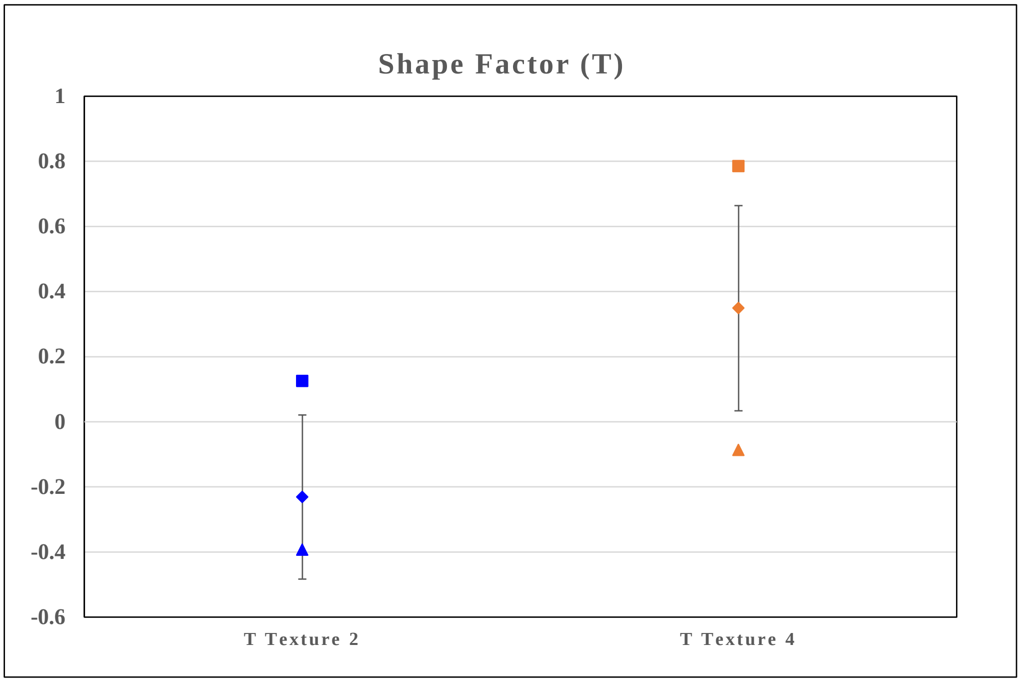

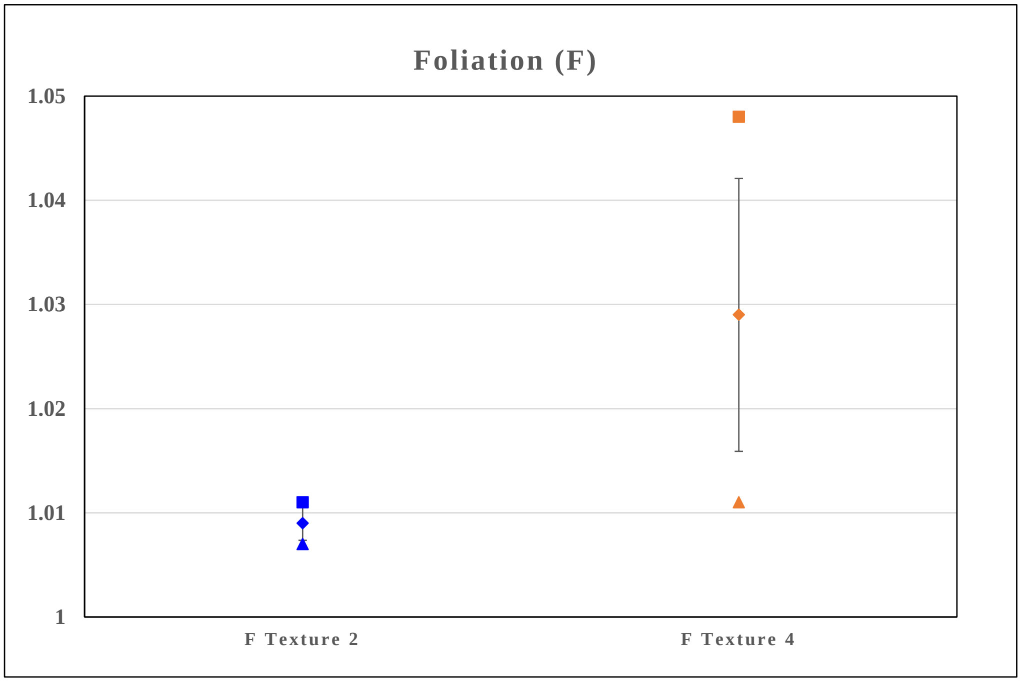

Figure 51. Plots demonstrating differences between Texture 2 and Texture 4 values for shape parameter (T) values (top) and foliation (F) values (bottom).

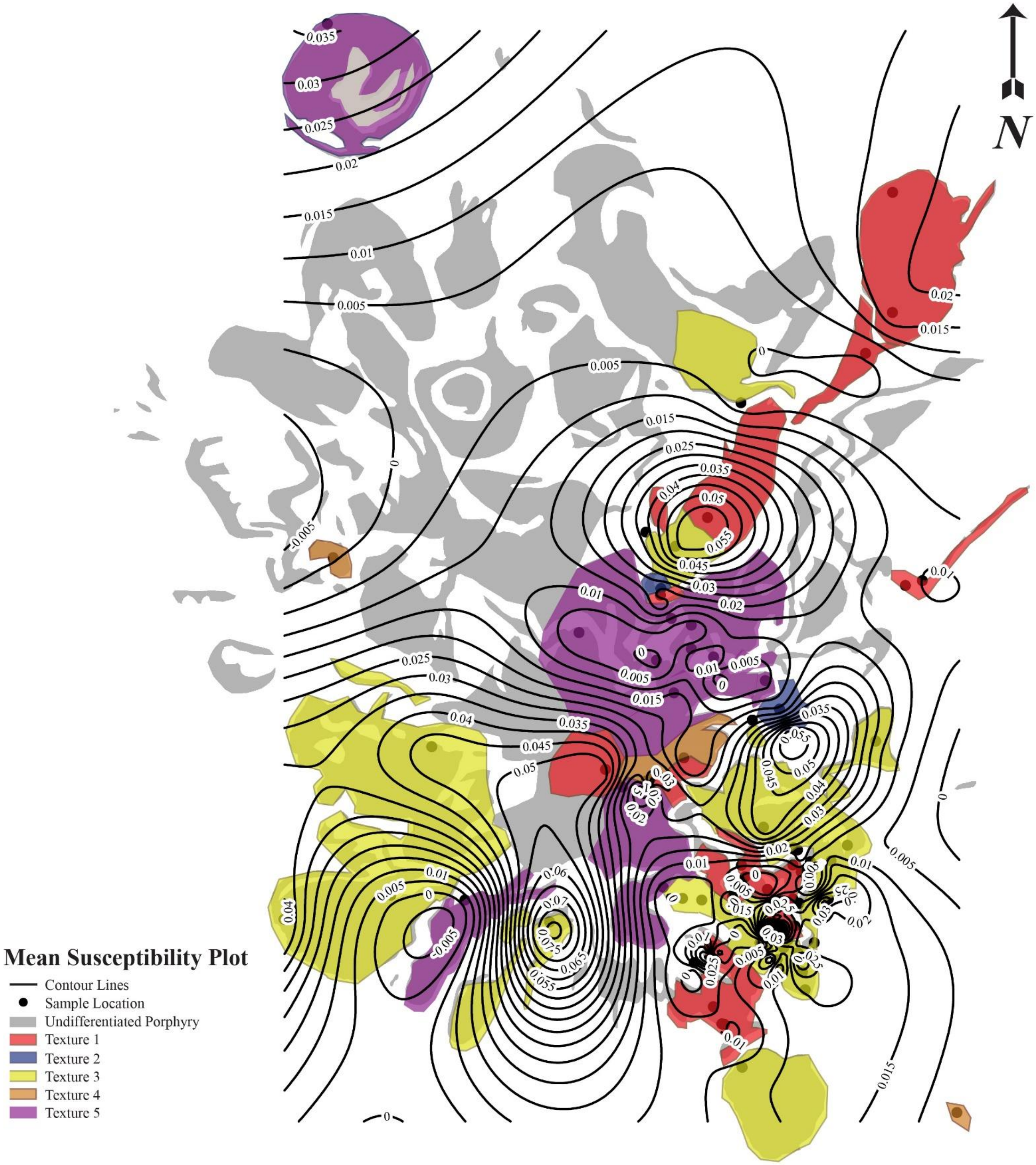

Figure 52. Contour map demonstrating spatial distribution of mean susceptibility (SI units) of collected samples. Interpolated with natural neighbor function in ArcGIS and contoured with an interval of 0.005.

AMS scalar parameters (Table. 3) are plotted for all samples within each texture group in Figure 46. The degree of anisotropy (P_j) for Texture 1 ranges from 1.013 to 1.055, with an average of 1.029, and a standard deviation of 0.010. For Texture 2, values range from 1.016 – 1.038, with an average of 1.026, and a standard deviation of 0.009. For Texture 3, values range from 1.013 to 1.084, with an average of 1.062, and a standard deviation of 0.014. For Texture 4, values range from 1.020 to 1.067, with an average of 1.047, and a standard deviation of 0.020. For Texture 5, values range from 1.014 to 1.104, with an average of 1.034, and a standard deviation of 0.022 (Fig. 53A, B).

Shape factor values (T) for Texture 1 range from -0.818 to 0.675, with an average of 0.045 and a standard deviation of 0.358. For Texture 2, values range from -0.393 to 0.125, with an average of -0.231 and a standard deviation of 0.252. For Texture 3, values range from -0.397 to 0.708, with an average of 0.142 and a standard deviation of 0.260. For Texture 4, values range from -0.087 to 0.785, with an average of 0.349 and a standard deviation of 0.315. For Texture 5, values range from -0.350 to 0.230, with an average of 0.020 and a standard deviation of 0.193 (Fig. 53B, C). For Texture 1, samples appear to be distributed as 50% prolate and 50% oblate. Texture 2 shows two samples that are prolate and one sample that is oblate. Texture 3 appears to be predominantly oblate with several prolate samples. Texture 4 has four samples that are oblate and one sample that is prolate. Texture 5 appears to also be distributed as 50% prolate and 50% oblate.

Lineation (L) values for Texture 1 range from 1.003 to 1.041, with an average of 1.013, and a standard deviation 0.007. For Texture 2, values range from 1.007 – 1.026, with an average of 1.016, and a standard deviation of 0.008. For Texture 3, values range from 1.003 to 1.032, with an average of 1.044, and a standard deviation of 0.007. For Texture 4, values range from

1.004 to 1.035, with an average of 1.015, and a standard deviation of 0.012. For Texture 5, values range from 1.006 to 1.054, with an average of 1.017, and a standard deviation of 0.012. Lineation values are plotted against Foliation (*F*) values for all samples (Fig. 53D). Foliation values for Texture 1 range from 1.004 to 1.042, with an average 1.015, and a standard deviation of 0.008. For Texture 2, values range from 1.007 to 1.011, with an average of 1.009, and a standard deviation of 0.002. For Texture 3, values range from 1.007 to 1.047, with an average of 1.016, and a standard deviation of 0.008. For Texture 4, values range from 1.011 to 1.048, with an average 1.029, and a standard deviation of 0.013. For Texture 5, values range from 1.009 to 1.043, with an average of 1.016, and a standard deviation of 0.009.

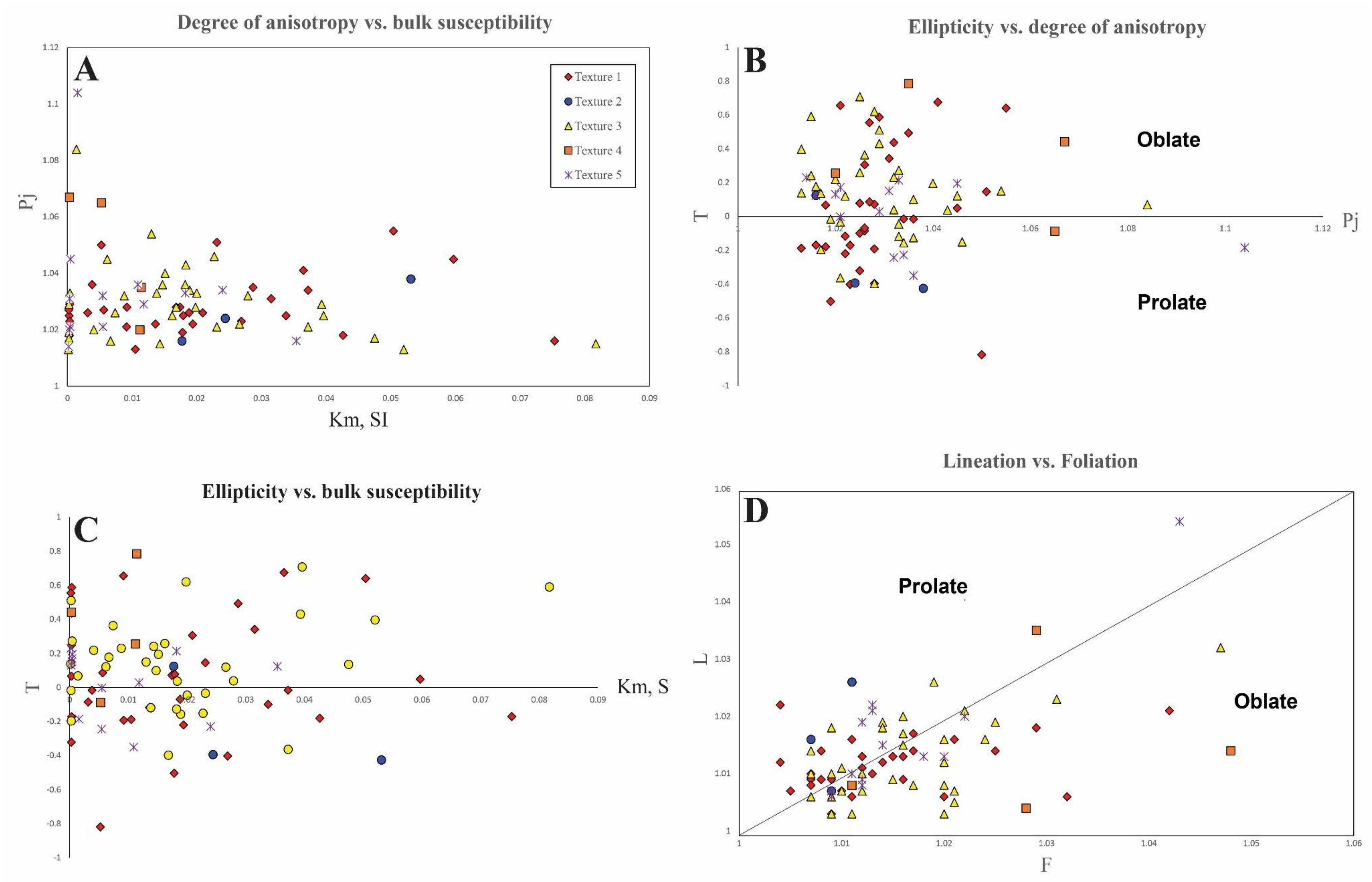

Figure 53. AMS scalar parameters plotted for all five texture groups. **A.** Corrected degree of anisotropy versus mean bulk susceptibility. **B.** Shape factor versus corrected degree of anisotropy. **C.** Shape factor versus mean bulk susceptibility. **D.** Lineation versus foliation

Table 3. Summary of scalar AMS data for each texture including mean susceptibility values for each texture and scalar parameter range values for Lineation (*L*), Foliation (*F*), Corrected degree of anisotropy (P_j), and Shape factor (*T*). For each parameter the average (Avg.) and standard deviation (Std.) are included.

Resulting AMS Data					
	Texture 1	**Texture 2**	**Texture 3**	**Texture 4**	**Texture 5**
# of Samples	**33**	**3**	**32**	**4**	**12**
K_min	2.24E-04	1.77E-02	1.52E-04	2.99E-04	1.97E-04
K_max	7.53E-02	5.31E-02	8.17E-02	1.14E-02	3.54E-02
K_mean	1.94E-02	3.17E-02	1.98E-02	7.04E-03	9.54E-03
Std.	1.84E-02	1.54E-02	1.75E-02	1.15E-03	1.06E-02
L	1.003 - 1.041	1.007 - 1.026	1.003 - 1.032	1.004 - 1.035	1.006 - 1.054
Avg.	1.013	1.016	1.013	1.015	1.017
Std.	0.007	0.008	0.007	0.012	0.012
F	1.004 - 1.042	1.007 - 1.011	1.007 - 1.047	1.011 - 1.048	1.009 - 1.043
Avg.	1.015	1.009	1.016	1.029	1.016
Std.	0.008	0.002	0.008	0.013	0.009
Pj	1.013 - 1.055	1.016 - 1.038	1.013 - 1.084	1.020 - 1.067	1.014 - 1.104
Avg.	1.029	1.026	1.030	1.047	1.034
Std	0.010	0.009	0.014	0.020	0.022
T	-0.818 - 0.675	-0.393 - 0.125	-0.397 - 0.708	-0.087 - 0.785	-0.350 - 0.230
Avg.	0.045	-0.231	0.137	0.349	0.018
Std.	0.358	0.252	0.260	0.315	0.193

7.5 Crystal Size Distribution

7.5.1 Hornblende Phenocrysts

All CSD data can be found in Appendix C. Plots of CSD slopes for hornblende phenocrysts are displayed by texture and a combined plot including all textures (Fig. 54). Generally, hornblende phenocrysts do not exceed 5 mm in size, except for two samples from Texture 1 and one sample from Texture 5. The hornblende CSD slopes are broadly consistent across textures with a steep slope below 1 mm in size (late cooling) and a more gradual slope above 1 mm in size (early cooling).

To further investigate and compare each textural group, averages for all CSDs, by texture, were plotted and analyzed using linear regression (Fig. 55). The resulting data (Table. 4) produced a trendline with a slope and y-intercept for the early stage and late stage component for each texture. The slope corresponds to the characteristic crystal length (equation 10), for each component, and the y-intercept corresponds to nucleation density (equation 9) of the texture.

Plotting the characteristic crystal length versus the nucleation density for all samples for each texture shows generally that the early stage crystals have a lower nucleation density with a higher characteristic crystal length. The late-stage crystals have a higher nucleation density and a lower characteristic crystal length (Fig. 56). There is no overlap between Texture 2 and all other Textures (1,3,4,5) for the early stage component. This suggests that Texture 2 has a clearly distinct early crystallization history from all other textures. There is also no overlap between Texture 2 and 4 for the late stage component. This suggests that Textures 2 and 4 have distinct late crystallization histories.

Additionally, equation 11 from the methods section, allows for estimation of residence time for each texture (Table 4). Using a maximum and minimum G values (empirical crystal growth rate) for hornblende of $3 \cdot 10^{-7}$ cm/s and $1 \cdot 10^{-8}$ cm/s, respectively, the maximum and minimum residence time values were calculated (Table 4). For the late stage component, the range of residence times between textures is approximately 0.2 - 0.3 years, and the early stage component is approximately 1 – 3 years.

Table 4. Resulting CSD data for Hornblende Crystals

Hornblende CSD												
Late Stage												
Bin Midpoint		0.127	0.201	0.319	0.506	0.801	1.270					
	# of Samples	ln (population density) values						Slope of trend line	Intercept	R^2	Residence time (yrs)	Residence time Avg. (yrs)
Texture 1	9	2.240	1.521	0.431	-0.752	-2.147	-3.793	-5.175	2.364	0.9633	0.020 - 0.613	0.32
Texture 2	2	3.275	1.935	0.28	-1.595	-3.28	-5.36	-7.529	3.020	0.9341	0.014 - 0.421	0.22
Texture 3	6	2.160	1.435	0.613	-0.540	-2.068	-3.787	-5.128	2.375	0.9752	0.021 - 0.618	0.32
Texture 4	4	0.092	0.468	1.065	-1.678	-3.468	-5.288	-6.164	2.080	0.9436	0.017 - 0.514	0.27
Texture 5	6	2.275	1.488	0.430	-0.885	-2.392	-4.240	-6.143	2.935	0.9399	0.017 - 0.516	0.27
Early Stage												
Bin Midpoint		2.01	3.19	5.06	8.01	12.70	-					
	# of Samples	ln (population density) values						Slope of trend line	Intercept	R^2	Residence time (yrs)	Residence time Avg. (yrs)
Texture 1	9	-5.689	-8.179	-10.394	-11.595	-13.380	-	-0.653	-5.804	0.8717	0.162 - 4.857	2.51
Texture 2	2	-10.295	-10.255	-7.160	-	-	-	-0.936	-6.034	0.6411	0.113 - 3.386	1.75
Texture 3	6	-5.897	-7.988	-11.185	-	-	-	-1.732	-2.434	0.9999	0.061 - 1.831	0.95
Texture 4	4	-7.840	-8.690	-11.430	-	-	-	-1.203	-5.205	0.9730	0.088 - 2.635	1.36
Texture 5	6	-6.562	-9.022	-10.860	-11.670	-13.220	-	-0.549	-6.865	0.8415	0.192 - 5.774	2.98

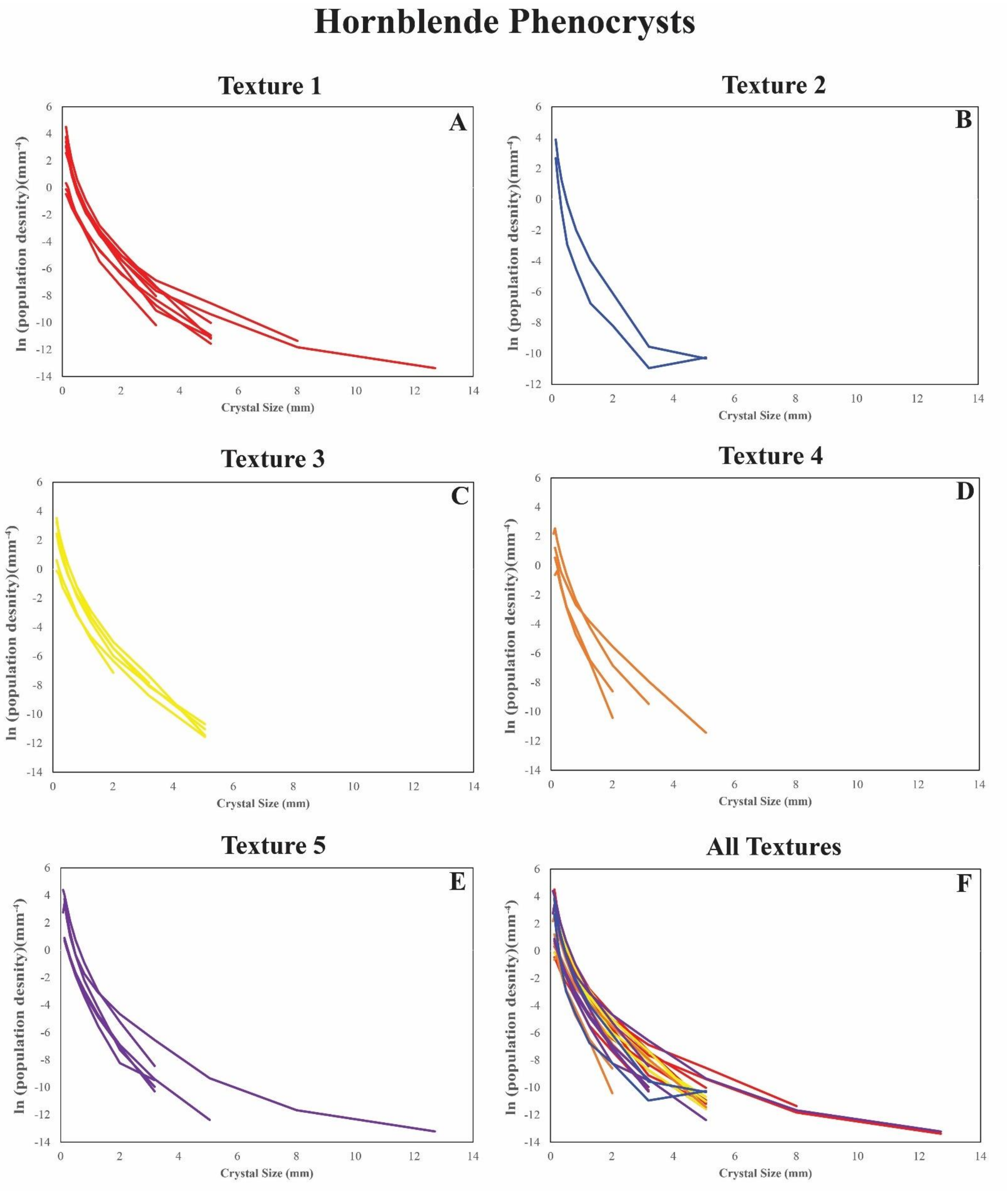

Figure 54. CSD plots for hornblende phenocrysts. **A.** Texture 1 (9 samples) **B.** Texture 2 (2 samples) **C.** Texture 3 (6 samples) **D.** Texture 4 (4 samples) **E.** Texture 5 (6 samples) **F.** All textures plotted together

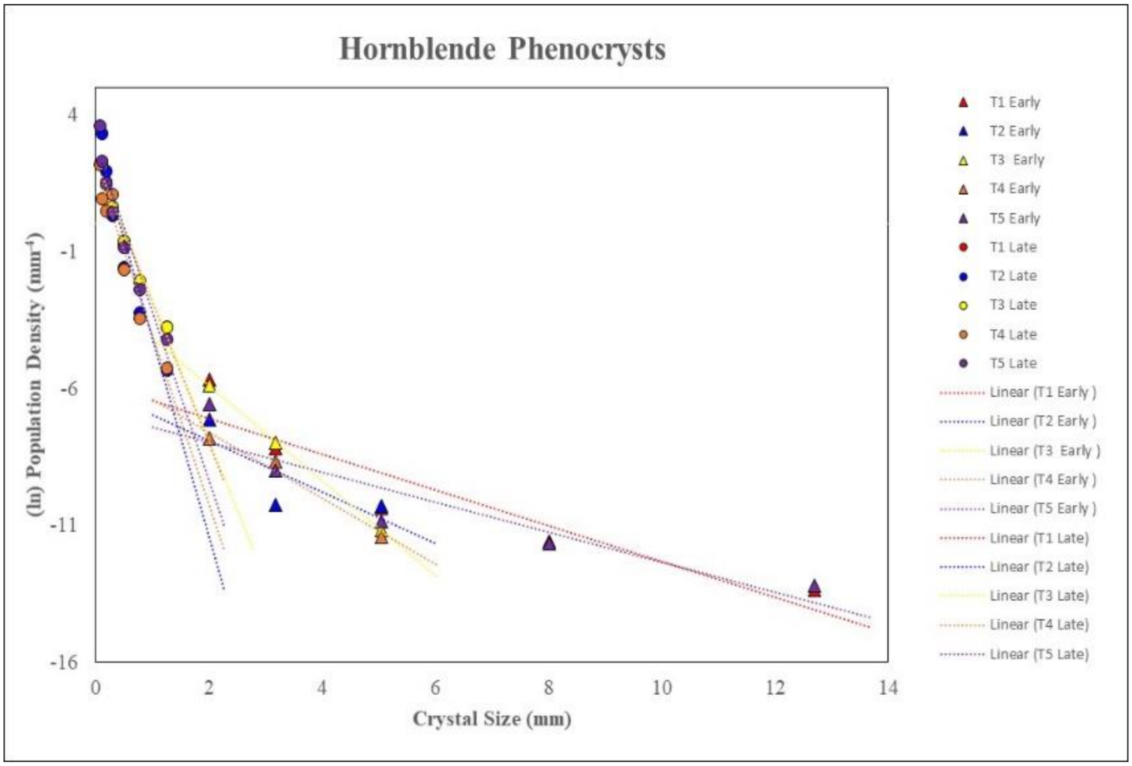

Figure 55. Linear regression analysis for averages of all textures for hornblende phenocrysts.

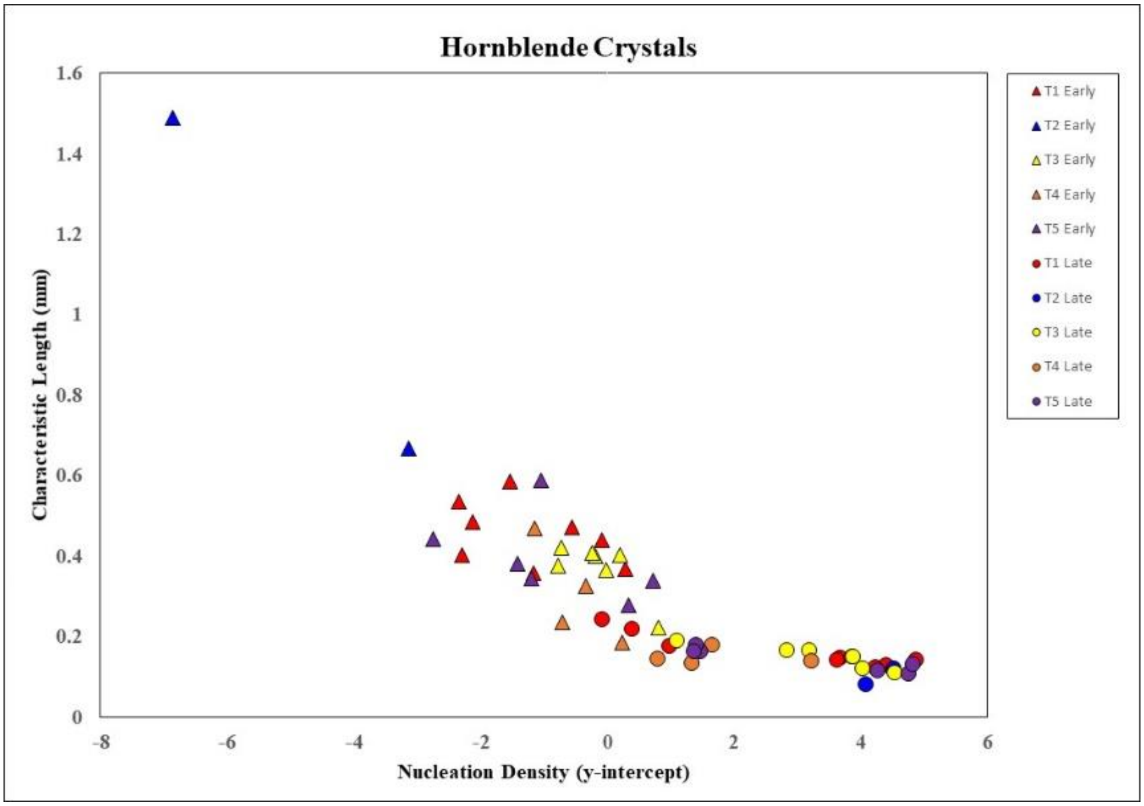

Figure 56. Characteristic crystal length versus nucleation density for all samples for each texture for hornblende phenocrysts.

7.5.2 Plagioclase Phenocrysts

Plots of CSD slopes for plagioclase phenocrysts are displayed by each texture group along with a combined plot including all textures (Fig. 57). Generally, plagioclase crystals are no larger than 8 mm, except for five samples from Texture 1, one sample from Texture 3, and 1 sample from Texture 4. The plagioclase CSD slopes are broadly consistent across textures, with a steep slope below the 1 mm in size and a more gradual slope above 1 mm in size. A linear regression was performed by using the averages for all plagioclase CSDs by texture (Fig. 58).

To further investigate and compare each textural group, averages for all CSDs, by texture, were plotted and analyzed using linear regression (Fig. 59). The resulting data (Table. 5) produced a trendline with a slope and y-intercept for the early stage and late stage component for each texture. The slope corresponds to the characteristic crystal length (equation 10), for each component, and the y-intercept corresponds to nucleation density (equation 9) of the magma.

Plotting the characteristic crystal length versus the nucleation density for all samples for each texture shows the early stage crystals generally have a lower nucleation density with a higher characteristic crystal length and the late stage crystals have a higher nucleation density and a lower characteristic crystal length. There is no overlap between Texture 1 and 5 and between Textures 2 and 5 for the early stage component. This would suggest that Textures 1 and 2 had clearly distinct early crystallization histories from Texture 5. There is also no overlap between Texture 2 and 5 for the late stage component. This would suggest that Textures 2 and 5 had clearly distinct late crystallization histories (Fig. 59).

Additionally, equation 11 from the methods section allows quantification of the residence time for each texture (Table 5) using maximum and minimum G values for plagioclase of $1.7 \cdot 10^{-6}$ cm/s and $7 \cdot 10^{-10}$ cm/s. The average between the maximum and minimum residence time values were calculated (Table 5). For the late-stage component, the range of residence times between textures is approximately 4 – 8 years, and the early-stage component is approximately 16 – 41 years.

7.5.3. Hornblende and Plagioclase Phenocrysts

A plot of the average nucleation density for each texture and each stage was used to examine both hornblende and plagioclase phenocrysts collectively (Fig. 60A). Individually, the hornblende phenocrysts (Fig. 60B) and plagioclase phenocryst (Fig. 60D) show a separation between nucleation density values at one standard devation between the early-stage and the late-stage components. Examining values for the early-stage component for both hornblende and plagioclase phenocrysts show that Textures 1, 3, and 4 are distinct from one another at one standard deviaiton (Fig. 60C). Values for the late-stage component for hornblende and plagioclase phenocrysts show that Texture 2 and 5 are distinct from one another at one standard deviation (Fig. 60E).

Table 5. Resulting CSD data for Plagioclase Crystals

Plagioclase CSD											
Late Stage											
Bin Midpoint		0.127	0.201	0.319	0.506	0.801	1.270				
	# of Samples	ln (population desnity) values						Slope (mm^{-1})	y-intercept	R^2	Residence time (yrs)	Residence time Avg. (yrs)
Texture 1	11	0.063	-0.170	-1.048	-2.144	-5.004	-4.996	-4.968	0.453	0.8806	0.004 -9.118	4.56
Texture 2	2	2.035	0.925	-0.270	-1.680	-3.190	-4.635	-5.629	1.889	0.9328	0.003 - 8.047	4.03
Texture 3	13	1.596	0.848	-0.173	-1.747	-3.625	-4.636	-5.553	1.694	0.9313	0.003 - 8.158	4.08
Texture 4	3	0.010	-0.673	-1.550	-2.293	-3.327	-4.317	-3.638	-0.070	0.9383	0.005 - 12.451	6.23
Texture 5	4	-0.530	-0.520	-1.035	-1.673	-2.545	-3.610	-2.825	-0.134	0.9893	0.007 - 16.037	8.02
Early Stage											
Bin Midpoint		2.01	3.19	5.06	8.01	12.70	-				
	# of Samples	ln (population desnity) values						Slope (mm^{-1})	y -intercept	R^2	Residence time (yrs)	Residence time Avg. (yrs)
Texture 1	11	-6.255	-7.776	-9.895	-12.331	-14.070	-	-0.724	-5.580	0.9402	0.026 - 62.560	31.29
Texture 2	2	-6.480	-8.515	-10.640	-	-	-	-1.343	-3.951	0.9863	0.014 - 33.725	16.87
Texture 3	13	-6.193	-8.186	-10.635	-12.653	-12.190	-	-0.541	-6.621	0.7157	0.034 - 83.749	41.89
Texture 4	3	-5.723	-7.397	-10.167	-12.080	-13.320	-	-0.693	-5.444	0.8798	0.027 - 65.358	32.69
Texture 5	4	-5.065	-7.140	-10.230	-12.337	-	-	-1.204	-3.194	0.9534	0.015 - 37.627	18.82

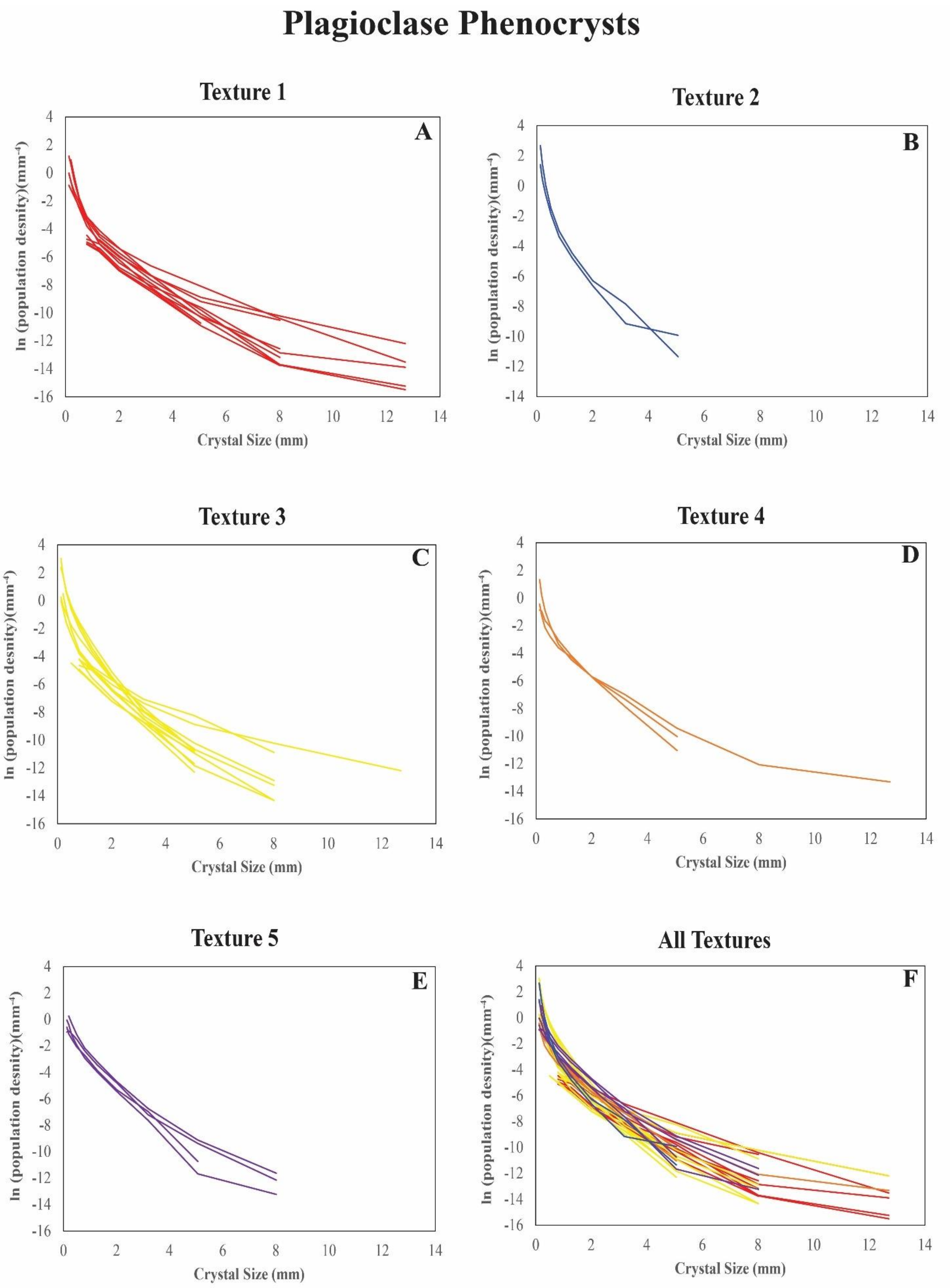

Figure 57. CSD plots for plagioclase phenocrysts. **A.** Texture 1 (11 samples) **B.** Texture 2 (2 samples) **C.** Texture 3 (13 samples) **D.** Texture 4 (3 samples) **E.** Texture 5 (4 samples) **F.** All textures plotted together.

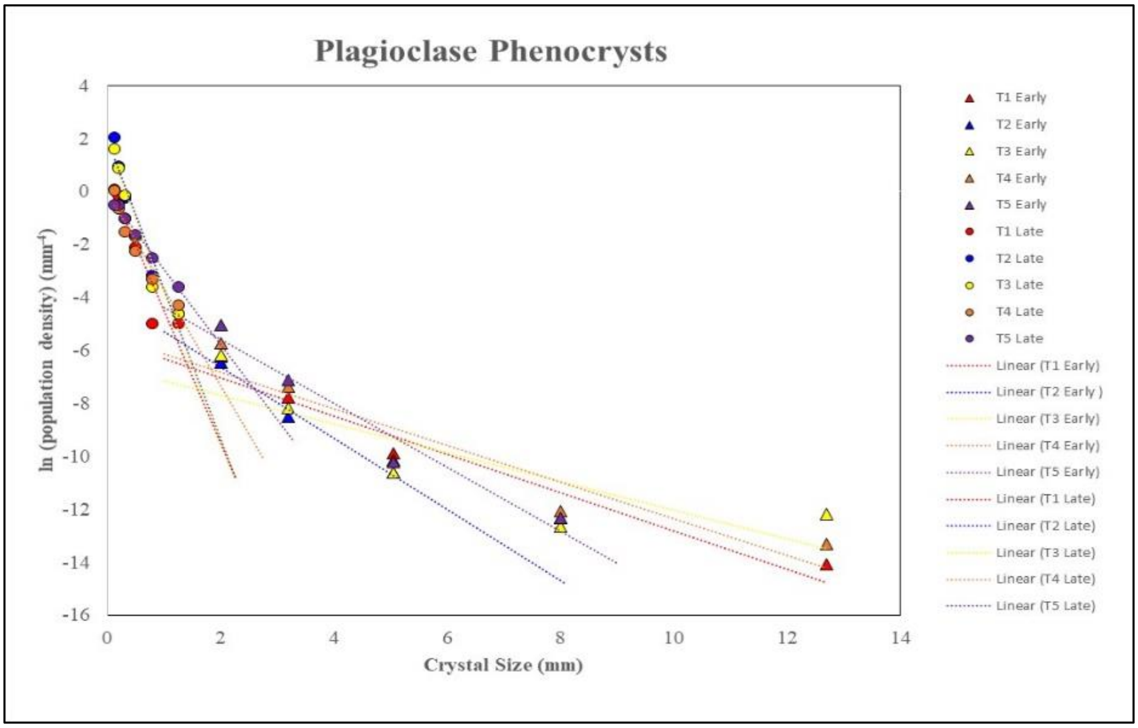

Figure 58. Linear regression analysis for averages of all textures for plagioclase phenocrysts.

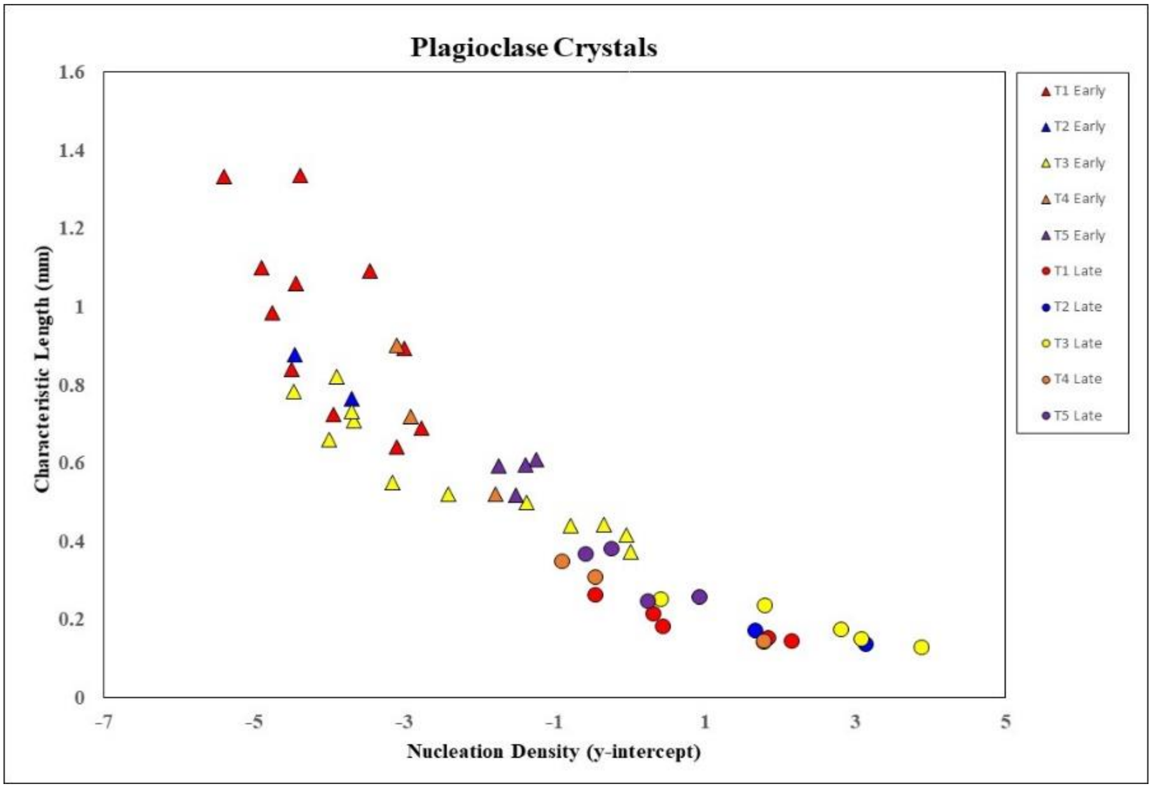

Figure 59. Characteristic crystal length versus nucleation density for all samples for each texture for plagioclase phenocrysts.

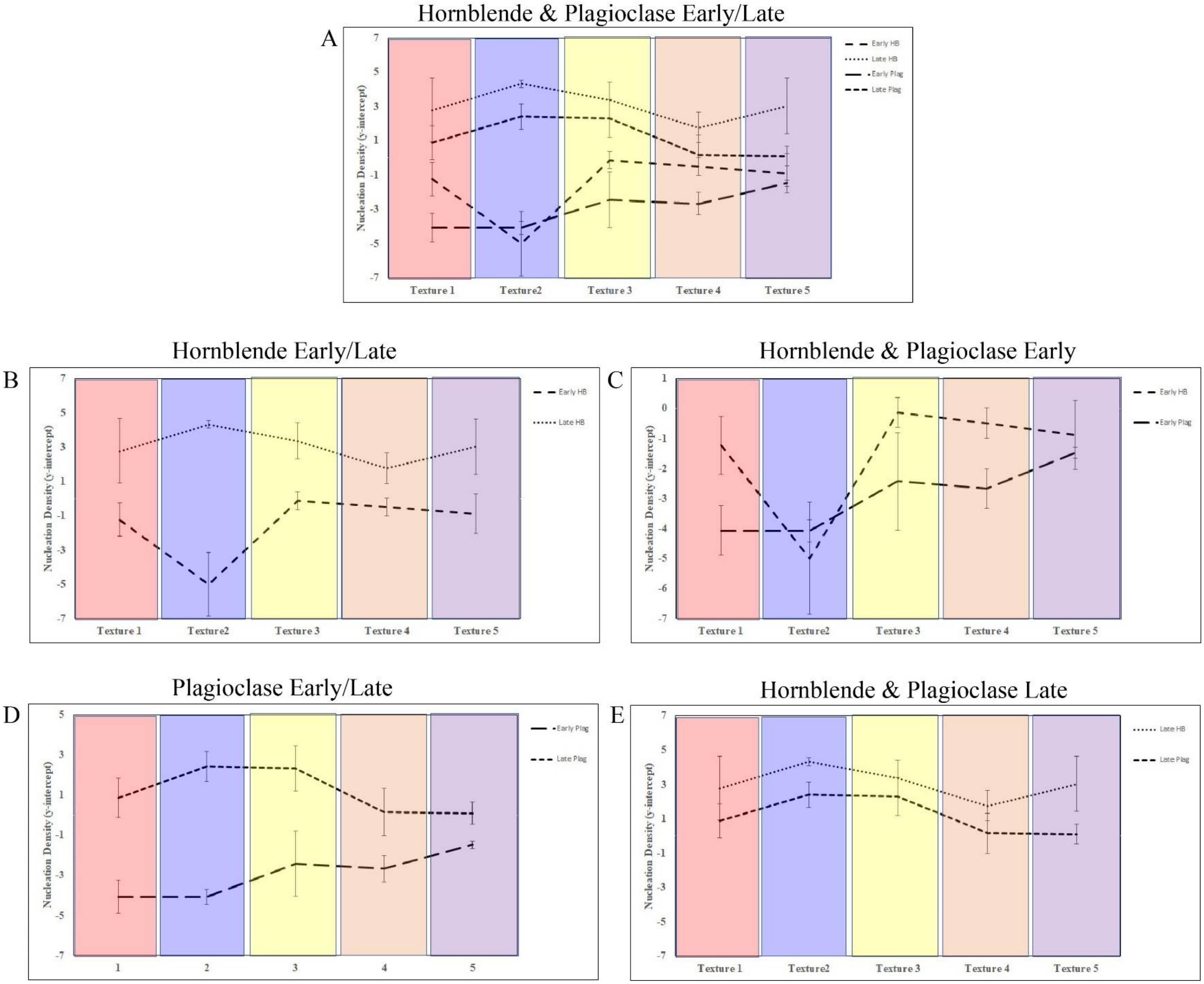

Figure 60. Averaged nucleation density values for all five texture groups with error bars at one standard deviation.

8.0 Discussion

In this section, I discuss and synthesize the data from each method in this study (fieldwork, lab analysis, geochemistry, AMS, and CSD). I then compare these results for the Mount Ellen intrusive complex with the previously mentioned case studies from the case studies section of this thesis. Additionally, I discuss my interpretations on how Mount Ellen was constructed based on the data and comparison to other case studies.

For this study, the texture of igneous rock samples was used as a basis to compare results from other methods by grouping all samples into 5 distinct textural groups. The use of texture alone is insufficient for distinguishing between magma batches or pulses because similar textures can have a considerable range of bulk compositions. However, this is one simple approach to provide a framework to compare results across a suite of data that includes multiple methods of analysis.

8.1 Field Work and Sample Collection

The structure contour map (Fig. 27) and the cross-sectional views (Fig. 26) of Mount Ellen clearly demonstrate to a first order a dome-like geometry with lobes radiating from the central portion of the intrusion. Mount Ellen's geometry reflects that of a Christmas-tree laccolith in cross-sectional view, with a suite of stacked intrusions between various sedimetary strata at different depths. Although not many contacts between igneous rock and sedimentary strata were observed, a few locations do show lobe-like geometries of igneous rock interacting with the sedimentary host rock (Fig. 37 B,C).

The five textural groups classified for this study are distinct from one another in phenocryst abundance (both plagioclase and hornblende), phenocryst size, and matrix color. The porphyritic texture indicates a two-stage cooling process. Larger phenocrysts formed within a magma chamber in the deeper crust before ascending to a level of final emplacement (early stage) and microphenocrysts formed during rapid cooling during the process of ascent and final emplacement (late stage). The variation of different textures within a single intrusive center stongly suggest that separate magma pulses contributed to the construction of Mount Ellen (e.g. Pownall et al, 2012). The magma within the mid-crustal chambers (> ~5km) can experience several processes such as magma mixing, fractional crystallization, and partial melting of host rock, that contribute to the diversity of magma compositions and overall texture of shallow crustal plutons (Higgins, 2002). More specifically, the nature of phenocrysts within mid-crustal chambers is important to address because phenocryst texture is not a record of emplacement, but rather the mid-crustal processes that formed the phenocrysts within a deeper magma chamber. The matrix in which these phenocrysts are embedded is a result of rapid cooling at near surface or surface conditions.

8.2 Geochemistry

Although there is not a discrete grouping of major element geochemical data between all five textures groups (Fig. 34), Textures 2 and 4 show a distinct grouping from one another in SiO_2 concentrations. This distinction also seems visibly apparent in the trace element data (Fig. 48B). To compare the statistical significance between Textures 2 and 4, a comparison between the mean and standard deviaiton values for trace element data were made using a T-test. The T-test compares the mean and standard deviation values between two sets of samples to see if there is a significant difference between them. The T-test resulted a probability value of 0.13, which suggest an 87% probablility that these two textures are distinct. Comparatively, Textures 1 and 3 appear to be visibly similar in trace element data. A T-test comparing Texture 1 and 3 resulted in a P-value of 0.95. This suggests a 5% probability that these two textures are distinct. Based on the visible differences in trace element data and the resulting T-test values, statistically Texture 2 and 4 are likely from separate pulses of magma.

The upper and lower sheet of the Copper Ridge laccolith on Mount Ellen also demonstrated in major and trace element geochemical data that they are from separate magma pulses (Maurer, 2015). For this study, the upper sheet of the Copper Ridge laccolith is grouped into Texture 1 and the lower sheet is grouped into Texture 3. Using the approach of examining data based on these texture groups, there is no geochemical distinction between Texture 1 and 3. The inclusion of other samples, outside the Copper Ridge laccolith, in these textures, masks the distinction noted by Maurer (2015).

The sample compositions for this study fall within the bulk compositional range observed by Nelson & Davidson (1993). This is not surprising, as Nelson & Davidson (1993) intentionally sampled the most extreme compositions of the Henry Mountains. Most of the samples range in composition of andesite to trachyandesite (Hunt et al., 1953; Hunt, 1988; Nelson & Davidson, 1993; Ward, 2014; Maurer, 2015; Thornton, 2015; Horsman et al., 2018) with SiO_2 concentrations ranging from 52 to 74 wt. %. Most samples plot from 60 and 63 wt. % SiO_2 (Nelson & Davidson, 1993). Patterns of trace element abundances for samples analyzed by Nelson & Davidson (1993) also demonstrate that the igneous rock for the Henry Mountains more closely resembles a calc-alkaline island arc basalt rather than intraplate basalts from the Basin and Range.

Texturally, most samples from the Henry Mountains can be classified as hornblende-plagioclase porphyry within a fine-grained matrix. In the case of this study, all samples are texturally hornblende-plagioclase porphyry. Nelson & Davidson (1993) suggest that the magma from this hornblende-plagioclase porphyry evolved through assimilation fractional crystallization in deep-crustal magma chambers. The fine-grained matrix demonstrates rapid cooling at the level of emplacement in the shallow crust.

The lack of an Eu anomaly (Fig. 48A) was also observed by Nelson & Davidson (1993) and Maurer (2015). Eu anomalies are predominantly controlled by the feldspars in felsic magmas (Rollinson, 2013). This may be explained by the lack of removal of plagioclase through fractional crystallization, which Nelson & Davidson suggest for the variation in geochemical data for the rocks of the Henry Mountains, or the addition of plagioclase through partial melting of the crystallizing magma. Nelson & Davidson (1993) suggest a low Eu^{2+}/Eu^{3+} ratio (McKay, 1989) resulting from oxidizing magmatic conditions. If there was an addition of plagioclase during the crystallization process, a positive spike in Eu would be expected and Eu depletion if there was removal of plagioclase.

8.3 Anisotropy of Magnetic Susceptibility

AMS has been used in many previous studies of the Henry Mountains and elsewhere to study the flow direction of magma within a single intrusions using magnetic fabrics (Horsman et al., 2005; Morgan et al., 2008; Maurer, 2015). Fabric is strongly controlled by details of local intrusion geometry. With a composite body like Mount Ellen, interpretations of fabric are not useful if component intrusions only have a couple of samples. A lower number of samples would not provide an accurate representation of magnetic fabric for Mount Ellen as a whole. Therefore only the scalar AMS results are useful for this study.

Mean susceptibility data are useful in determining variations between the different textural groups classified for this study. Although there is no variablility in mean susceptibility between all five texture groups (Fig. 50), Texture 2 and Texture 4 have distinctly separate mean susceptibility values. Texture 2 could have a higher bulk susceptibility value than Texture 4 due to compositional differences between each texture and the resulting magnetic mineralogy (e.g. abundance of magnetic minerals present). Texture 2 is more mafic in composition than Texture 4 and would generally be expected to have a higher magnetic susceptibility. However, the limited number of samples for both textural groups may not be sufficient to provide a reliable measure of possible susceptibilities difference between the textural groups. Additionally, Textures 2 and 4 show a separation in values for shape parameter (T) and folation (F) at one standard deviation (Fig. 51).

8.4 Crystal Size Distribution

The rates of crystal nucleation and growth are significant in determining the final texture of igneous rocks (Cashman, 2020). Using CSD to quantify the final textures of hornblende and plagioclase crystals for each textural group has revealed information on the crystallization history of each crystal type and for each textural group.

The CSDs for hornblende phenocrysts and plagioclase phenocrysts are characteristically distinct and can be described using the shape of their slopes and their nucleation density values (Fig 58 – 59). Both phenocrysts show a general trend for each texture with a “kinked” CSD curve between 1 and 2 mm. This could be a result of textural coarsening (small crystals dissolve at the same time as larger crystals grow), which causes a reduction in the CSD slope. Across all textures, both hornblende and plagioclase CSDs consistently show the early stage crystals having higher products of growth rate and residence time than the late stage crystals and early stage having lower nucleation values than the late stage crystals.

The slopes of the hornblende CSDs are generally steeper than the plagioclase CSDs overall. A more negative CSD slope is indicative of a faster cooling rate that produces smaller crystals and increases nucleation. Examining the slopes of CSDs across all textures shows no consistent correlation between hornblende and plagioclase CSDs. Comparing the slopes of CSDs from one texture to another shows that Texture 2 and Texture 4 show some separation in their slope shapes. The slopes for Texture 2 are generally steeper for both hornblende and plagioclase microphenocrysts (late stage) and generally shallower for phenocryst (early stage). This is consistent with Texture 2 demonstrating a higher nucleation density for microphenocrysts and a lower nucleation density for phenocrysts. This suggests that these two textures have separate crystallization histories from one another. It is also notable that Texture 5 shows a distinction for plagioclase microphenocrysts from both Texture 1 and Texture 2.

Residence times were calculated for both hornblende and plagioclase crystals (Table 4). Resulting residence times are calculated based on experimental data of crystal growth rates for plagioclase and hornblende crystals and should be viewed as an approximation. The hornblende microphenocrysts and phenocrysts residence times range from 0.2 (~73 day) - 3 years. The plagioclase microphenocrysts and phenocrysts residence times range from 4 – 41 years. The modeled residence times for each crystal type is less than 1000 years as suggested by Cashman (1993). These ranges and approximations of growth rates suggest that hornblende crystals formed in a shorter time span than plagioclase crystals. This is consistent with plagioclase crystals being generally larger than hornblende crystals within the samples analyzed. Shorter residence times for the samples of this study are considered indicative of a shallow level (mid-crustal) magmatic system (Cashman, 1993). There is a clear record of changes in crystallization history in the mid-crust and residence times suggest magma ascent through dikes to final emplacement took a few weeks at most.

The construction of Mount Ellen is highly complex and at the scale of an entire intrusive center, distinctions between pulses are somewhat cryptic. The CSD data for all five textural groups provides constraints on how long magma bodies spent in the mid-crustal storage system. Texture 2 has the smallest crystals present and Texture 1 has the largest crystals present. The textural groups clearly have different crystallization histories. Based on the sizes of crystals present and the residence times of phenocrysts, the following order is representative of the texture that spent the least amount of time to the greatest amount of time in the mid-crustal magma storage system where the phenocrysts grew: Texture 2, Texture 5, Texture 3, Texture 4, and then Texture 1.

8.5 Comparison to Case Studies

The data for this study provides a suitable framework to further evaluate the Mount Ellen intrusive complex and how it was constructed over time. Further detailed work on individual component intrusions and a compilation of their data would be most beneficial for a more complete history. However, various other studies of intrusions can help provide comparable insight on the construction of Mount Ellen. The case studies previously mentioned in this study were chosen for this reason and will be used to evaluate interpretations of Mount Ellen's history.

As a short recap, Mount Ellen is the largest of the intrusive centers of the Henry Mountains. Mount Ellen is composed of dozens of component intrusions that contribute to its dome-like geometry and has an igneous rock volume of approximately 100 km^3. Mount Ellen also extends approximately 15 – 20 km from NW to SE. Recent zircon U/Pb dating performed by Murray et al. (2016) determined an Oligocene age of 27.8 ± 0.58 Ma and suggests Mount Ellen was constructed over a million-year time scale.

8.5.1 Characteristics

8.5.1.1 Depth of Emplacement, Radial Extent, and Total Rock Volume

The Mount Ellen intrusive complex was emplaced into the shallow crust at a depth of approximately 2 – 4 km, has a diameter of ~ 15 – 20 km, and has a total igneous rock volume of 100 km^3. These characteristics are comparable to several of the case studies previously discussed. The Torres del Paine laccolith has an emplacement depth of 2 – 3 km and has a total igneous rock volume of ~88 km^3. The Elba Island laccolith was emplaced at 2 – 3 km depth, has a diameter of approximately 10 km, and has a total igneous rock volume of ~37 km^3. The Erland volcano plumbing system is ~ 15 km in diameter and has a total rock volume of ~ 200 km^3. These first order similarities suggest that these other intrusions can provide insight on how Mount Ellen was constructed based on their characteristics.

8.5.1.2 Geometry

The Torres del Paine laccolith is constructed from distinct sheets stacked upon one another to collectively form a laccolithic body and its overall geometry. These sheets are geochemically different from one another and are discernably separate in field observations (Michel et al. 2008; Leuthold et al. 2012). The difference in geochemical data for each sheet and the amalgamation of these sheets to form a single laccolith. The Elba Island laccolith and the Erland Volcano plumbing system are both exceptional examples of laccoliths with a Christmas-tree like geometry composed of a network of stacked intrusions/sheets (Rocchi, 2010; Walker et al. 2020). Geochemical data from this study and for smaller component intrusions of Mount Ellen (Maurer, 2015), show a geochemical distinction between textures and individual stacked sheets. This may be indicative that Mount Ellen also has a Christmas-tree like geometry with an interconnected network of stacked sheets.

As discussed, Mount Ellen has a circular like geometry in map-view with lobes radiating from the central part of the intrusions. We see similar geometries and radiating lobes in the Erland volcano plumbing system, the North Rockall Trough, and even in analogue models (Thomas & Hutton, 2004; Currier & Marsh, 2015; Walker et al. 2020). This suggests that a circular map-view geometry may be a consequence of small lobate and elongated component intrusions.

8.5.1.3 Growth

A wide variety of sources and data suggest that many igneous intrusions in the shallow crust are built incrementally over time, but there is no one general growth pattern for these intrusions. A magma pulse is injected into the shallow crust forming a single small intrusion. Several more injections may contribute to the growth of this small intrusion and coalesce into a single sheet. There may or may not be a period of cooling, however if there is a period of cooling, the first intrusive body, as a partially solidified mush, may act as a barrier for additional injections of magma. The barrier would form a separation between the next injection from the previous injections, and potentially create an under-accreted second small intrusion. This intrusion may follow the same growth path as the first with additional injections and coalescence of these additional injections. This would ultimately form two separate sheets that are stacked upon one another. A continuation of multiple sheets stacking upon one another will increase the length and thickness of these intrusions and ultimately form laccoliths or other sheeted plutons. It is important to keep in mind that this is only one scenario of how these intrusions may form. A sheet could also form from a single magma injection. The volume of magma supplied during a single pulse may be variable in both volume and timescale. This type of growth pattern is what we can see in several of the case studies and for the Mount Ellen intrusive complex.

The North Rockall Trough is an example of an intrusive complex that provides insight on magma flow patterns, sill growth, and sill geometry (Thomson & Hutton, 2004). It demonstrates how intrusions may form from lobes that coalesce into sheets and how these lobes and sheets radiate from the central portion of these sills. Additionally, analogue models support how modelled laccoliths are a product of multiple lobes that coalesce to form sheets, produce a dome-like appearance, and have circular geometries in map-view. This may be indicative of the how Mount Ellen was constructed because its geometry indicates a central body with stacked intrusions with dozens of radiating intrusions from the central body.

As discussed earlier, correlations exist between scaling dimensions for various igneous intrusions, the duration of a its construction and its overall final volume and geometry. To quantify the overall geometry of Mount Ellen, approximations of length (~20,000 m), thickness (~2,000 m), and volume (100,000,000,000 m^3) characteristics were used, and we are able to see that Mount Ellen plots along with many laccolithic igneous intrusions based on these parameters (Fig. 59, 60). This suggests Mount Ellen followed a similar growth path as the compilation of laccoliths modeled by Cruden et al. (2017).

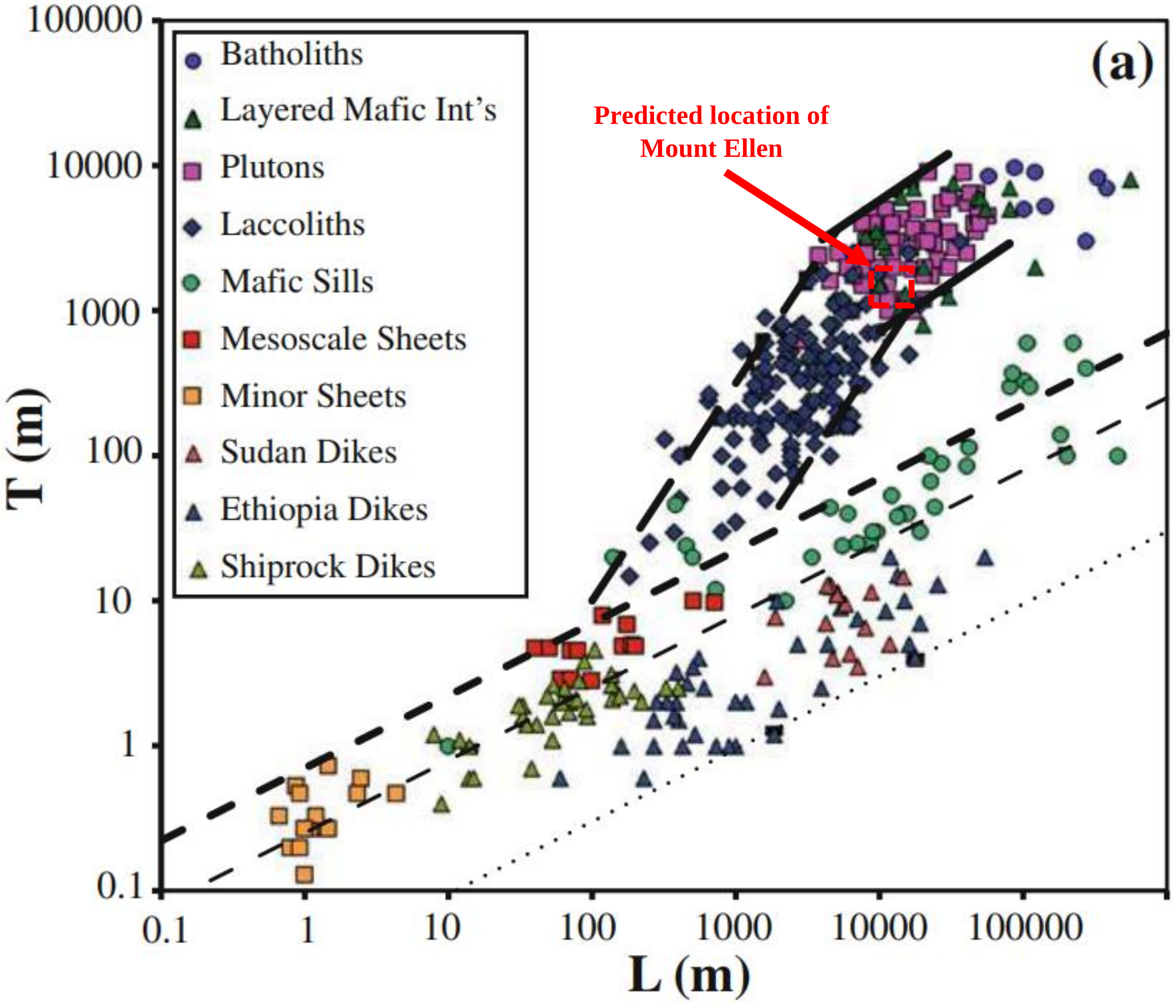

Figure 61. Log thickness (T) versus Log length (L) of dimensional data for dikes, sills, and laccoliths from various sources. The approximation where Mount Ellen would fall on this plot is noted by the dashed red box (modified from Cruden et al., 2017).

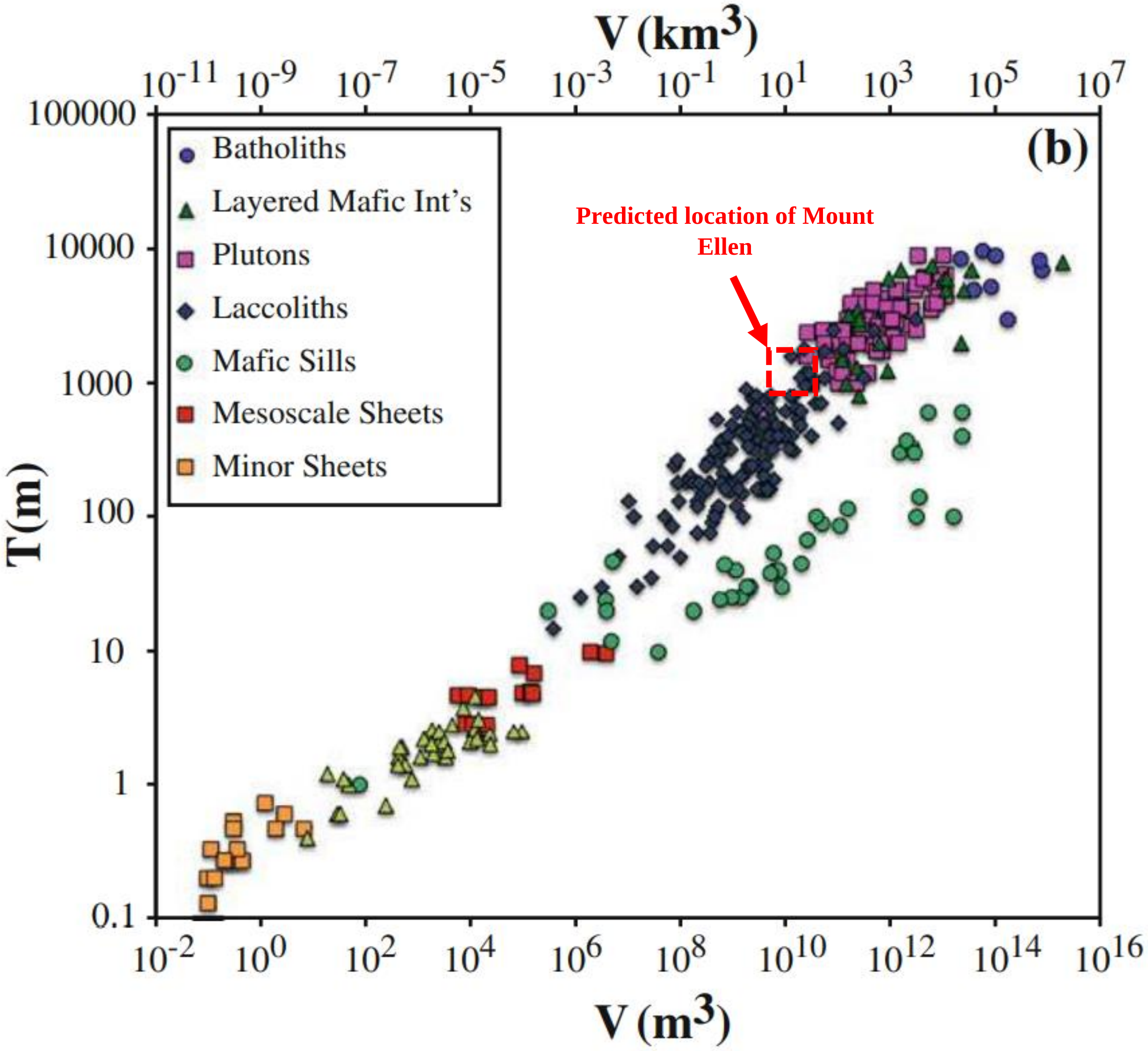

Figure 62. Log thickness (T) versus Log volume (V) of dimensional data for dikes, sills, and laccoliths from various sources. The approximation where Mount Ellen would fall on this plot is noted by the dashed red box (modified from Cruden et al., 2017).

8.5.1.4 Timescale

The Torres del Paine laccolith was constructed over a time span of 90,000 years. It has a total rock volume of ~88 km^3 with an average construction rate of 0.0005 $km^3\ y^{-1}$. Similarly, Mount Ellen was constructed over a time span of approximately 1 million years, with a total rock volume of ~ 100 km^3 and an average construction rate of 0.0004 $km^3\ y^{-1}$. These growth rates are on the low end compared to growth rates of other plutons worldwide, which have growth rates that vary over three orders of magnitude from 0.0001 to 0.1 $km^3\ y^{-1}$ (Saint Blanquat et al., 2011). Recent work from Saint Blanquat et al. (2011) suggest that the duration of pluton construction correlates, on a first order, to the pluton volume. The magma flux rates and total rock volume for the Torres del Paine laccolith and the Mount Ellen intrusive center correspond with the timescale for which they were constructed. These relatively small intrusive centers were constructed over relatively short periods of geological time.

Using zircon U/Pb ages from Murray (2016) for the Henry Mountains of 25.5 ± 0.37 Ma (Mount Hillers and Mount Pennell) and 27.8 ± 0.58 Ma (Mount Ellen) and an estimated igneous rock volume of 100 km^3 (Horsman et al., 2018) for Mount Ellen, yielded an estimated magma flux rate of 0.0004 $km^3\ y^{-1}$. This is comparable to the growth rate of the Torres del Paine laccolith and the Elba Island laccolith. When compared to growth rates of other various size plutons, Mount Ellen falls within the growth rates modeled by Saint Blanquat et al. (2011) (Fig. 63).

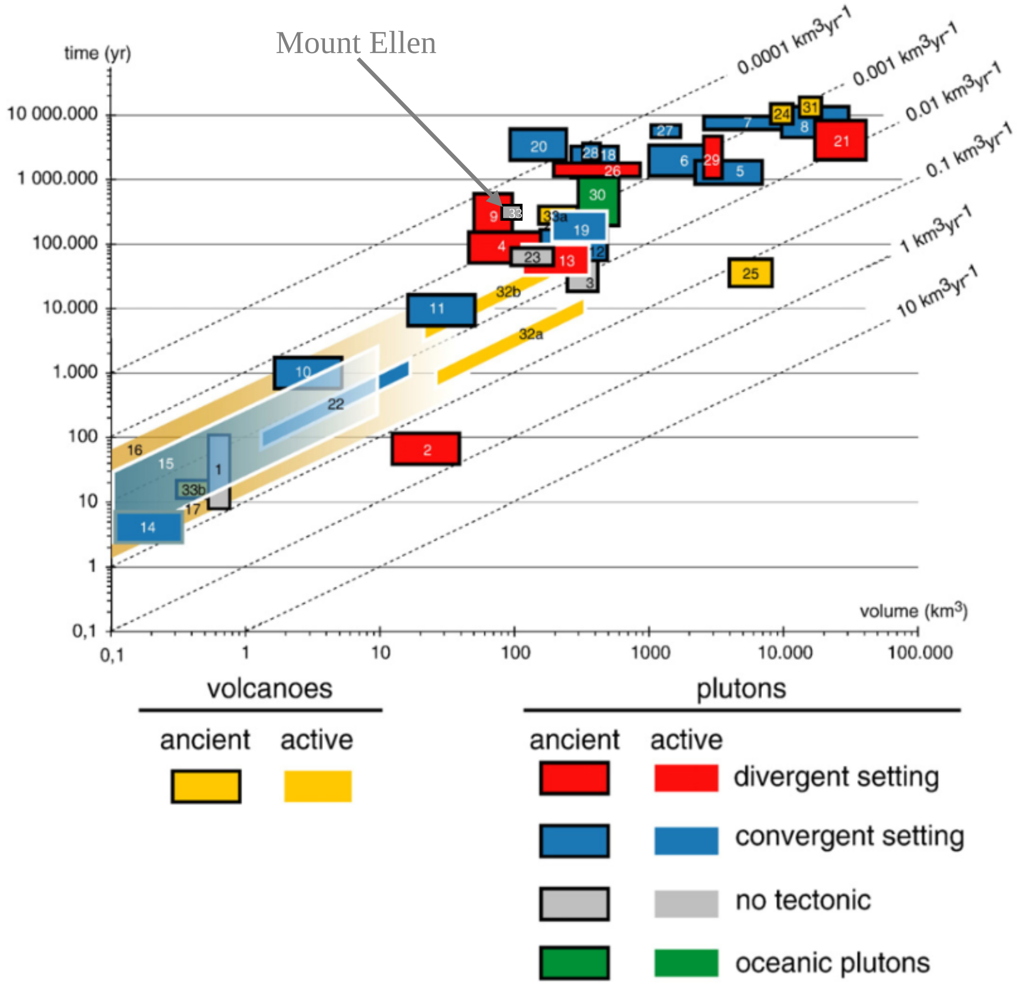

Figure 63. Compilation of duration and rates of pluton construction for various pluton sizes for both active and ancient systems. 2 – Elba Island Laccolith (Rocchi et al, 2002); 23 – Torres del Paine Laccolith (Michel et al., 2008); 33 – Mount Ellen Intrusive Complex (Modified from Saint Blanquat et al. 2011).

8.6 History of a Generalized Henry Mountains Magma Body

Nelson & Davidson (1993) suggest the Henry Mountains magma is produced from "ponding" of basaltic melt at the base of the crust, which then melts the Proterozoic lower crust. The product of this process ascends the magma to mid-crustal levels (> ~ 5 km) developing a magma chamber. The crystallization of phenocrysts begins within the magma chamber for hornblende phenocrysts (0.2 to 3 years) and plagioclase phenocrysts (4 to 41 years). Magma ascends rapidly through a dike or network of dikes to the shallow crust (< ~ 5 km) in a matter of several days to weeks at most. Once magma is emplaced into the shallow crust, rapid cooling occurs to form a fine-grained matrix.

8.7 Proposed Construction History and Geometry of the Mount Ellen Intrusive Complex

This research has demonstrated that Mount Ellen is constructed from multiple magma pulses. Of the five textural groups classified for this study, Textures 2 and 4 show a distinction from one another across all data sets. Research preformed by Maurer (2015) demonstrated that Mount Ellen's largest component intrusion was built from two stacked sheets that were constructed from at least two magma pulses. Many of the case studies presented earlier in this paper demonstrate clear evidence of laccoliths forming from multiple magma pulses and are constructed from stacked sheets.

Based on data from this study, correlations between pluton characteristics (length, thickness, volume, and duration), and examples from other studies on similar intrusions, Mount Ellen followed a growth path that produced a Christmas-tree like geometry. Mount Ellen is a complex network constructed from various component intrusions that under accreted (and some over accreted) one another. A proposed schematic diagram shows a simplistic stepwise construction of Mount Ellen before reaching its final stage of emplacement (Fig. 64). It is important to note that the schematic diagram does not account for the number of magma pulses that contributed to the construction of Mount Ellen, but rather demonstrates how Mount Ellen's final geometry reflects a growth model similar to the Elba Island laccolith and the Erland Volcano plumbing system. Mount Ellen is constructed from an interconnected network of amalgamated intrusions with dozens of radiating lobes from the central portion of the intrusive center. We can also infer from its Christmas-tree like geometry, that pulses were injected sequentially with periods of time between injections, i.e. a pulse was emplaced and had time to cool/solidify to some extent, before a sequential pulse was emplaced.

Taking into consideration how Mount Ellen was constructed from dozens of component intrusions and how these intrusions themselves can be constructed from multiple stacked sheets, I suggest that Mount Ellen was constructed from a minimum of 5 texturally distinct magma pulses (at the coarsest scale) that were widely distributed to several parts of Mount Ellen. Each textural group was emplaced as a separate pulsed event, regardless of the order they were emplaced. However, based on relative elevation of the mapped-out textures in cross-sectional view and residence times calculated for each texture, a general order of emplacement can be made.

Using the spatial distribution map of all five textural groups and their relative crustal elevations (Fig. 65), I was able to constrain to a first order, the order of emplacement for Textures 1, 3, and 5. Textures 2 and 4 are not included due their lack of distribution compared to other texture groups. Texture 4 was emplaced first, followed by texture 1, and then texture 3. The map-view geometry was also constrained to a first order for these three texture groups as demonstrated in Figure 66. Each of these textures are mapped out as individual sheets that are stacked upon one another. Although I suggest a minimum of 5 separate pulses, there may be additional pulses that contribute to the construction of Mount Ellen, as contacts may be cryptic. However, it can be seen for one of the larger component intrusions (Copper Ridge Laccolith) of Mount Ellen, that multiple pulsed construction does exists through the stacking of sheeted intrusions.

Stage 1

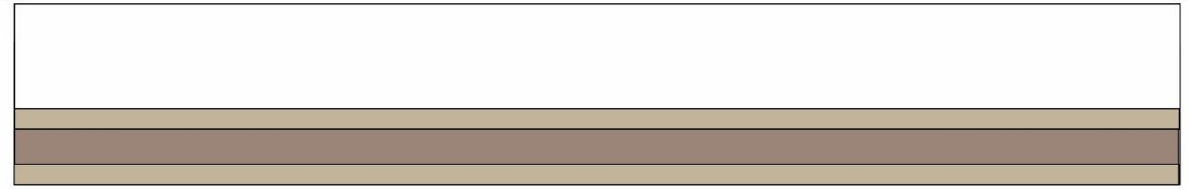

Horizontal sedimentary strata prior to intrusion emplacement and deformation.

Stage 2

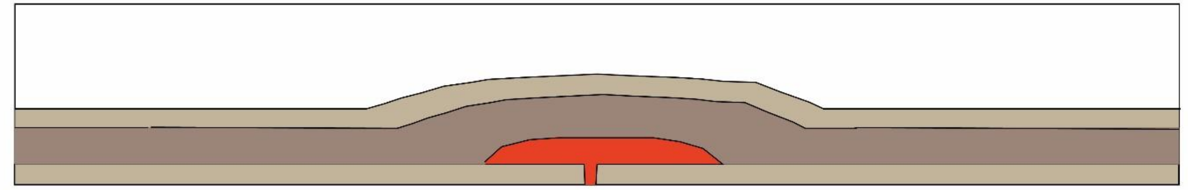

Intrusion is emplaced from a central feeder as a sill or small laccolith. Initial doming of surrounding host rock begins to occur. One or more injections of magma may be responsible for intrusions emplacement.

Stage 3

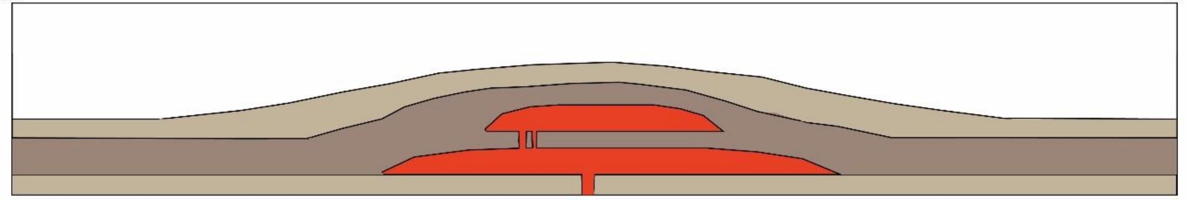

Initial intrusion reaches a critical spreading length and sill begins to thicken into a laccolith. Cooling occurred for previous batch(es) of magma. Additions of magma injections intrude below existing laccolith to accommodate space for new magma. The above laccolith may have acted as a barrier that was still in a mushy state.

Figure 64. Cross sectional diagram of simplified construction model of Mount Ellen (not to scale for first five diagrams).

Stage 4

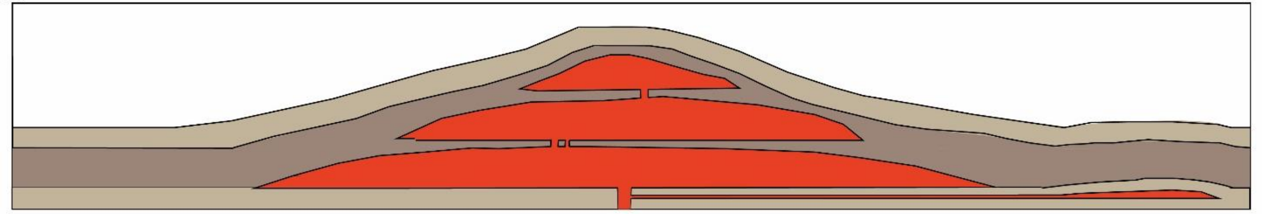

The additional batch (es) of magma are also halted by overlying mush. Rapid injections cause the magma to spread more laterally and emplace a radiating sill from the central intrusive body.

Stage 5

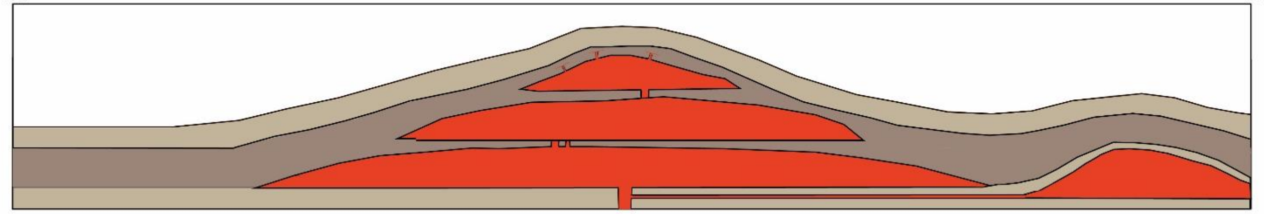

Radiating sill reached a critical length value and thickens into a laccolith.

Final Stage

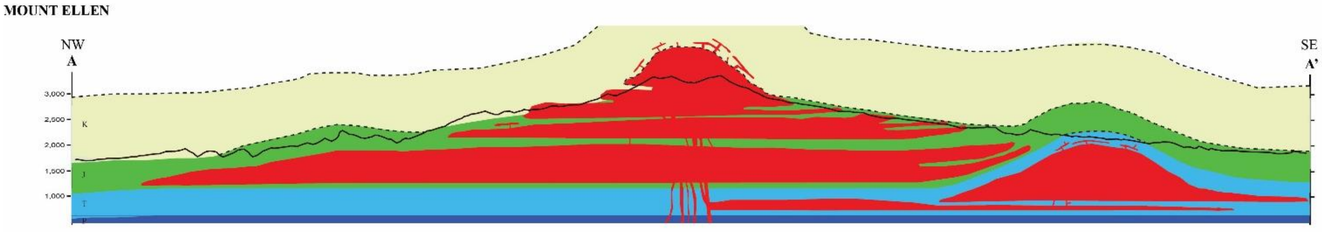

Final product of a Christmas-tree like geometry with a multicomponent network of stacked sheets/intrusions.

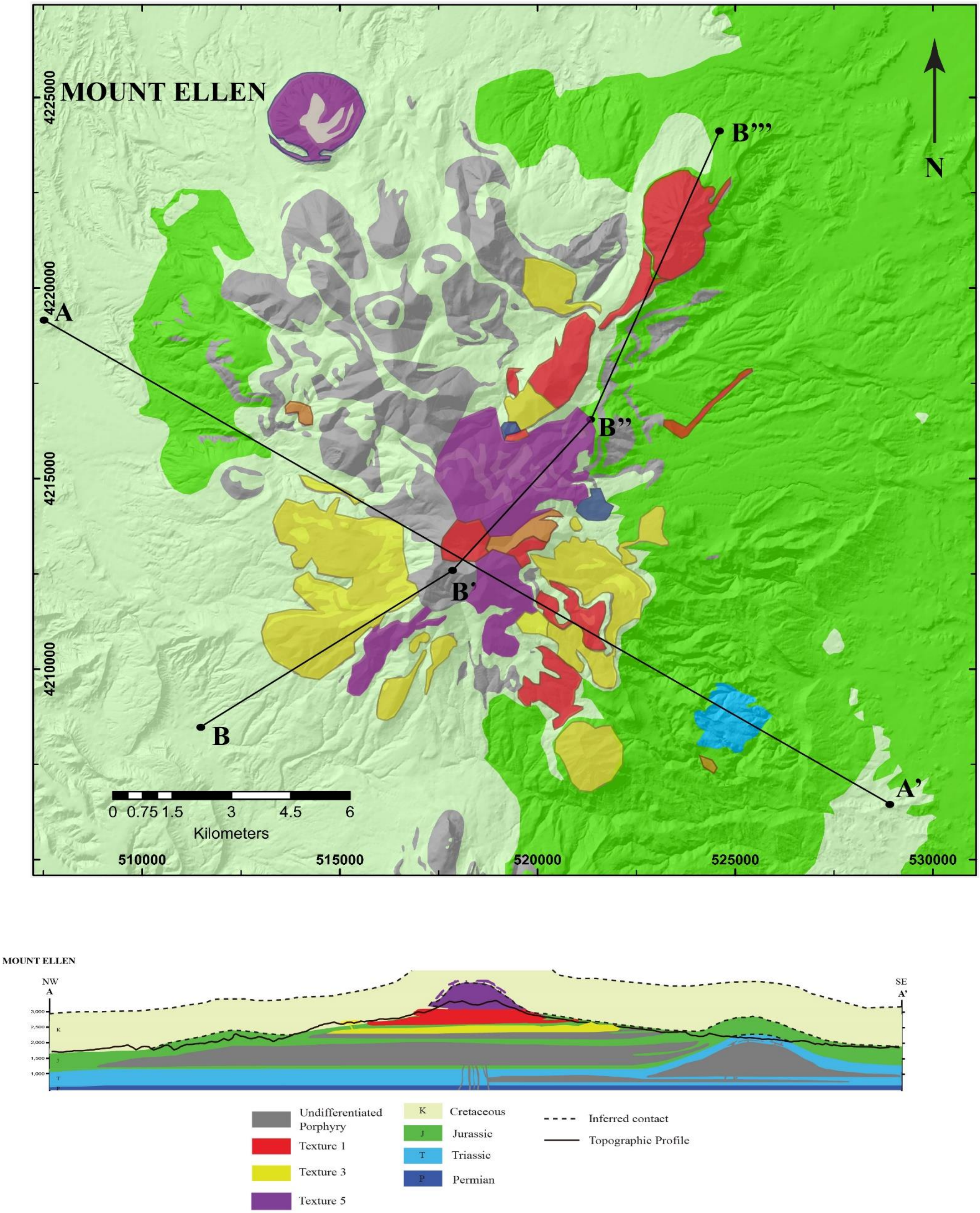

Figure 65. Map view of distribution for all five textures with associated cross-section demonstrating the order of emplacement for Texture 1, Texture 3, and Texture 5.

Distribution of Texture 5

Distribution of Texture 1

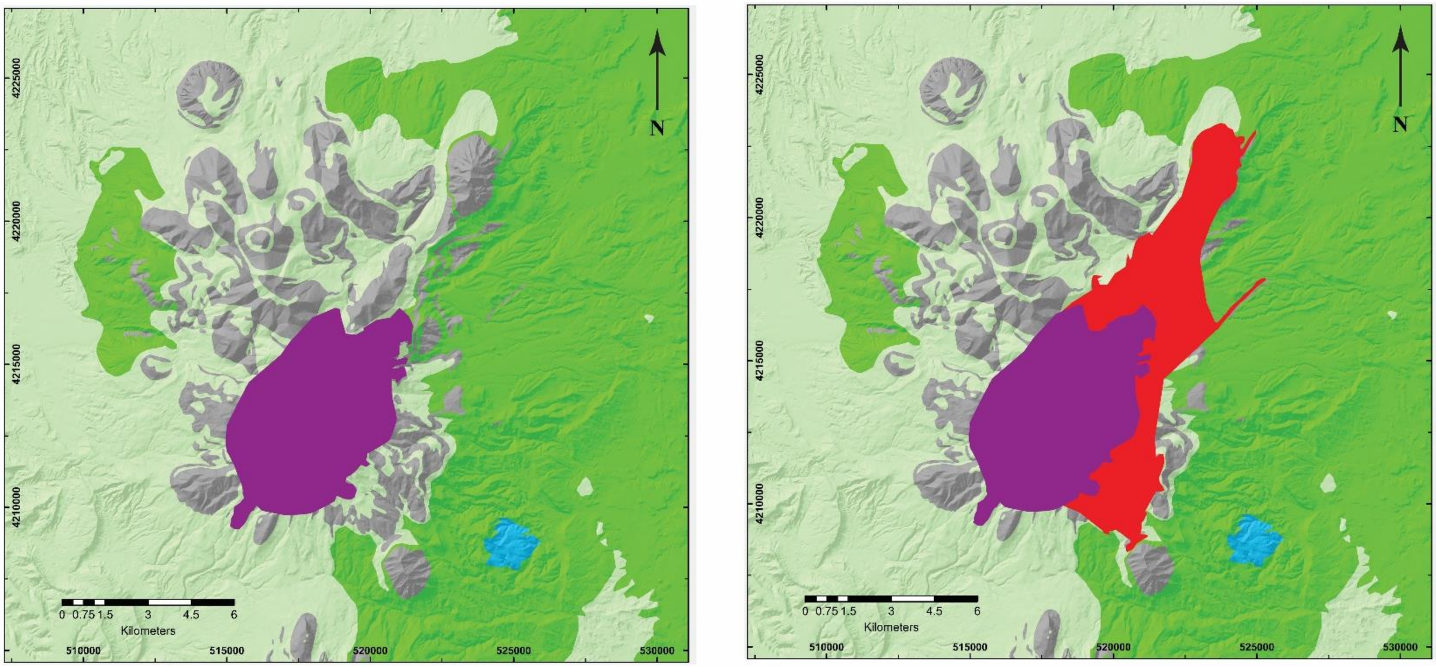

Distribution of Texture 3

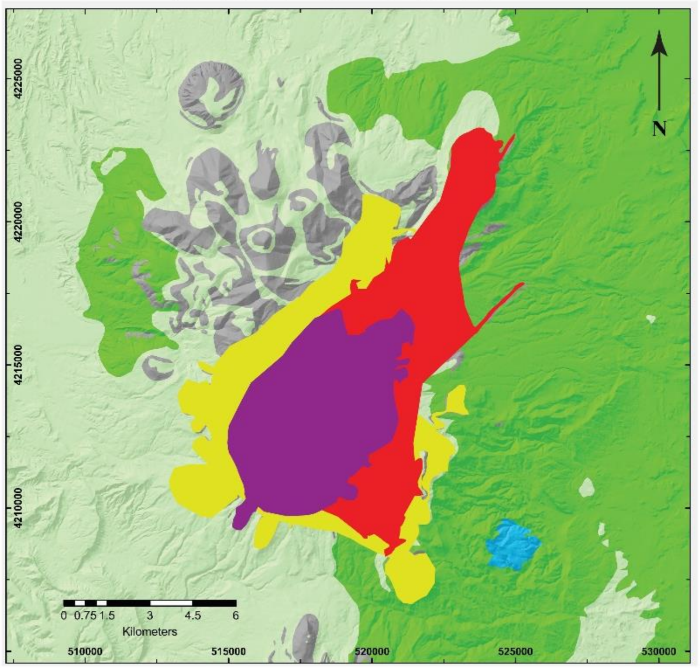

Figure 66. Map view distribution of proposed sheets in order of emplacement for Texture 1, Texture 3, and Texture 5.

9. Conclusions

Magma systems within the shallow crust drive volcanic activity at the surface. These magma systems are difficult to study directly, but ancient systems can be used as an analogue to study modern systems. The Henry Mountains of Utah are a collection of five, well-exposed shallow crustal intrusions with a lack of tectonic deformation. They are an exceptional example for studying ancient systems and the processes that contributed to their construction.

The purpose of this study was to constrain the construction history of Mount Ellen by synthesizing multiple suites of data and to test if Mount Ellen was constructed from multiple magma pulses. Previous studies have examined smaller component intrusions of Mount Ellen with similar methods but did not examine Mount Ellen as a whole.

Although we are unable to constrain a concrete number of magma pulses that contributed to the construction of Mount Ellen, various data sets and calculations demonstrate that the Mount Ellen intrusive complex is constructed from a minimum of 5 separate pulses of magma at the coarsest scale. Two of the five textural groups classified for this study and additional work by Maurer (2015) support these findings through differences in geochemical, AMS, and CSD data.

Using parameters to quantify the overall geometry and construction of Mount Ellen such as length, thickness, volume, and duration of emplacement demonstrate that Mount Ellen comparatively fits into models for predicted laccolith growth. The Christmas-tree like geometry of Mount Ellen is likely from a network of sills and laccoliths that failed to coalesce during emplacement. Zircon U/Pb ages show that Mount Ellen was constructed over a time span of approximately 1 million years at an average rate of 0.0004 km^3 y^{-1}.

9.1 Future Work

Future research should aim to further analyze crystal size distribution samples from this thesis. The five textural groups for this thesis were objectively classified based on the appearance of crystals within a rock slab sample. Examining samples in thin sections would provide a more rigorous job at differentiating between textures. Thin sections would also provide constraints on emplacement histories for all samples by analyzing the groundmass.

Detailed studies on individual component intrusions of Mount Ellen would provide greater insight on Mount Ellen’s construction history. I suggest employing the same methods of analysis from this thesis on individual component intrusions and to collect enough samples to analyze a single component intrusion in detail. These individual intrusions could then collectively provide significant insight and detail for a more complete construction history.

10. References Cited

Annen, C., Sparks, R.S.J., 2002. Effects of repetitive emplacement of basaltic intrusionson the thermal evolution and melt generation in the crust. Earth Planet. Sci. Lett.203, 937–955.

Annen, C., Scaillet, B., Sparks, R.S.J., 2006. Thermal constraints on the emplacement rateof a large intrusive complex: the Manaslu leucogranite, Nepal, Himalaya. J. Petrol.47, 71–95.

Annen, C., Pichavant, M., Bachmann, O., Burgisser, A., 2008. Conditions for the growth of a long-lived shallow crustal magma chamber below Mount Pelee volcano (Martinique, Lesser Antilles Arc). J. Geophys. Res. 113 Art. No. B07209, July 26.

Baer, G., and Reches, Z., 1991, Mechanics of emplacement and tectonic implications of the Ramon dike systems, Israel: Journal of Geophysical Research, v. 96, p. 11,895–11,910, doi: 10.1029/91JB00371.

Bartley, J.M., Coleman, D.S., Glazner, A.F., 2008. Incremental pluton emplacement by magmatic crack-seal. Transactions Royal Society of Edinburgh: Earth Sciences 97, 383–396

Bas, M.J.L., Maitre, R.W.L., Streckeisen, A., and Zanettin, B., 1986, A chemical classification of volcanic rocks based on the total alkali-silica diagram: Journal of Petrology, v. 27, no. 3, p. 745-750.

Bonechi, B., Perinelli, C. & Gaeta, M. Clinopyroxene growth rates at high pressure: constraints on magma recharge of the deep reservoir of the Campi Flegrei Volcanic District (south Italy). *Bull Volcanology* 82, 5 (2020). https://doi.org/10.1007/s00445-019-1342-5

Bouchez, J.L., 1997, Granite is never isotropic: an introduction to AMS studies of granitic rocks, in Bouchez, J.L., Hutton, D.H.W., and Stephens, W.E., eds., Granite: From Segregation of Melt to Emplacement Fabrics: Springer, Netherlands, p. 95-112.

Braunagel, M., Giorgis, S., Horsman, E., 2015. Using preserved secular variation to constrain emplacement duration in large scale sills, Copper Ridge intrusion, Mt. Ellen, Henry Mountains, Utah: Geological Society of America Abstracts with Programs. Vol. 47, No. 7, p.579

Broda, R.J., 2014. Geometry and progressive development of a shallow crustal intrusive 716 complex, Mount Hillers, Henry Mountains, Utah. M.S. thesis, East Carolina Univ., 100 pp.

Bump, A.P., 2004, Three-dimensional Laramide deformation of the Colorado Plateau: Competing stresses from the Sevier thrust belt and the flat Farallon slab: Tectonics, v. 23, no. 1, p. TC1008.

Daniels, K.A., Kavanagh, J.L., Menand, T., and R. Stephen, J.S., 2012, The shapes of dikes: Evidence for the influence of cooling and inelastic deformation: Geological Society of America Bulletin, v. 124, p. 1102-1112, doi: 10.1130/B30537.1.

Davis, G.H., and Bump, A.P., 2009. Structural geologic evolution of the Colorado Plateau. In: Kay, S.M., Ramos, V.A., Dickinson, W.R. (Eds.), Backbone of the Americas: Shallow Subduction, Plateau Uplift, and Ridge and Terrane Collision: Geological Society of America Memoir, 204, pp. 99–124

Cashman, K.V., and Marsh, B.D., 1988, Crystal size distribution (CSD) in rocks and the kinetics and dynamics of crystallization II: Makaopuhi lava lake: Contributions to Mineralogy and Petrology, v. 99, no. 3, p. 292-305.

Cashman K V. 1993 Relationship between plagioclase crystallization and cooling rate in basaltic melts Contrib. to Mineral. Petrol. 113 126–42

Cashman, K. V. (2020). Crystal size distribution (CSD) analysis of volcanic samples: advances and challenges. *Front. Earth Sci.* 8, 1–17. doi:10.3389/feart.2020.00291

Coleman, D.S., Gray, W., and Glazner, A.F., 2004, Rethinking the emplacement and evolution of zoned plutons: Geochronologic evidence for incremental assembly of the Tuolumne Intrusive Suite, California: Geology, v. 32, no. 5, p. 433-436.

Corry, C.E., 1988, Laccoliths: Mechanics of Emplacement and Growth: Geological Society of America Special Paper 220, 127 p.

Cruden, A.R., McCaffrey, K.J.W., 2001. Growth of plutons by floor subsidence: implications for rates of emplacement, intrusion spacing and melt extraction mechanisms. Phys. Chem. Earth 26 (4–5), 303–315.

Cruden A.R., Bunger A.P., 2010. Emplacement dynamics of laccoliths, sills and dykes from dimensional scaling and mechanical models. LASI 4 Conference, abstract.

Cruden A.R., McCaffrey K.J.W., Bunger A.P., 2017. Geometric Scaling of Tabular Igneous Intrusions: Implications for Emplacement and Growth. In: Breitkreuz C., Rocchi S. (eds) Physical Geology of Shallow Magmatic Systems. Advances in Volcanology p 1-28

Currier, R.M., and Marsh, B.D., 2009, Mapping real time growth of experimental laccoliths: The effect of solidification on the mechanics of magmatic intrusion: Journal of Volcanology and Geothermal Research, v. 184, p. 493-494, doi: 10.1016/S0377-0273(09)00247-9.

Flowers, R. M., 2010, The enigmatic rise of the Colorado Plateau: Geology, v. 38, no. 7, p. 671-672

Gilbert, G.K., 1877, Report on the geology of the Henry Mountains: U.S. Geological Survey, 170 p.

Glazner, A.F., Bartley, J.M., Coleman, D.S., Gray, W., and Taylor, R.Z., 2004, Are plutons assembled over millions of years by amalgamation from small magma chambers? GSA Today, v. 14, no. 4/5, p. 4-12

Gonnermann, H., and Taisne, B., 2015, Chapter 10 - Magma Transport in Dikes, *in* Sigurdsson, H., ed., The Encyclopedia of Volcanoes (Second Edition): Amsterdam, Academic Press, p. 215-224.

Gudmundsson, A., 1986. Formation of crustal magma chambers in Iceland. Geology 14,164–166.

Gudmundsson, A., 1990. Emplacement of dikes, sills and crustal magma chambers at divergent plate boundaries. Tectonophysics 176, 257–275.

Gwyn, N., 2011. Progressive assembly of complex intrusions in the shallow crust, Henry Mountains, Utah. M.S. thesis, East Carolina Univ., 100 pp.

Higgins, M.D., 2000, Measurement of crystal size distributions: American Mineralogist, v. 85, no. 8-9, p. 1105–1116.

Higgins, M. D. (2006). QuantitativeTextural Measurements in Igneous and Metamorphic Petrology. Cambridge: Cambridge University Press

Hitchen K, Ritchie JD (1993) New K-Ar ages, and a provisional chronology, for the offshore part of the British Tertiary Igneous Province. Scott J Geol 29:73–85

Hogan, J.P., and Gilbert, M.C., 1995, The A-type Mount Scott Granite sheet: Importance of crustal magma traps: Journal of Geophysical Research, v. 100, p. 15,779–15,792, doi: 10.1029/94JB03258.

Hogan, J.P., Price, J.D., and Gilbert, M.C., 1998, Magma traps and driving pressure: Consequences for pluton shape and emplacement in an extensional regime: Journal of Structural Geology, v. 20, p. 1155–1168, doi: 10.1016/S0191-8141(98)00063-7.

Horsman, E., Tikoff, B., and Morgan, S., 2005, Emplacement-related fabric and multiple sheets in the Maiden Creek sill, Henry Mountains, Utah, USA: Journal of Structural Geology, v. 27, no. 8, p. 1426–1444.

Horsman, E., Morgan, S., de Saint-Blanquat, M., Habert, G., Nugent, A., Hunter, R.A., and Tikoff, B., 2010, Emplacement and assembly of shallow intrusions from multiple magma pulses, Henry Mountains, Utah: Earth and Environmental Science Transactions of the Royal Society of Edinburgh, v. 100, p. 117-132, doi: 10.1017/S1755691009016089.

Horsman, E., Broda, R.J., Gwyn, N.Z., Maurer, E.A., Thornton, E.D., & Ward, M.D., 2018. Progressive construction of laccolithic intrusive centers, Henry Mountains, Utah, U.S.A. In: Breitkreuz, C. & Rocchi, S. (eds), Physical Geology of High-Level Magmatic Systems, a volume in the Advances in Volcanology book series.

Hrouda, F.,1982 Magnetic anisotropy of rocks and its application in geology and geophysics. Geophys Surv 5:37–82

Hunt, C.B., Averitt, P., and Miller, R.L., 1953, Geology and Geography of the Henry Mountains Region, Utah: US Geological Survey Professional Paper 228, 234 p.

Hunt, C.B., 1956, Cenozoic Geology of the Colorado Plateau: US Geological Survey Professional Paper 279, 99 p

Hutchinson, J.W., 1996. Stresses and failure modes in thinfilms and multilayers.Technical University of Denmark, Lyngby, pp. 1–45.

Jackson, M.D., and Pollard, D.D., 1988, The laccolith-stock controversy - new results from the southern Henry Mountains, Utah: Geological Society of America Bulletin, v. 100, no. 1, p. 117-139.

Jackson, M.D., and Pollard, D.D., 1990, Flexure and faulting of sedimentary host rocks during growth of igneous domes, Henry Mountains, Utah: Journal of Structural Geology, v. 12, no. 2, p. 185-206. 84

Johnson, A.M., and Pollard, D.D., 1973, Mechanics of growth of some laccolithic intrusions in the Henry Mountains, Utah, I, Tectonophysics, v. 18, 261-309.

Kavanagh, J.L., Menand, T., Sparks, R.S.J., 2006. An experimental investigation of sill formation and propagation in layered elastic media. Earth Planet. Sci. Lett. 245,799–813

Le Bas, M.J., Lemaitre, R.W., Streckeisen, A., and Zanettin, B. (1986). A chemical classification of volcanic-rocks based on the total alkali silica diagram: Journal of Petrology, v. 27, no. 3, p. 745-750

Le Maitre, R.W., Bateman, P., Dudek, A., Keller, J., Lameyre, M., Le Bas, M.J., Sabine, P.A., Schmid, R., Sørenson, H., Streckeisen, A., Woolley, A.R. & Zanettin, B., 1989. A Classification of Igneous Rocks and a Glossary of Terms. Recommendations of the International Union of Geological Sciences Subcommission on the Systematics of Igneous Rocks. Blackwell Scientific Publications, Oxford. p.193.

Marsh, B.D., Crystal size distribution (CSD) in rocks and the kinetics and dynamics of crystallization I. Theory Contributions to Mineralogy and Petrology, 1988, vol. 99 (pg. 277-291)

Maurer, E., 2015. Geometry and construction history of the Copper Ridge laccolith, Mount Ellen, Henry Mountains, Utah. East Carolina University, M.S. thesis, 104 pp.

McDonough, W.F., and Sun, S.-s., 1995, The composition of the Earth: Chemical Geology, v. 120, no. 3–4, p. 223–253.

Menand, T., 2008. The mechanics and dynamics of sills in layered elastic rocks and their implications for the growth of laccoliths and other igneous complexes. Earth Planet.Sci. Lett. 267, 93–99

Menand, T., Annen, C., and de Saint Blanquat, M., 2015, Rates of magma transfer in the crust: Insights into magma reservoir recharge and pluton growth: Geology, v. 43, p. 199-202, doi: 10.1130/G36224.1.

Menand, T., 2011, Physical controls and depth of emplacement of igneous bodies: A review: Tectonophysics, v. 500, p. 11-19, doi: doi.org/10.1016/j.tecto.2009.10.016.

Michaut, C., Jaupart, C., 2006.Ultra-rapid formation of large volumes of evolved magma. Earth Planet. Sci. Lett. 250, 38–52.

Michel, J., Baumgartner, L., Putlitz, B., Schaltegger, U., and Ovtcharova, M., 2008, Incremental growth of the Patagonian Torres del Paine laccolith over 90 ky: Geology, v. 36, no. 6, p. 459–462.

Mock, A., Jerram, D.A., and Breitkreuz, C., 2003, Using quantitative textural analysis to understand the emplacement of shallow-level rhyolitic laccoliths—A case study from the Halle Volcanic Complex, Germany: Journal of Petrology, v. 44, no. 5, p. 833–849.

Morgan, S., Stanik, A., Horsman, E., Tikoff, B., de Saint Blanquat, M., and Habert, G., 2008, Emplacement of multiple magma sheets and wall rock deformation: Trachyte Mesa intrusion, Henry Mountains, Utah: Journal of Structural Geology, v. 30, no. 4, p. 491–512.

Morton LB (1984) Geology of the Mount Ellen quadrangle, Henry Mountains, Garfield County, Utah. Brigham Young Univ Geol Stud 331:67–95

Morton, L.B., 1986, Provisional geologic and coal resource map of the Mt. Ellen quadrangle, Garfield County, Utah [Master's Thesis]: Brigham Young University, scale: 1:24,000.

Murray, K.E., Reiners, P.W., and Thomson, S.N., 2016, Rapid Pliocene–Pleistocene erosion of the central Colorado Plateau documented by apatite thermochronology from the Henry Mountains: Geology (Boulder), v. 44, p. 483-486, doi: 10.1130/G37733.1.

Mussett AE, Dagley P, Skelhorn RR (1988) Time and duration of activity in the British Tertiary Volcanic Province. In: Morton AC, Parson LM (eds) Early Tertiary volcanism and opening of the NE Atlantic. Geol Soc Lond Spec Pub 39:337–348

Nelson, S.T., Davidson, J.P., and Sullivan, K.R., 1992. New age determinations of central Colorado Plateau laccoliths, Utah: Recognizing disturbed K-Ar systematics and reevaluating tectonomagmatic relationships. Geological Society of America Bulletin, 855 104: 1547–1560.

Nelson, S.T., Davidson, J.P.,1993. Interactions between mantle-derived magmas and mafic crust, Henry Mountains, Utah.J. Geophys.Res. B2 98, 1837e1852.

Parson, T., Sleep, N.H., Thompson, G.A., 1992. Host rock rheology controls on the emplacement of tabular intrusions: implications for underplating of extended crust. Tectonics 11, 1348–1356

Pederson, J. L., R. D. Mackley, and J. L. Eddleman, 2002, Colorado Plateau uplift and erosion evaluated using GIS, GSA Today, 12, 4 – 10, doi:10.1130/1052-5173(2002)0122.0.CO;2.

Pollard DD, Johnson AM (1973) Mechanics of growth of some laccolith intrusions in the Henry Mountains, Utah, Part II. Tectonophysics 18:311–354

Pollard DD, Muller OH, Dockstader DR (1975) The form and growth of fingered sheet intrusions. Geol Soc Am Bull 86:351– 363

Putlitz, B., Baumgartner, L.P., Oberhaensli, R., Diamond, L., and Altenberger, U., 2001, The Torres del Paine laccolith (Chile): Intrusion and metamorphism: Virginia, USA, XI Annual V.M. Goldschmidt Conference Proceedings, abs. 3534

Randolph, A. D. & Larson, M. A. (1971). Theory of Particulate Processes. New York: Academic Press.

Reches, Z., and Fink, J., 1988, The mechanism of intrusion of the Inyo Dike, Long Valley Caldera, California: Journal of Geophysical Research, v. 93, no. B5, p. 4321–4334.

Rivalta, E., Taisne, B., Bunger, A.P., and Katz, R.F., 2015, A review of mechanical models of dike propagation: Schools of thought, results and future directions: Tectonophysics, v. 638, p. 1-42, doi: https://doi.org/10.1016/j.tecto.2014.10.003.

Rollinson, H.R., 2013, Using Geochemical Data: Evaluation, Presentation, Interpretation: New York, Routledge, 352 p

Rocchi, S., Westerman, D.S., Dini, A., Innocenti, F., and Tonarini, S., 2002, Two-stage laccolith growth at Elba Island (Italy): Geology, v. 30, p. 983–986, doi: 10.1130/ 0091-7613(2002)0302.0.CO;2.

Rocchi, S., Westerman, D.S., Dini, A., and Farina, F., 2010, Intrusive sheets and sheeted intrusions at Elba Island, Italy: Geosphere, v. 6, no. 3, p. 225-236.

Ross, M.L., 1992, Geology and petrology of the Oligocene North Mountain intrusive center, La Sal Mountains, Utah: Geological Society of America Abstracts with Programs, v. 24, no. 6, p. 59.

Rubin, A.M., 1995, Propagation of Magma-Filled Cracks: Annual Review of Earth and Planetary Sciences, v. 23, p. 287-336, doi: 10.1146/annurev.ea.23.050195.001443.

Saint Blanquat (de), M., Habert, G., Horsman, E., Morgan, S.S., Tikoff, B., Launeau, P., and Gleizes, G., 2006, Mechanisms and duration of non-tectonically assisted magma emplacement in the upper crust: The Black Mesa pluton, Henry Mountains, Utah: Tectonophysics, v. 428, p. 1-31, doi: 10.1016/j.tecto.2006.07.014.

Saint Blanquat (de), M., Horsman, E., Habert, G., Morgan, S., Vanderhaeghe, O., Law, R., and Tikoff, B., 2011, Multiscale magmatic cyclicity, duration of pluton construction, and the paradoxical relationship between tectonism and plutonism in continental arcs: Tectonophysics, v. 500, no. 1-4, p. 20–33.

Thompson, G.A., and Zoback, M.L., 1979, Regional geophysics of the Colorado Plateau: Tectonophysics, v. 61, no. 1–3, p. 149–181

Thomson, K. and Hutton, D., 2004. Geometry and growth of sill complexes: insights using 3D seismic from the North Rockall Trough. *Bulletin of Volcanology*, *66*(4), pp.364-375.

Thornton, E., 2015. Timing, internal flow characteristics, and emplacement mechanisms 916 of the intrusive sheet network on the southern margin of Mount Hillers, Henry Mountains, southern Utah. East Carolina University, M.S. thesis, 104 pp.

Trexler, C., 2014, Tectonic and Landscape Evolution of the Colorado Plateau. Ecogeomorphology report, UC Davis

Upton BGJ (1988) History of Tertiary igneous activity in the North Atlantic borderlands. In: Morton AC, Parsons LM (eds) Early Tertiary volcanism and the opening of the NE Atlantic. Geol Soc Lond Spec Publ 39:429–454

Vigneresse, J.L., and Clemens, J.D., 2000, Granitic magma ascent and emplacement: neither diapirism nor neutral buoyancy: Geological Society of London Special Publication, v. 174, no. 1, p. 1-19.

Walker, F., Schofield, N., Millett, J., Jolley, D., Holford, S., Planke, S., Jerram, D.A., and Myklebust, R., 2020, Inside the volcano: Three-dimensional magmatic architecture of a buried shield volcano: Geology, , doi: 10.1130/G47941.1.

Ward, M., 2014. Geometry and construction history of a complex intrusive center in the shallow crust, Mount 928 Pennell, Henry Mountains, Utah. East Carolina University, M.S. thesis, 130 pp.

Westerman, D.S., Dini, A., Innocenti, F., and Rocchi, S., 2004, Rise and fall of a nested Christmas-tree laccolith complex, Elba Island, Italy, in Breitkreuz, C., and Petford, N., eds., Physical geology of high-level magmatic systems: Geological Society of London Special Publication 234, p. 195–213

Wiebe, R.A., and Collins, W.J., 1998, Depositional features and stratigraphic sections in granitic plutons: implications for the emplacement and crystallization of granitic magma: Journal of Structural Geology, v. 20, p. 1273-1289, doi: 10.1016/S0191-8141(98)00059-5.

Witkind, I.J., 1964, Geology of the Abajo Mountains area, San Juan County, Utah: U.S. Geological Survey Professional Paper453, 110 p.

11. Appendices

11.1 Appendix A: Geochemistry Data

Table 6. Whole-rock major-element compositions for rocks with Texture 1

Texture 1 Geochemistry - Major Elements												
	Major Element Weight %											
Sample	**Al_2O_3**	**CaO**	**Cr_2O_3**	**Fe_2O_3**	**K_2O**	**MgO**	**MnO**	**Na_2O**	**P_2O_5**	**SiO_2**	**TiO_2**	**LOI**	**Total**
CR82	17.28	5.26	0.003	7.27	1.86	2.02	0.15	5.05	0.23	59.09	0.62	0.9	99.733
CR19	17.02	6.19	0.004	6.9	1.87	1.97	0.13	4.25	0.21	58.65	0.61	1.9	99.704
CR66	16.98	6.62	0.004	6.67	1.89	1.66	0.11	4.31	0.22	58.12	0.6	2.5	99.684
CR71	16.75	6.32	0.004	7.14	1.9	1.79	0.14	4.13	0.21	58.72	0.59	2	99.694
CR95	16.71	6.41	0.004	6.88	1.71	1.6	0.12	4.19	0.22	58.12	0.57	3.2	99.734
CR114	17.34	5.44	0.003	6.59	1.86	1.95	0.13	4.3	0.21	60.11	0.59	1.2	99.723
ME8	17.41	4.52	0.003	6.86	1.88	1.94	0.12	4.59	0.24	59.82	0.61	1.7	99.693
ME9	17.46	5.43	0.004	6.9	1.84	1.86	0.13	4.19	0.22	59.93	0.6	1.2	99.764
CR1	17.64	4.65	0.003	5.33	1.87	1.55	0.13	4.27	0.23	61.7	0.55	1.8	99.723
CR12	17.22	5.33	0.003	5.41	1.79	2.02	0.12	4.68	0.19	60.98	0.48	1.5	99.723
CR31	16.93	5.86	0.002	5.14	1.74	1.55	0.12	4.08	0.2	59.67	0.52	3.9	99.712
CR46	16.67	4.64	<0.002	3.05	1.7	0.88	0.06	4.04	0.14	64.56	0.32	3.6	99.66
ME103	17.14	5.4	0.003	4.89	1.8	1.33	0.1	4.34	0.21	61.3	0.46	2.8	99.773
ME105	17.33	3.95	0.005	4.47	1.95	1.54	0.08	5.29	0.17	62.77	0.4	1.8	99.755
ME119	17.42	6.23	0.004	6.15	2	1.93	0.17	4.56	0.25	58.06	0.58	2.4	99.754
ME120	17.57	5.94	0.003	4.49	1.98	1.06	0.14	4.72	0.18	60.36	0.4	2.9	99.743
ME124	17.5	6.42	0.002	5.64	2.17	1.62	0.15	4.1	0.22	59.63	0.52	1.8	99.772
ME125	18.1	5.2	<0.002	4.0	2.0	1.0	0.1	5.0	0.2	63.1	0.4	0.7	99.7
ME130	17.9	5.7	0.0	4.7	1.9	1.1	0.1	4.5	0.2	62.7	0.5	0.4	99.743
ME133	15.0	4.5	<0.002	4.1	2.0	1.1	0.1	3.7	0.2	67.9	0.4	0.8	99.74
ME138	17.2	5.3	0.0	5.7	2.2	1.7	0.2	4.6	0.2	59.9	0.5	2.3	99.724
ELLN-2	17.34	4.17	-	-	2.85	0.92	0.14	5.16	0.13	62.71	0.35	2.42	96.19
ELLN-3	17.78	5.45	-	-	2.01	1.05	0.14	4.45	0.13	62.26	0.38	2.48	96.13
BULL-1	18.06	5.34	-	-	1.9	1.02	0.14	5.01	0.14	63.35	0.4	0.41	95.77
Average	17.24	5.43	0.00	4.93	1.95	1.51	0.13	4.48	0.20	60.98	0.50	1.94	99.26

Table 7. Whole-rock major-element compositions for rocks with Texture 2

Texture 2 Geochemistry - Major Elements												
	Major Element Weight %											
Sample	**Al_2O_3**	**CaO**	**Cr_2O_3**	**Fe_2O_3**	**K_2O**	**MgO**	**MnO**	**Na_2O**	**P_2O_5**	**SiO_2**	**TiO_2**	**LOI**	**Total**
ME16	16.36	7.7	0.004	8.3	1.68	3.25	0.16	3.44	0.33	52.18	0.85	5.4	99.654
ME19	15.74	7.42	0.005	8.44	1.69	4.01	0.16	3.58	0.25	51.6	0.75	6	99.645
ME134	17.7	6.5	0.0	6.9	2.1	2.1	0.1	4.1	0.3	57.2	0.6	2.1	99.732
Average	16.61	7.19	0.00	7.86	1.83	3.11	0.15	3.72	0.30	53.67	0.74	4.50	99.677

Table 8. Whole-rock major-element compositions for rocks with Texture 3

Texture 3 Geochemistry - Major Elements													
	Major Element Weight %												
Sample	**Al_2O_3**	**CaO**	**Cr_2O_3**	**Fe_2O_3**	**K_2O**	**MgO**	**MnO**	**Na_2O**	**P_2O_5**	**SiO_2**	**TiO_2**	**LOI**	**Total**
CR8	16.96	5.3	<0.002	5.07	1.7	1.21	0.1	4.53	0.2	61.95	0.43	2.3	99.75
CR63	17.43	5.06	<0.002	5.95	1.85	1.49	0.18	4.57	0.21	62.22	0.46	0.3	99.72
CR76	16.92	5.09	0.002	5.47	1.77	1.32	0.12	4.82	0.2	61.23	0.45	2.3	99.692
CR81	17.06	4.34	<0.002	5.85	1.82	1.29	0.14	5.17	0.21	62.26	0.45	1.1	99.69
CR88	16.6	5	<0.002	5.95	1.99	1.4	0.13	4.57	0.21	61.95	0.45	1.5	99.75
CR104	17.16	5.09	<0.002	5.28	1.83	1.26	0.1	4.41	0.19	63.2	0.44	0.8	99.76
CR35	16.53	6.64	0.004	6.4	1.8	2.56	0.14	3.54	0.23	56.82	0.65	4.4	99.714
CR75	17.3	5.35	<0.002	4.59	1.81	1.26	0.11	4.62	0.22	62.59	0.45	1.4	99.7
CR78	16.49	6.02	0.005	6.33	1.33	2.54	0.13	4.49	0.2	58.83	0.6	2.7	99.665
CR37	15.53	7.41	0.009	8.33	1.31	3.26	0.15	3.55	0.25	52.96	0.68	6.2	99.639
CR100	16.53	6.63	0.005	7.3	1.82	2.67	0.13	4.05	0.24	56.29	0.68	3.3	99.645
ME17	17.11	6.73	0.004	7.58	1.65	2.77	0.14	4.11	0.29	56.8	0.71	1.8	99.694
ME20	16.49	4.06	<0.002	3.14	2.2	0.96	0.08	4.89	0.13	65.67	0.3	1.8	99.72
ME21	16.93	3.85	<0.002	2.85	2.09	0.82	0.05	4.92	0.12	66.13	0.28	1.7	99.74
CR67	17.12	5.24	0.003	5.23	1.82	1.57	0.11	4.16	0.21	60.31	0.53	3.4	99.703
ME101	17.91	4.46	0.004	5.33	1.9	1.46	0.1	4.39	0.21	61.34	0.5	2.1	99.704
ME106	17.15	6.16	0.005	6.36	1.78	2.14	0.14	4.25	0.23	57.85	0.64	3	99.705
ME114	16.56	6.65	0.007	8.1	2.03	3.31	0.15	4.14	0.27	55.91	0.69	1.9	99.717
ME117	17.06	7.08	0.006	8.3	1.77	3.3	0.15	4.13	0.23	54.19	0.71	2.8	99.726
ME118	17.87	6.06	0.005	7.68	1.4	2.48	0.13	4.82	0.33	56.28	0.75	1.9	99.705
ME122	18.08	5.68	0.002	5.35	1.98	1.39	0.16	4.7	0.23	60.5	0.5	1.2	99.772
ME123	17.65	6.74	0.003	6.66	1.81	1.92	0.2	4.06	0.28	58.52	0.6	1.3	99.743
ME127	17.9	4.8	<0.002	4.4	1.9	1.0	0.1	4.7	0.2	63.0	0.4	1.4	99.76
ELLN-1	16.76	3.3	-	-	2.13	0.84	0.14	6.29	0.11	67.51	0.31	0.86	98.25
ELLN-6	17.82	6.24	-	-	1.96	1.49	0.16	4.57	0.2	60.81	0.52	0.43	94.2
ELLN-9	17.25	5.59	-	-	1.95	2.73	0.13	4.24	0.21	58.89	0.55	1.64	93.18
Average	17.08	5.56	0.00	5.29	1.82	1.86	0.13	4.49	0.21	60.15	0.53	2.06	99.19

Table 9. Whole-rock major-element compositions for rocks with Texture 4

Texture 4 Geochemistry - Major Elements													
	Major Element Weight %												
Sample	**Al_2O_3**	**CaO**	**Cr_2O_3**	**Fe_2O_3**	**K_2O**	**MgO**	**MnO**	**Na_2O**	**P_2O_5**	**SiO_2**	**TiO_2**	**LOI**	**Total**
ME109	17.55	5.11	0.003	4.14	1.88	1.04	0.07	4.64	0.14	62.68	0.39	2.1	99.743
ME132	16.5	5.5	<0.002	4.8	1.8	1.3	0.1	4.0	0.2	59.9	0.4	5.4	99.75
ME137	16.6	4.6	0.0	3.7	2.9	0.9	0.1	3.9	0.1	62.8	0.3	3.7	99.742
Average	16.88	5.05	0.00	4.19	2.19	1.08	0.09	4.18	0.16	61.81	0.38	3.73	99.745

Table 10. Whole-rock major-element compositions for rocks with Texture 5

Texture 5 Geochemistry - Major Elements													
	Major Element Weight %												
Sample	**Al_2O_3**	**CaO**	**Cr_2O_3**	**Fe_2O_3**	**K_2O**	**MgO**	**MnO**	**Na_2O**	**P_2O_5**	**SiO_2**	**TiO_2**	**LOI**	**Total**
ME10	17.28	6.09	0.003	6.19	1.67	1.94	0.15	4.15	0.2	57.97	0.62	3.5	99.763
ME11	16.84	5.66	0.003	6.07	0.93	2.07	0.15	4.16	0.21	56.83	0.63	5.8	99.353
ME12	17.35	4.68	<0.002	4.04	1.63	0.95	0.12	5.45	0.17	59.47	0.44	5.4	99.7
ME13	17.33	4.88	<0.002	4.39	1.95	1.18	0.11	4.76	0.17	60.47	0.44	4	99.68
ME14	17.78	4.56	<0.002	4.37	1.59	1.37	0.08	4.44	0.17	61.84	0.43	3.1	99.73
ME15	17.01	4.97	0.004	4.61	2.19	1.71	0.09	4.6	0.15	62.36	0.4	1.6	99.694
ME112	18.09	6.07	<0.002	4.94	1.63	1.21	0.13	4.78	0.22	61.69	0.47	0.5	99.73
ME113	18.26	4.68	0.002	5.37	1.72	1.26	0.14	4.03	0.21	61.06	0.48	2.5	99.712
ME116	17.32	7.23	0.004	6.63	1.47	2.35	0.13	4.1	0.21	55.95	0.57	3.8	99.764
ME129	17.9	4.8	<0.002	4.4	1.8	0.7	0.1	4.5	0.1	63.7	0.3	1.5	99.76
ME136	17.4	5.3	<0.002	4.4	1.8	1.0	0.1	4.6	0.2	61.7	0.4	2.9	99.66
ELLN-4	17.02	7.88	-	-	1.86	3.47	0.17	3.97	0.3	53.82	0.88	1.83	91.2
ELLN-5	16.75	5.08	-	-	1.98	1.8	0.14	4.64	0.14	62.81	0.42	2.09	95.85
ELLN-10	15.73	6.7	-	-	1.41	5.59	0.13	3.49	0.25	52.1	0.8	4.75	90.95
ELLN-11	16.05	0.51	-	-	1.15	1.8	0.12	4.11	0.24	58.75	0.51	1.1	84.34
ELLN-11i-B	15.23	10.31	-	-	0.56	6.66	0.19	3.69	0.22	51.17	0.51	1	89.54
Average	17.08	5.59	0.00	5.03	1.58	2.19	0.13	4.34	0.20	58.86	0.52	2.84	96.78

Table 11. Whole-rock trace-element compositions for rocks with Texture 1

	Texture 1 Geochemistry Data - Trace Elements																								
	Samples #																								
Trace Element (ppm)	CR82	CR19	CR66	CR71	CR95	CR114	ME8	ME9	CR1	CR12	CR31	CR46	ME103	ME105	ME119	ME120	ME124	ME125	ME130	ME133	ME138	ELLN-2	ELLN-3	BULL-1	Average
Ag	0.1	<0.1	<0.1	<0.1	<0.1	<0.1	<0.1	<0.1	<0.1	<0.1	<0.1	0.4	<0.1	<0.1	<0.1	<0.1	<0.1	<0.1	<0.1	<0.1	<0.1	-	-	-	0.02
As	0.7	1.1	0.9	1	0.6	<0.5	<0.5	<0.5	0.6	<0.5	<0.5	17.2	<0.5	1.5	0.6	<0.5	<0.5	<0.5	1.0	<0.5	0.9	-	-	-	1.04
Au (ppb)	0.6	<0.5	<0.5	<0.5	<0.5	<0.5	<0.5	<0.5	<0.5	0.7	1.8	<0.5	2.5	<0.5	0.6	<0.5	<0.5	<0.5	1.2	<0.5	<0.5	-	-	-	0.30
Ba	625	718	699	680	701	657	737	741	738	784	805	952	768	760	593	710	602	776.0	668.0	781.0	723.0	748	580	737	691.32
Be	<1	2	<1	<1	<1	<1	<1	<1	3	<1	1	<1	2	2	<1	<1	<1	<1	<1	<1	2.0	-	-	-	0.48
Bi	<0.1	<0.1	<0.1	<0.1	<0.1	<0.1	<0.1	<0.1	<0.1	<0.1	<0.1	<0.1	<0.1	0.1	0.2	<0.1	<0.1	<0.1	<0.1	<0.1	0.2	-	-	-	0.02
Cd	0.3	<0.1	<0.1	<0.1	<0.1	<0.1	<0.1	<0.1	<0.1	<0.1	0.2	2	<0.1	<0.1	<0.1	<0.1	<0.1	<0.1	<0.1	<0.1	<0.1	-	-	-	0.10
Ce	41.9	47.6	43.3	36.5	47.7	37.1	37.5	48.7	36.2	32.4	49	26.2	37.2	26.9	54.8	50.5	53.2	47.2	49.1	32.6	51.7	-	-	-	35.49
Co	10.8	12.3	11.8	10.8	11.3	10.4	11.2	11.4	10.6	10.7	9.7	1.5	6	8.6	9.8	5.2	8.2	4.7	4.4	5.6	9.9	-	-	-	7.40
Cs	0.3	0.6	0.6	0.6	0.7	0.6	1.4	0.6	0.2	0.4	0.9	1.5	0.2	0.4	0.2	2	0.5	1.7	0.2	<0.1	0.5	-	-	-	0.56
Cu	17.6	19	21.2	19.1	18.8	20.2	25.5	20.6	15.6	14.8	16.3	2.9	5.5	10.4	15.6	5.6	6.6	7.0	42.8	3.1	13.0	-	-	-	12.85
Dy	3.43	3.15	3.3	3.28	3.45	3.19	3.17	3.33	3.2	2.63	3.5	1.71	2.73	1.43	4.1	3.19	3.34	2.7	3.4	2.0	3.7	-	-	-	2.56
Er	2.05	2.02	2.01	2.18	1.95	1.85	1.83	1.94	2.19	1.6	2.07	1.03	1.61	0.94	2.35	1.91	2.08	1.9	2.0	1.3	2.2	-	-	-	1.56
Eu	1.31	1.28	1.29	1.23	1.26	1.33	1.26	1.34	1.19	1.08	1.39	0.81	1.17	0.75	1.53	1.26	1.36	1.1	1.4	0.9	1.4	-	-	-	1.03
Ga	19.6	18.6	19	18.6	18.1	18.4	18	20.2	17.6	18.6	19.7	18.2	18.8	20.1	18.6	17.8	17.7	17.8	17.6	14.1	16.8	-	-	-	15.36
Gd	4.07	3.87	3.88	3.82	3.93	3.86	3.6	4.22	4.01	3.09	4.27	2.23	3.52	2.08	4.5	3.68	4.16	3.3	4.2	2.8	4.0	-	-	-	3.08
Hf	3.6	3.7	3.1	3.8	3.5	3.7	3.6	3.7	3.7	3	3.8	3.3	3.1	2.9	3.4	3.4	3	3.5	3.7	2.7	3.4	-	-	-	2.86
Hg	<0.01	<0.01	<0.01	<0.01	<0.01	<0.01	<0.01	<0.01	0.01	<0.01	0.01	0.02	<0.01	<0.01	<0.01	<0.01	<0.01	<0.01	<0.01	<0.01	<0.01	-	-	-	0.00
Ho	0.71	0.66	0.72	0.64	0.63	0.68	0.64	0.68	0.69	0.6	0.71	0.35	0.54	0.31	0.85	0.67	0.7	0.6	0.7	0.5	0.7	-	-	-	0.53
La	19.6	24.2	21.7	18.1	23.3	18.4	17.9	25.8	19.1	17	24.8	13.4	18.1	14.9	27.5	26.8	28.1	25.0	26.1	15.5	27.2	20	24	26	20.90
Lu	0.3	0.31	0.31	0.31	0.31	0.3	0.32	0.32	0.32	0.24	0.31	0.16	0.23	0.15	0.37	0.31	0.31	0.3	0.3	0.2	0.3	-	-	-	0.24
Mo	0.3	0.4	0.3	0.3	0.5	0.2	0.3	0.1	0.2	<0.1	0.3	0.1	0.4	0.2	0.9	0.2	0.5	0.1	0.6	<0.1	0.5	-	-	-	0.26
Nb	6.6	6.2	5.7	6.3	5.9	6.4	5.9	6.4	6.4	4	6.7	5.4	4.7	3.7	5.1	5	5.2	5.2	6.2	4.4	5.4	5	6	6	5.35
Nd	21.2	23.2	22.5	18.9	23.6	18.9	18.2	23	21.4	16.4	23.2	13.9	18.6	13.6	27	22.3	24.1	21.7	24.2	16.9	25.1	-	-	-	17.52
Ni	5	8	6.7	5.2	7.9	5.3	7.9	5.9	<20	<20	<20	<20	<20	<20	<20	<20	<20	1.6	1.0	1.8	5.5	<10	<10	<10	2.47
Pb	32	4	4.1	4.9	3.7	2.9	3.4	2	6.1	5.9	3.8	13	2.4	2.9	11.3	3.6	3.4	2.6	3.1	1.3	19.1	18	13	22	7.54
Pr	5.31	5.92	5.21	4.76	5.54	4.93	4.76	5.66	4.88	4.14	5.94	3.31	4.45	3.23	6.49	5.78	6.22	5.4	6.0	3.9	6.2	-	-	-	4.33
Rb	27.7	26.8	29.7	30.5	26.5	25.7	28.3	26.7	27.6	26.9	30.7	30.3	20	28.7	31.1	31.9	34.6	30.9	23.1	18.2	33.8	44	32	32	27.91
Sb	0.1	<0.1	<0.1	<0.1	<0.1	<0.1	<0.1	<0.1	<0.1	<0.1	<0.1	<0.1	<0.1	<0.1	<0.1	<0.1	<0.1	<0.1	<0.1	<0.1	<0.1	-	-	-	-
Sc	10	10	10	9	9	10	10	10	8	10	8	3	6	6	8	5	7	5.0	6.0	5.0	8.0	-	-	-	6.52
Se	<0.5	<0.5	<0.5	<0.5	<0.5	<0.5	<0.5	<0.5	0.8	1.4	1	1.9	<0.5	<0.5	<0.5	<0.5	<0.5	<0.5	<0.5	<0.5	<0.5	-	-	-	0.20
Sm	4.67	4.23	4.36	3.96	4.3	4.18	4.02	4.58	4.38	3.46	4.88	2.55	3.72	2.63	5.3	4.12	4.76	4.0	4.8	3.3	4.8	-	-	-	3.48
Sn	<1	1	<1	1	<1	<1	<1	<1	<1	<1	1	<1	<1	<1	<1	<1	<1	4.0	4.8	3.3	4.8	-	-	-	0.79
Sr	893.9	1020.7	918.1	991.2	993.8	1029	967.1	1019.6	933	1092.8	1102.4	1042.5	963.3	1148	936.9	1088.8	1063.1	1186.0	964.2	865.4	990.4	991	915	1277	975.73
Ta	0.3	0.3	0.3	0.3	0.3	0.3	0.3	0.4	0.4	0.2	0.3	0.2	0.3	0.2	0.3	0.3	0.3	0.2	0.3	0.3	0.2	-	-	-	0.24
Tb	0.59	0.58	0.57	0.57	0.56	0.58	0.53	0.63	0.56	0.47	0.6	0.3	0.48	0.29	0.68	0.52	0.58	0.5	0.6	0.4	0.6	-	-	-	0.45
Th	2.4	3.1	2.9	2.2	3.4	2.7	2.4	2.9	2.6	2.9	3.5	1.8	2.7	3.6	5.1	6.5	4.6	6.1	4.2	2.2	4.5	3	4	4	3.33
Tl	<0.1	<0.1	<0.1	<0.1	<0.1	<0.1	<0.1	<0.1	<0.1	<0.1	<0.1	<0.1	<0.1	<0.1	<0.1	<0.1	<0.1	<0.1	<0.1	<0.1	<0.1	-	-	-	-
Tm	0.33	0.3	0.3	0.32	0.28	0.3	0.29	0.3	0.31	0.24	0.32	0.16	0.22	0.13	0.35	0.27	0.29	0.3	0.3	0.2	0.3	-	-	-	0.23
U	1.3	1.3	1	1.1	1.1	1.2	0.9	1	1.3	1.3	1.6	1.1	1	1.6	1.8	2	1.3	1.6	1.6	0.9	2.1	3	1	1	1.32
V	104	101	103	92	96	100	105	105	77	125	88	46	61	73	97	60	81	60.0	55.0	53.0	96.0	-	-	-	71.12
W	<0.5	<0.5	<0.5	0.8	<0.5	<0.5	<0.5	<0.5	<0.5	<0.5	0.6	0.6	0.5	<0.5	<0.5	<0.5	<0.5	0.7	0.6	<0.5	0.5	-	-	-	0.17
Y	19.5	19.3	19.6	19.3	18.2	19.3	18.2	19.8	19.1	14.1	19.6	9.2	15.3	8.7	21.9	18.3	19	16.6	20.2	12.1	19.9	17	22	18	16.97
Yb	1.86	2.04	2	1.98	1.8	1.97	2.02	1.99	1.99	1.58	2.11	1.04	1.45	0.93	2.45	1.98	2.07	1.8	2.1	1.3	2.3	-	-	-	1.55
Zn	173	47	31	58	57	39	43	37	57	32	86	387	58	49	66	60	30	42.0	19.0	29.0	67.0	-	-	-	58.68
Zr	141.6	136.2	128.7	155.9	131.4	130.1	135.9	138.2	135.9	106.7	152.7	126.4	111.5	98	119.2	128.3	113.7	131.9	134.5	99.1	120.5	171	172	204	128.94

Table 12. Whole-rock trace-element compositions for rocks with Texture 2

Texture 2 Geochemistry Data - Trace Elements				
	Samples #			
Trace Element (ppm)	ME16	ME19	ME134	Averages
Ag	<0.1	<0.1	<0.1	-
As	2.5	<0.5	<0.5	0.83
Au (ppb)	<0.5	0.8	0.6	0.47
Ba	686	700	695.0	693.67
Be	2	<1	<1	0.67
Bi	<0.1	<0.1	<0.1	-
Cd	<0.1	<0.1	<0.1	-
Ce	55.5	41.5	54.8	50.60
Co	19	21.7	11.9	17.53
Cs	0.2	0.3	0.4	0.30
Cu	49.9	56.9	26.5	44.43
Dy	3.65	2.96	3.6	3.39
Er	2.15	1.62	2.4	2.04
Eu	1.56	1.32	1.6	1.48
Ga	19.7	17.3	16.4	17.80
Gd	4.65	3.7	4.7	4.34
Hf	3.3	2.4	2.9	2.87
Hg	<0.01	<0.01	<0.01	-
Ho	0.78	0.57	0.8	0.71
La	28.2	21.8	28.2	26.07
Lu	0.32	0.24	0.4	0.31
Mo	0.3	0.7	0.3	0.43
Nb	5.4	3.8	5.2	4.80
Nd	28	21.7	28.8	26.17
Ni	<20	25	2.7	9.23
Pb	3.5	3.6	2.4	3.17
Pr	6.7	5.14	6.8	6.20
Rb	25.2	26.1	38.5	29.93
Sb	<0.1	<0.1	0.1	0.03
Sc	16	18	9.0	14.33
Se	1.4	0.9	<0.5	0.77
Sm	5.15	4.43	5.4	4.98
Sn	1	<1	5.4	2.12
Sr	1044.6	903.5	1032.2	993.43
Ta	0.2	0.2	0.3	0.23
Tb	0.66	0.55	0.7	0.63
Th	4.1	3.9	4.9	4.30
Tl	<0.1	<0.1	<0.1	-
Tm	0.29	0.26	0.3	0.29
U	1.6	1.6	2.0	1.73
V	208	204	113.0	175.00
W	<0.5	<0.5	<0.5	-
Y	20	15.4	21.6	19.00
Yb	1.89	1.79	2.4	2.02
Zn	87	73	41.0	67.00
Zr	125.5	89.8	108.2	107.83

Table 13. Whole-rock trace-element compositions for rocks with Texture

	Texture 3 Geochemistry Data - Trace Elements																										
	Samples #																										
Trace Element (ppm)	CR8	CR63	CR76	CR81	CR88	CR104	CR35	CR75	CR78	CR37	CR100	ME17	ME20	ME21	CR67	ME101	ME106	ME114	ME117	ME118	ME122	ME123	ME127	ELLN-1	ELLN-6	ELLN-9	Averages
Ag	<0.1	<0.1	<0.1	<0.1	<0.1	<0.1	<0.1	<0.1	<0.1	<0.1	<0.1	<0.1	<0.1	<0.1	<0.1	<0.1	<0.1	<0.1	<0.1	<0.1	<0.1	<0.1	<0.1	-	-	-	-
As	0.6	1	6.4	0.8	2.1	1.4	0.6	0.6	13.1	1.9	9.8	1.1	<0.5	<0.5	0.6	2.1	<0.5	<0.5	<0.5	<0.5	1.1	<0.5	<0.5	-	-	-	1.66
Au (ppb)	<0.5	<0.5	<0.5	<0.5	<0.5	<0.5	0.6	<0.5	<0.5	<0.5	<0.5	0.7	0.6	1.2	1.6	1	0.5	<0.5	<0.5	<0.5	<0.5	1.3	1.2	-	-	-	0.33
Ba	889	850	994	970	934	812	771	912	918	700	725	667	982	968	753	764	646	735	601	622	632	546	772.0	901	680	798	759.38
Be	2	<1	<1	2	<1	<1	<1	2	<1	<1	<1	<1	3	1	<1	1	2	2	<1	<1	<1	<1	<1	-	-	-	0.58
Bi	<0.1	<0.1	<0.1	<0.1	<0.1	<0.1	<0.1	<0.1	0.3	<0.1	<0.1	<0.1	<0.1	<0.1	<0.1	0.2	<0.1	<0.1	<0.1	0.2	<0.1	<0.1	0.1	-	-	-	0.03
Cd	<0.1	<0.1	<0.1	0.4	0.1	<0.1	<0.1	<0.1	<0.1	0.1	<0.1	<0.1	0.1	<0.1	<0.1	<0.1	0.2	<0.1	<0.1	<0.1	<0.1	<0.1	<0.1	-	-	-	0.03
Ce	32.1	36.7	34.9	33.5	31.5	31.4	55.4	38.7	52.4	55.9	49.7	39.9	18.2	17.5	41.4	35.9	43.3	44.1	41.9	55.3	51.9	58	35.6	-	-	-	35.97
Co	6.5	7.6	7.8	7.5	7.4	6.8	15.8	6.6	14.4	21.2	15.4	15.8	4.4	3.6	9.1	8.8	12.3	19.2	17.8	14.2	7.2	10	14.9	-	-	-	9.78
Cs	1.1	1.1	0.7	1.6	0.8	0.8	0.6	0.7	0.8	0.7	0.4	0.6	0.7	1.2	0.2	0.3	0.6	0.8	0.2	0.1	0.4	0.2	0.4	-	-	-	0.58
Cu	6.4	14.4	9.2	10.7	11.9	5.4	36.3	10.5	31.2	55.7	25.2	29.5	16.2	5.4	15.5	22.9	21.2	45	36.1	9	9.6	16.6	13.6	-	-	-	17.60
Dy	2.52	2.58	2.49	2.64	2.67	2.61	3.21	2.86	3.1	3.17	3.09	3.38	1.23	1.13	3.3	2.79	3.63	3.35	3.36	3.83	3.69	3.84	2.5	-	-	-	2.58
Er	1.44	1.56	1.43	1.51	1.58	1.33	1.9	1.77	1.85	1.78	1.58	1.98	0.7	0.65	1.93	1.73	2.21	2.07	1.95	2.25	2.15	2.34	1.6	-	-	-	1.51
Eu	1.04	1.19	1.16	1.21	1.17	0.99	1.42	1.3	1.35	1.42	1.38	1.32	0.57	0.62	1.15	1.21	1.45	1.41	1.33	1.64	1.4	1.54	1.0	-	-	-	1.09
Ga	17.8	19	18.5	18.7	18.6	17.6	19.5	18.6	19.4	17.6	18.5	17.3	17.1	18.1	19.3	19.5	18.6	18	18.1	19.7	18.3	18.8	18.3	-	-	-	16.34
Gd	3.06	3.6	3.44	3.23	3.34	3.06	4.17	3.8	3.83	4.47	3.98	4.23	1.82	1.6	3.88	3.54	4.2	4.31	3.84	5.07	4.32	4.8	3.0	-	-	-	3.25
Hf	3.1	3.2	2.9	3.1	2.8	3	3.2	3.1	3.1	2.8	2.9	3.1	2.4	2.7	3.7	3.5	3.8	2.9	2.4	3.2	3.6	3.4	3.3	-	-	-	2.74
Hg	<0.01	<0.01	<0.01	0.01	<0.01	<0.01	<0.01	<0.01	<0.01	<0.01	<0.01	<0.01	<0.01	<0.01	<0.01	<0.01	<0.01	<0.01	<0.01	<0.01	<0.01	<0.01	0.0	-	-	-	0.00
Ho	0.48	0.5	0.51	0.49	0.49	0.52	0.65	0.61	0.64	0.73	0.57	0.71	0.25	0.23	0.69	0.53	0.73	0.69	0.69	0.77	0.76	0.79	0.6	-	-	-	0.52
La	15.4	19.6	17.5	16.3	16.9	16	28	19.5	29.1	30.6	26.9	19.9	9.5	9	20.9	18	21.1	22.4	22.2	29.3	27.5	29.6	20.6	14	24	19	20.15
Lu	0.22	0.24	0.23	0.23	0.24	0.22	0.28	0.25	0.27	0.3	0.25	0.3	0.11	0.1	0.29	0.25	0.34	0.29	0.29	0.3	0.34	0.35	0.2	-	-	-	0.23
Mo	0.3	0.4	0.2	0.4	0.3	0.2	0.2	0.2	1.1	1.2	0.6	0.1	0.8	0.2	0.4	0.5	0.2	0.2	0.2	0.5	0.7	0.5	0.1	-	-	-	0.37
Nb	5.5	5.3	5.8	5.6	5.3	4.7	5.3	5.6	5.3	4.7	5	4.4	4.1	4.4	6.2	4.8	5.5	4.1	3.8	5.1	5.3	6.1	6.0	5	6	5	4.96
Nd	16.9	20.8	19	18	18.5	18.1	25.7	21.3	23.8	27	23.7	20.9	10.3	9	21.8	19.9	22	23.2	20.4	29.3	25.1	27.6	17.5	-	-	-	18.45
Ni	3.2	3	3	2.6	3.2	2.6	<20	<20	<20	22.1	11.9	36	<20	<20	<20	<20	<20	20	<20	<20	<20	<20	1.6	<10	<10	10	4.20
Pb	3.1	7.5	6.4	4.8	5	4.2	3.5	2.4	10.9	7.7	4.4	5.7	4.2	3	3.9	3.6	5.4	1.6	2.7	2.3	9.3	2	5.9	16	20	19	5.60
Pr	3.98	4.85	4.64	4.3	4.13	4.09	6.64	4.93	6.27	6.58	6.01	5.14	2.37	2.19	5.19	4.58	5.43	5.5	5.04	6.98	6.24	6.77	4.4	-	-	-	4.47
Rb	26.8	32	29.4	29.4	35.2	29.1	32.3	30.4	17.2	18.1	28.9	25	40.2	35.7	27.7	32.2	25.3	34.5	27.4	18.5	31.1	27.8	25.4	38	35	34	28.18
Sb	<0.1	0.1	0.2	<0.1	<0.1	0.1	<0.1	<0.1	0.1	0.1	0.2	<0.1	<0.1	<0.1	<0.1	<0.1	<0.1	<0.1	<0.1	<0.1	0.1	<0.1	<0.1	-	-	-	0.03
Sc	6	7	6	6	6	7	11	6	11	16	12	13	4	3	8	7	11	16	15	12	7	9	5.0	-	-	-	7.85
Se	<0.5	0.6	<0.5	<0.5	<0.5	<0.5	0.9	1.5	1.6	<0.5	<0.5	0.6	1.6	1.3	1.4	<0.5	<0.5	<0.5	<0.5	<0.5	<0.5	<0.5	<0.5	-	-	-	0.37
Sm	3.72	3.51	4	3.84	3.76	3.51	4.96	4.24	4.41	4.88	4.48	4.46	1.93	1.75	4.21	3.84	4.86	4.67	4.12	5.62	4.92	5.33	3.2	-	-	-	3.63
Sn	<1	<1	<1	<1	<1	<1	<1	<1	<1	1	<1	<1	<1	<1	<1	<1	<1	<1	<1	<1	<1	<1	3.2	-	-	-	0.16
Sr	1021.2	1020.8	1196.5	1202.6	1042.5	1037.9	1130.4	1119.8	1168.9	1121.6	1102.1	1009	1064.6	1080.7	1014.2	1091.4	941.2	909	954.9	1145.9	1048.9	981.8	1072.4	1024	1106	1129	1023.40
Ta	0.2	0.3	0.2	0.3	0.2	0.3	0.3	0.4	0.3	0.3	0.3	0.3	0.2	0.2	0.3	0.2	0.4	0.2	0.2	0.3	0.3	0.3	0.3	-	-	-	0.24
Tb	0.43	0.46	0.48	0.46	0.48	0.43	0.6	0.52	0.53	0.61	0.53	0.61	0.24	0.22	0.57	0.47	0.63	0.62	0.56	0.7	0.62	0.66	0.4	-	-	-	0.46
Th	2.7	2.7	2.7	2.4	2.5	2.3	4.9	3	4.8	5	4.2	2.7	1.6	1.5	2.8	2.9	3	3.5	4.1	4.8	4.8	4.2	3.5	1	3	5	3.10
Tl	<0.1	<0.1	<0.1	<0.1	<0.1	<0.1	0.2	<0.1	<0.1	<0.1	<0.1	<0.1	<0.1	<0.1	<0.1	<0.1	<0.1	<0.1	<0.1	<0.1	<0.1	<0.1	<0.1	-	-	-	0.01
Tm	0.21	0.22	0.22	0.22	0.21	0.21	0.27	0.26	0.27	0.28	0.26	0.28	0.11	0.1	0.3	0.23	0.31	0.27	0.29	0.32	0.31	0.34	0.2	-	-	-	0.22
U	0.9	1.1	0.9	0.9	0.9	1	1.5	1.2	1.8	1.5	1.5	1.5	1	0.9	1.4	1.3	1.3	1	1.5	1.5	1.6	1.4	1.8	0	2	2	1.21
V	60	65	62	63	67	62	133	74	148	170	141	179	54	60	93	69	110	148	170	125	69	85	53.0	-	-	-	86.92
W	0.6	<0.5	<0.5	<0.5	<0.5	<0.5	0.6	<0.5	0.6	<0.5	0.5	<0.5	2.3	0.5	<0.5	0.7	<0.5	<0.5	<0.5	<0.5	<0.5	0.5	0.8	-	-	-	0.27
Y	14.6	15.4	14.8	14.5	14.6	14.5	17.6	15.9	16.2	19.5	15.9	17.5	7.1	6	17.7	15.9	20	18.9	18.3	20.5	20.4	21.5	14.3	8	23	18	15.48
Yb	1.39	1.53	1.5	1.55	1.58	1.37	1.89	1.66	1.88	1.91	1.63	2.1	0.63	0.6	1.99	1.56	2.21	1.85	1.88	2.01	2.19	2.22	1.7	-	-	-	1.49
Zn	40	69	53	44	67	31	53	39	61	75	72	67	50	43	65	54	90	53	38	47	57	45	61.0	-	-	-	49.00
Zr	117.7	116.3	113.5	112.8	107.1	109.6	126.2	120	113.9	110.7	100.7	114.5	90.4	98.9	140.4	130.3	137	109.8	94.9	122.6	131.9	126.6	120.0	158	192	123	115.99

Table 14. Whole-rock trace-element compositions for rocks with Texture 4

Texture 4 Geochemistry Data - Trace Elements				
	Samples #			
Trace Element (ppm)	ME109	ME132	ME137	Averages
Ag	0.2	<0.1	<0.1	0.07
As	17.8	<0.5	0.8	6.20
Au (ppb)	0.6	<0.5	<0.5	0.20
Ba	719	798.0	884.0	800.33
Be	2	<1	<1	0.67
Bi	0.1	<0.1	<0.1	0.03
Cd	<0.1	<0.1	<0.1	-
Ce	23.4	35.7	25.1	28.07
Co	6.5	6.0	4.6	5.70
Cs	0.6	1.3	3.9	1.93
Cu	20.1	1.4	14.9	12.13
Dy	1.55	2.6	1.5	1.88
Er	0.94	1.6	1.0	1.16
Eu	0.69	1.0	0.7	0.80
Ga	18.1	15.5	14.5	16.03
Gd	2.09	3.2	2.0	2.43
Hf	3.1	2.8	2.3	2.73
Hg	<0.01	<0.01	<0.01	-
Ho	0.33	0.5	0.4	0.41
La	12.4	18.0	13.4	14.60
Lu	0.13	0.2	0.2	0.17
Mo	0.2	<0.1	0.1	0.10
Nb	4.3	4.8	4.0	4.37
Nd	11.6	19.0	12.6	14.40
Ni	<20	4.3	3.0	2.43
Pb	6.9	2.2	6.1	5.07
Pr	2.91	4.5	3.0	3.46
Rb	39.2	31.4	45.9	38.83
Sb	0.2	<0.1	<0.1	0.07
Sc	7	7.0	5.0	6.33
Se	<0.5	<0.5	<0.5	-
Sm	2.29	3.6	2.4	2.75
Sn	<1	3.6	2.4	1.99
Sr	1037.6	1012.1	781.3	943.67
Ta	0.2	0.2	0.2	0.20
Tb	0.28	0.5	0.3	0.34
Th	2.7	2.5	2.7	2.63
Tl	<0.1	<0.1	<0.1	-
Tm	0.13	0.2	0.1	0.16
U	0.9	1.2	0.9	1.00
V	68	60.0	58.0	62.00
W	0.6	<0.5	<0.5	0.20
Y	9.2	14.5	9.5	11.07
Yb	0.92	1.5	1.1	1.16
Zn	53	79.0	57.0	63.00
Zr	109.4	103.5	88.2	100.37

Table 15. Whole-rock trac Whole-rock trace-element compositions for rocks with

	Texture 5 Geochemistry Data - Trace Elements																
	Samples #																
Trace Element (ppm)	ME10	ME11	ME12	ME13	ME14	ME15	ME112	ME113	ME116	ME129	ME136	ELLN-4	ELLN-5	ELLN-10	ELLN-11	LLN-11i-	Average
Ag	<0.1	<0.1	<0.1	<0.1	<0.1	<0.1	<0.1	<0.1	<0.1	<0.1	<0.1	-	-	-	-	-	-
As	1.3	1	2.5	0.6	0.7	0.8	1	10.1	<0.5	<0.5	<0.5	-	-	-	-	-	1.13
Au (ppb)	<0.5	1	1.8	1.2	6.8	<0.5	<0.5	5.8	<0.5	2.0	0.9						1.22
Ba	644	3689	1612	1058	991	864	701	579	442	762.0	988.0	698	790	362	688	226	943.38
Be	<1	3	1	<1	<1	3	<1	<1	1	<1	<1	-	-	-	-	-	0.50
Bi	<0.1	<0.1	<0.1	<0.1	<0.1	<0.1	<0.1	<0.1	<0.1	0.1	<0.1	-	-	-	-	-	0.01
Cd	0.1	<0.1	<0.1	<0.1	<0.1	<0.1	<0.1	0.1	<0.1	<0.1	<0.1	-	-	-	-	-	0.01
Ce	47.8	50.4	38.5	38.3	27.2	26.7	43.9	51.7	43.3	32.8	33.8	56.9			40.8	33.2	35.33
Co	11.2	11.2	6.8	6.2	6.5	8.5	5.4	6.2	12.1	14.9	5.3	-	-	-	-	-	5.89
Cs	0.6	0.6	0.5	0.3	0.9	0.2	0.4	0.9	0.3	0.5	0.4	-	-	-	-	-	0.35
Cu	24.9	20.9	9.6	10.3	19.1	20.5	6.5	8.9	13.4	12.3	2.1	-	-	-	-	-	9.28
Dy	3.66	3.82	2.5	2.39	2.04	1.85	2.85	3.79	2.59	2.4	2.5	-	-	-	-	-	1.90
Er	2.36	2.51	1.38	1.43	1.06	1.22	1.68	2.64	1.46	1.7	1.5	-	-	-	-	-	1.18
Eu	1.43	1.37	0.93	1.07	1.03	0.79	1.37	1.48	1.2	0.9	1.0	1.8			1.33	1.01	1.04
Ga	19	18.9	19.3	19.2	19.4	16.6	19.1	19.8	19.3	17.3	16.1	-	-	-	-	-	12.75
Gd	4.47	4.55	3.15	3.01	2.69	2.32	3.92	4.63	3.3	2.6	2.9	-	-	-	-	-	2.35
Hf	3.6	4	3.3	3.2	3.2	2.4	3.4	3.4	2.3	3.4	3.4	-	-	-	-	-	2.23
Hg	<0.01	<0.01	<0.01	<0.01	<0.01	<0.01	<0.01	<0.01	<0.01	0.0	<0.01	-	-	-	-	-	-
Ho	0.77	0.81	0.47	0.48	0.37	0.39	0.56	0.81	0.5	0.6	0.5	-	-	-	-	-	0.39
La	24	24.9	19.3	20.6	14.3	13.6	22.4	27.3	23.8	19.8	18.8	29.9	14	36	20.5	14.6	21.49
Lu	0.37	0.38	0.21	0.22	0.16	0.18	0.23	0.38	0.23	0.3	0.3	0.36	-	-	0.27	0.22	0.23
Mo	0.4	0.5	0.5	0.4	<0.1	<0.1	0.4	0.5	0.5	<0.1	0.1	-	-	-	-	-	0.21
Nb	6.4	6.3	5.9	5.8	4.8	3.6	5	6.1	3.4	6.2	5.7	5	4	4	5	2	4.95
Nd	23.9	24.4	18.1	18.3	16.1	12.7	22.1	25.5	20.1	15.0	16.8	30.9	-	-	22.1	21.3	17.96
Ni	<20	<20	<20	<20	<20	<20	<20	<20	<20	1.0	3.3	13	<10	50	<10	63	8.14
Pb	3.3	3.1	2.9	3.4	4.2	3.4	1.4	5.6	1.4	3.9	1.5	15	15	8	10	8	5.63
Pr	5.96	6.04	4.56	4.57	3.6	3.13	5.54	6.28	5.01	3.9	4.4	-	-	-	-	-	3.31
Rb	24.1	21.5	39.3	33.1	29.2	36.2	24.8	28.7	30.7	22.5	23.5	28	35	18	28	4	26.66
Sb	<0.1	<0.1	<0.1	<0.1	<0.1	<0.1	<0.1	<0.1	<0.1	<0.1	<0.1	-	-	-	-	-	-
Sc	10	10	5	5	6	8	6	6	9	4.0	5.0	-	-	-	-	-	4.63
Se	1	1.1	0.8	1.3	1.1	<0.5	<0.5	<0.5	<0.5	<0.5	<0.5	-	-	-	-	-	0.33
Sm	4.87	4.94	3.44	3.14	3.25	2.55	4.34	5.09	3.8	2.9	3.3	6.01	-	-	4.27	3.95	3.49
Sn	<1	<1	<1	<1	<1	<1	<1	<1	<1	2.9	3.3	-	-	-	-	-	0.39
Sr	977.2	1062.1	980.8	1199.2	1170.1	1186.8	945.4	1000.2	937.5	1036.5	1138.9	1186	1183	729	1214	673	1038.73
Ta	0.3	0.3	0.3	0.3	0.3	0.2	0.3	0.3	0.2	0.3	0.3	0.32	-	-	0.3	0.1	0.24
Tb	0.66	0.68	0.43	0.44	0.39	0.31	0.52	0.67	0.46	0.4	0.4	0.75	-	-	0.57	0.51	0.45
Th	3.4	3.3	3.3	3.7	2	2.1	3.5	5.3	4.4	3.2	2.5	4.6	1	2	3.3	0.9	3.03
Tl	<0.1	<0.1	<0.1	<0.1	<0.1	<0.1	<0.1	<0.1	<0.1	<0.1	<0.1	-	-	-	-	-	-
Tm	0.35	0.36	0.21	0.21	0.16	0.18	0.23	0.35	0.22	0.2	0.2	-	-	-	-	-	0.17
U	1.4	1.5	1.6	1.5	1.2	1.3	1.4	1.8	1.6	1.7	1.2	1.6	0	2	1.4	0.8	1.38
V	118	121	75	77	69	92	55	63	114	33.0	51.0	-	-	-	-	-	54.25
W	0.7	0.5	<0.5	0.5	<0.5	<0.5	<0.5	0.7	<0.5	1.0	<0.5	-	-	-	-	-	0.21
Y	22	21.9	13.5	12.5	10.4	10.2	16.4	22.2	14.3	14.9	13.8	23	13	19	19	17	16.44
Yb	2.43	2.36	1.47	1.42	1.12	1.16	1.58	2.45	1.5	1.8	1.4	-	-	-	-	-	1.16
Zn	69	75	43	61	56	42	20	82	33	59.0	45.0	-	-	-	-	-	36.56
Zr	147.1	152.2	123.5	128.1	120.8	89	120.7	134.1	86.6	124.5	120.8	194	169	90	120	37	122.34

11.2 Appendix B: Anisotropy of Magnetic Susceptibility Data

Table 16. AMS data for Texture 1

AMS Data Texture 1										
Sample	**Source**	**Intrusive Center**	**UTM_nad83 Easting**	**UTM_nad83 Northing**	**# of Specimens**	**Km (SI)**	**L**	**F**	**P_j**	**T**
ME8	Texture 1	Ellen	521243	4210732	6	0.075300	1.009	1.007	1.016	-0.170
ME9	Texture 1	Ellen	521274	4211060	6	0.042600	1.010	1.007	1.018	-0.180
CR3	Texture 1	Ellen	521585	4211068	6	0.017800	1.014	1.004	1.019	-0.503
CR15	Texture 1	Ellen	520710	4210792	6	0.000272	1.016	1.008	1.025	-0.321
CR18	Texture 1	Ellen	520595	4211096	6	0.017900	1.011	1.013	1.025	0.078
CR19	Texture 1	Ellen	521687	4210995	5	0.019400	1.013	1.008	1.022	-0.220
CR48	Texture 1	Ellen	521868	4211416	6	0.000367	1.006	1.021	1.029	0.587
CR54	Texture 1	Ellen	519964	4210017	6	0.000296	1.007	1.012	1.020	0.248
CR59	Texture 1	Ellen	521621	4210621	6	0.020900	1.009	1.016	1.026	0.306
CR66	Texture 1	Ellen	521670	4210179	6	0.033800	1.013	1.011	1.025	-0.099
CR71	Texture 1	Ellen	521722	4211507	5	0.013600	1.012	1.010	1.022	-0.117
CR82	Texture 1	Ellen	520421	4209011	6	0.009150	1.003	1.016	1.021	0.656
CR83	Texture 1	Ellen	520462	4209005	6	0.003140	1.014	1.012	1.026	-0.085
CR84	Texture 1	Ellen	520277	4209295	5	0.005240	1.041	1.004	1.050	-0.818
CR86	Texture 1	Ellen	520738	4211618	6	0.000335	1.013	1.009	1.023	-0.171
CR95	Texture 1	Ellen	520210	4210273	6	0.028700	1.008	1.025	1.035	0.493
CR96	Texture 1	Ellen	520256	4210291	6	0.000312	1.009	1.022	1.032	0.436
CR101	Texture 1	Ellen	521500	4210388	6	0.018800	1.014	1.012	1.026	-0.069
CR114	Texture 1	Ellen	521267	4210884	6	0.026900	1.016	1.007	1.023	-0.402
ME103	Texture 1	Ellen	519256	4213062	6	0.036500	1.006	1.032	1.041	0.675
ME105	Texture 1	Ellen	523433	4216214	6	0.005630	1.012	1.014	1.027	0.086
ME119	Texture 1	Ellen	519170	4217092	7	0.037200	1.017	1.017	1.034	-0.015
ME120	Texture 1	Ellen	523224	4222671	6	0.017400	1.013	1.015	1.028	0.072
ME124	Texture 1	Ellen	520182	4217331	6	0.059700	1.021	1.024	1.045	0.049
ME125	Texture 1	Ellen	522778	4220030	7	0.000224	1.006	1.020	1.027	0.554
ME126	Texture 1	Ellen	523219	4220700	6	0.016800	1.018	1.009	1.028	-0.397
ME130	Texture 1	Ellen	518505	4213191	6	0.050400	1.009	1.042	1.055	0.640
ME133	Texture 1	Ellen	519286	4213082	6	0.031500	1.010	1.020	1.031	0.342
CR1	Texture 1	Ellen	521166	4211222	6	0.003800	1.018	1.017	1.036	-0.016
CR12	Texture 1	Ellen	521044	4210345	9	0.009200	1.016	1.011	1.028	-0.192
CR31	Texture 1	Ellen	520802	4211428	7	0.000297	1.009	1.009	1.018	0.067

Table 17. AMS data for Texture 2

AMS Data Texture 2										
Sample	**Source**	**Intrusive Center**	**UTM_nad83 Easting**	**UTM_nad83 Northing**	**# of Specimens**	**Km (SI)**	**L**	**F**	**P_j**	**T**
ME134	Texture 2	Ellen	519418	4216165	7	0.017700	1.007	1.009	1.016	0.125
ME16	Texture 2	Ellen	521364	4214185	6	0.024400	1.016	1.007	1.024	-0.393
ME19	Texture 2	Ellen	521467	4213983	6	0.053100	1.026	1.011	1.038	-0.425

Table 18. AMS data for Texture 3

AMS Data Texture 3										
Sample	**Source**	**Intrusive Center**	**UTM_nad83 Easting**	**UTM_nad83 Northing**	**# of Specimens**	**Km (SI)**	**L**	**F**	**P_j**	**T**
ME6	Texture 3	Ellen	521180	4210224	6	0.027900	1.015	1.016	1.032	0.039
ME7	Texture 3	Ellen	521224	4210472	6	0.014300	1.006	1.009	1.015	0.242
CR2	Texture 3	Ellen	521586	4211623	6	0.006150	1.019	1.025	1.045	0.122
CR7	Texture 3	Ellen	522167	4211066	6	0.022700	1.026	1.019	1.046	-0.151
CR8	Texture 3	Ellen	522049	4211158	6	0.037200	1.014	1.007	1.021	-0.363
CR9a	Texture 3	Ellen	521942	4211221	6	0.018900	1.019	1.014	1.034	-0.156
CR10	Texture 3	Ellen	521064	4210512	6	0.000403	1.012	1.020	1.033	0.273
CR24	Texture 3	Ellen	521937	4210348	6	0.018300	1.021	1.022	1.043	0.038
CR49	Texture 3	Ellen	521895	4211488	6	0.000152	1.006	1.007	1.013	0.139
CR62	Texture 3	Ellen	521743	4209868	6	0.023100	1.011	1.010	1.021	-0.033
CR63	Texture 3	Ellen	521788	4209571	6	0.019800	1.005	1.021	1.028	0.620
CR73	Texture 3	Ellen	521870	4211677	6	0.000222	1.010	1.009	1.019	-0.016
CR76	Texture 3	Ellen	521598	4211906	6	0.013800	1.018	1.014	1.033	-0.118
CR81	Texture 3	Ellen	521245	4212011	6	0.020000	1.017	1.016	1.033	-0.045
CR87	Texture 3	Ellen	522210	4211692	6	0.016200	1.009	1.015	1.025	0.259
CR88	Texture 3	Ellen	522480	4211948	6	0.006670	1.007	1.010	1.016	0.178
CR103	Texture 3	Ellen	521432	4210261	6	0.014700	1.016	1.020	1.036	0.100
CR104	Texture 3	Ellen	521325	4210067	6	0.007370	1.008	1.017	1.026	0.364
CR105	Texture 3	Ellen	521375	4209868	6	0.015100	1.016	1.024	1.040	0.195
CR113	Texture 3	Ellen	521175	4210423	6	0.008780	1.012	1.020	1.032	0.231
ME101	Texture 3	Ellen	514984	4211129	9	0.000242	1.007	1.021	1.029	0.511
ME106	Texture 3	Ellen	519773	4211075	6	0.001380	1.032	1.047	1.084	0.069
ME114	Texture 3	Ellen	515652	4213566	8	0.047500	1.007	1.010	1.017	0.136
ME117	Texture 3	Ellen	517587	4210688	8	0.081700	1.003	1.011	1.015	0.591
ME118	Texture 3	Ellen	520917	4214005	8	0.026600	1.010	1.012	1.022	0.120
ME122	Texture 3	Ellen	520731	4219216	6	0.004070	1.007	1.012	1.020	0.219
ME123	Texture 3	Ellen	519657	4216859	7	0.052000	1.003	1.009	1.013	0.397
ME127	Texture 3	Ellen	522946	4213657	6	0.016800	1.018	1.009	1.028	-0.397
CR35	Texture 3	Ellen	521102	4212242	6	0.039300	1.008	1.020	1.029	0.431
CR67	Texture 3	Ellen	520088	4211048	6	0.000248	1.010	1.007	1.017	-0.196
CR75	Texture 3	Ellen	521661	4211871	7	0.018200	1.020	1.016	1.036	-0.126
ME21	Texture 3	Ellen	520753	4208300	6	0.013000	1.023	1.031	1.054	0.150

Table 19. AMS data for Texture 4

AMS Data Texture 4										
Sample	**Source**	**Intrusive Center**	**UTM_nad83 Easting**	**UTM_nad83 Northing**	**# of Specimens**	**Km (SI)**	**L**	**F**	**P_j**	**T**
ME109	Texture 4	Ellen	514033	4216670	6	0.000299	1.014	1.048	1.067	0.442
ME131	Texture 4	Ellen	519175	4213001	6	0.011400	1.004	1.028	1.035	0.785
ME132	Texture 4	Ellen	519795	4213384	6	0.011200	1.008	1.011	1.020	0.256
ME137	Texture 4	Ellen	524281	4207556	6	0.005250	1.035	1.029	1.065	-0.087

Table 20. AMS data for Texture 5

AMS Data Texture 5										
Sample	**Source**	**Intrusive Center**	**UTM_nad83 Easting**	**UTM_nad83 Northing**	**# of Specimens**	**Km (SI)**	**L**	**F**	**P_j**	**T**
ME102	Texture 5	Ellen	519454	4211255	6	0.000358	1.013	1.018	1.031	0.151
ME112	Texture 5	Ellen	513938	4225442	8	0.035400	1.007	1.009	1.016	0.124
ME113	Texture 5	Ellen	518074	4215441	6	0.001580	1.054	1.043	1.104	-0.185
ME116	Texture 5	Ellen	516196	4211046	7	0.000453	1.020	1.022	1.045	0.195
ME129	Texture 5	Ellen	518788	4212901	7	0.024000	1.021	1.013	1.034	-0.228
ME135	Texture 5	Ellen	519345	4214987	7	0.000197	1.006	1.009	1.014	0.230
ME136	Texture 5	Ellen	519632	4214450	6	0.018200	1.013	1.020	1.033	0.214
ME10	Texture 5	Ellen	519588	4215672	5	0.005450	1.019	1.012	1.032	-0.244
ME11	Texture 5	Ellen	519915	4215563	5	0.000408	1.009	1.012	1.021	0.171
ME12	Texture 5	Ellen	519916	4215173	7	0.011800	1.015	1.014	1.029	0.028
ME13	Texture 5	Ellen	520281	4215040	8	0.010900	1.022	1.013	1.036	-0.350
ME14	Texture 5	Ellen	520282	4214876	6	0.000273	1.008	1.012	1.020	0.131
ME15	Texture 5	Ellen	521133	4214650	6	0.005480	1.010	1.011	1.021	-0.002

11.3 Appendix C: Crystal Size Distribution Data

Table 21. CSD data for Hornblende phenocrysts – Texture 1

Hornblende CSD data for Texture 1						
Sample #	ME105		ME114		ME120	
	Crystal Size (mm)	ln (pop density) (mm^{-4})	Crystal Size (mm)	ln (pop density) (mm^{-4})	Crystal Size (mm)	ln (pop density) (mm^{-4})
	5.06	-11.19	5.06	-11.09	5.06	-10.02
	3.19	-7.33	3.19	-9.11	3.19	-7.4
	2.01	-4.65	2.01	-5.69	2.01	-5.01
	1.27	-2.8	1.27	-3.44	1.27	-3.18
	0.801	-0.94	0.801	-1.5	0.801	-1.63
	0.506	0.59	0.506	-0.02	0.506	-0.29
	0.319	2.04	0.319	1.15	0.319	0.96
	0.201	3.38	0.201	2.07	0.201	2.21
	0.127	4.51	0.127	2.57	0.127	3.03
Sample #	ME126		ME138		ME103	
	Crystal Size (mm)	ln (pop density) (mm^{-4})	Crystal Size (mm)	ln (pop density) (mm^{-4})	Crystal Size (mm)	ln (pop density) (mm^{-4})
	5.06	-11.57	5.06	-10.94	8.01	-11.36
	3.19	-8.72	3.19	-8.31	5.06	-8.57
	2.01	-6.34	2.01	-6.43	3.19	-6.87
	1.27	-4.69	1.27	-4.61	2.01	-5.04
	0.801	-3.2	0.801	-3.34	1.27	-3.3
	0.506	-2	0.506	-2.26	0.801	-1.91
	0.319	-1.25	0.319	-1.48	0.506	-0.41
	0.201	-0.36	0.201	-0.82	0.319	0.94
	0.127	-0.12	0.127	-0.46	0.201	2.38
					0.127	3.77
Sample #	ME119		ME133		ME124	
	Crystal Size (mm)	ln (pop density) (mm^{-4})	Crystal Size (mm)	ln (pop density) (mm^{-4})	Crystal Size (mm)	ln (pop density) (mm^{-4})
	3.19	-8.04	3.19	-10.19	12.7	-13.38
	2.01	-5.33	2.01	-7.34	8.01	-11.83
	1.27	-3.14	1.27	-5.47	5.06	-9.38
	0.801	-1.54	0.801	-3.43	3.19	-7.64
	0.506	-0.11	0.506	-2.14	2.01	-5.37
	0.319	1.21	0.319	-0.98	1.27	-3.51
	0.201	2.27	0.201	0	0.801	-1.83
	0.127	3.1	0.127	0.34	0.506	-0.13
					0.319	1.29
					0.201	2.56
					0.127	3.42

Table 22. CSD data for Hornblende phenocrysts – Texture 2

Hornblende CSD data for - Texture 2				
Sample #	ME16		ME134	
	Crystal Size (mm)	ln (pop density) (mm $^{-4}$)	Crystal Size (mm)	ln (pop density) (mm $^{-4}$)
	5.06	-10.33	5.06	-10.26
	3.19	-9.56	3.19	-10.95
	2.01	-6.11	2.01	-8.21
	1.27	-3.97	1.27	-6.75
	0.801	-2.01	0.801	-4.55
	0.506	-0.25	0.506	-2.94
	0.319	1.25	0.319	-0.69
	0.201	2.64	0.201	1.23
	0.127	3.88	0.127	2.67

Table 23. CSD data for Hornblende phenocrysts – Texture 3

Hornblende CSD data for Texture 3						
Sample #	ME137		ME122		ME118	
	Crystal Size (mm)	ln (pop density) (mm^{-4})	Crystal Size (mm)	ln (pop density) (mm^{-4})	Crystal Size (mm)	ln (pop density) (mm^{-4})
	3.19	-7.84	5.06	-11.47	5.06	-10.68
	2.01	-5.46	3.19	-7.34	3.19	-8.07
	1.27	-3.34	2.01	-5.02	2.01	-5.45
	0.801	-1.75	1.27	-2.9	1.27	-3.28
	0.506	-0.45	0.801	-1.22	0.801	-1.25
	0.319	0.68	0.506	0.28	0.506	0.3
	0.201	1.57	0.319	1.53	0.319	1.56
	0.127	2.44	0.201	2.55	0.201	2.51
			0.127	3.25	0.127	3.25
Sample #	ME123		ME17		ME127	
	Crystal Size (mm)	ln (pop density) (mm^{-4})	Crystal Size (mm)	ln (pop density) (mm^{-4})	Crystal Size (mm)	ln (pop density) (mm^{-4})
	5.06	-11.03	2.01	-7.14	5.06	-11.56
	3.19	-7.98	1.27	-4.86	3.19	-8.71
	2.01	-5.98	0.801	-3.1	2.01	-6.33
	1.27	-3.65	0.506	-1.61	1.27	-4.69
	0.801	-1.89	0.319	-0.7	0.801	-3.2
	0.506	-0.37	0.201	0.01	0.506	-1.99
	0.319	1.01	0.127	0.62	0.319	-1.24
	0.201	2.33			0.201	-0.36
	0.127	3.53			0.127	-0.13

Table 24. CSD data for Hornblende phenocrysts – Texture 4

Hornblende CSD data for Texture 4						
Sample #	ME137		ME131		ME132	
	Crystal Size (mm)	ln (pop density) (mm^{-4})	Crystal Size (mm)	ln (pop density) (mm^{-4})	Crystal Size (mm)	ln (pop density) (mm^{-4})
	5.06	-11.43	2.01	-8.6	2.01	-10.41
	3.19	-7.92	1.27	-6.47	1.27	-6.6
	2.01	-5.53	0.801	-4.2	0.801	-4.69
	1.27	-3.85	0.506	-2.83	0.506	-2.89
	0.801	-2.66	0.319	-1.3	0.319	-1.42
	0.506	-1.31	0.201	-0.05	0.201	-0.36
	0.319	-0.4	0.127	0.54	0.127	-0.64
	0.201	0.6				
	0.127	1.22				
Sample #	ME109					
	Crystal Size (mm)	ln (pop density) (mm^{-4})				
	3.19	-9.46				
	2.01	-6.82				
	1.27	-4.23				
	0.801	-2.32				
	0.506	-0.63				
	0.319	0.72				
	0.201	1.68				
	0.127	2.54				
	0.0801	2.18				

Table 25. CSD data for Hornblende phenocrysts – Texture 5

Hornblende CSD data for Texture 5						
Sample #	ME136		ME112		ME113	
	Crystal Size (mm)	ln (pop density) (mm^{-4})	Crystal Size (mm)	ln (pop density) (mm^{-4})	Crystal Size (mm)	ln (pop density) (mm^{-4})
	3.19	-9.48	3.19	-9.96	12.7	-13.22
	2.01	-8.24	2.01	-7.27	8.01	-11.67
	1.27	-5.53	1.27	-4.22	5.06	-9.34
	0.801	-3.39	0.801	-2.21	3.19	-6.55
	0.506	-1.86	0.506	-0.36	2.01	-4.66
	0.319	-0.62	0.319	1.29	1.27	-3.09
	0.201	0.16	0.201	2.52	0.801	-1.72
	0.127	0.73	0.127	3.38	0.506	-0.35
			0.0801	2.75	0.319	1.02
					0.201	2.39
					0.127	3.74
Sample #	ME116		ME102		ME12	
	Crystal Size (mm)	ln (pop density) (mm^{-4})	Crystal Size (mm)	ln (pop density) (mm^{-4})	Crystal Size (mm)	ln (pop density) (mm^{-4})
	2.01	-5.98	0.801	-3.1	2.01	-6.33
	1.27	-3.65	0.506	-1.61	1.27	-4.69
	0.801	-1.89	0.319	-0.7	0.801	-3.2
	0.506	-0.37	0.201	0.01	0.506	-1.99
	0.319	1.01	0.127	0.62	0.319	-1.24
	0.201	2.33			0.201	-0.36
	0.127	3.53			0.127	-0.13

Table 26. CSD data for Plagioclase phenocrysts – Texture 1

Plagioclase CSD data for Texture 1						
Sample #	ME105		CR19		CR48	
	Crystal Size (mm)	ln (pop density) (mm^{-4})	Crystal Size (mm)	ln (pop density) (mm^{-4})	Crystal Size (mm)	ln (pop density) (mm^{-4})
	12.7	-13.52	12.7	-13.89	12.7	-15.498
	8.01	-10.41	8.01	-12.86	8.01	-13.74
	5.06	-8.1	5.06	-9.61	5.06	-10.32
	3.19	-6.65	3.19	-8.07	3.19	-7.88
	2.01	-5.42	2.01	-6.76	2.01	-6.44
	1.27	-4.39	1.27	-5.38	1.27	-5.08
	0.801	-3.17	0.801	-4.95	0.801	-4.74
	0.506	-1.77				
	0.319	-0.19				
	0.201	0.93				
Sample #	CR59		CR84		CR95	
	Crystal Size (mm)	ln (pop density) (mm^{-4})	Crystal Size (mm)	ln (pop density) (mm^{-4})	Crystal Size (mm)	ln (pop density) (mm^{-4})
	5.06	-10.91	8.01	-13.76	8.01	-12.57
	3.19	-8.32	5.06	-10.92	5.06	-10.29
	2.01	-6.93	3.19	-8.47	3.19	-8.33
	1.27	-5.55	2.01	-7	2.01	-6.92
	0.801	-5.07	1.27	-5.63	1.27	-5.54
			0.801	-5.11	0.801	-4.47
Sample #	ME9a		ME138		ME119	
	Crystal Size (mm)	ln (pop density) (mm^{-4})	Crystal Size (mm)	ln (pop density) (mm^{-4})	Crystal Size (mm)	ln (pop density) (mm^{-4})
	12.7	-15.24	5.06	-10.75	8.01	-10.53
	8.01	-13.7	3.19	-8.18	5.06	-9.19
	5.06	-9.79	2.01	-6.23	3.19	-7.32
	3.19	-7.64	1.27	-5.07	2.01	-5.4
	2.01	-5.95	0.801	-3.5	1.27	-4.12
	1.27	-4.77	0.506	-2.42	0.801	-3.13
			0.319	-1.67	0.506	-1.88
			0.201	-1.2	0.319	-0.52
			0.127	-0.89	0.201	0.62
					0.127	1.19
Sample #	ME126		ME133			
	Crystal Size (mm)	ln (pop density) (mm^{-4})	Crystal Size (mm)	ln (pop density) (mm^{-4})		
	12.7	-12.2	8.01	-13.18		
	8.01	-10.23	5.06	-10.08		
	5.06	-8.89	3.19	-7.32		
	3.19	-7.36	2.01	-5.73		
	2.01	-6.02	1.27	-4.57		
	1.27	-4.86	0.801	-3.38		
	0.801	-3.82	0.506	-2.14		
	0.506	-2.51	0.319	-1.3		
	0.319	-1.56	0.201	-0.62		
	0.201	-0.58	0.127	-0.03		
	0.127	-0.02				

Table 27. CSD data for Plagioclase phenocrysts – Texture 2

Plagioclase CSD data for - Texture 2				
Sample #	ME16		ME134	
	Crystal Size (mm)	ln (pop density) (mm $^{-4}$)	Crystal Size (mm)	ln (pop density) (mm $^{-4}$)
	5.06	-9.93	5.06	-11.35
	3.19	-9.16	3.19	-7.87
	2.01	-6.65	2.01	-6.31
	1.27	-4.79	1.27	-4.48
	0.801	-3.38	0.801	-3
	0.506	-1.87	0.506	-1.49
	0.319	-0.59	0.319	0.05
	0.201	0.41	0.201	1.44
	0.127	1.4	0.127	2.67

Table 28. CSD data for Plagioclase phenocrysts – Texture 3

Plagioclase CSD data for Texture 3						
Sample #	ME122		ME114		ME123	
	Crystal Size (mm)	ln (pop density) (mm^{-4})	Crystal Size (mm)	ln (pop density) (mm^{-4})	Crystal Size (mm)	ln (pop density) (mm^{-4})
	8.01	-10.89	5.06	-10.62	3.19	-8.27
	5.06	-8.25	3.19	-8.27	2.01	-5.45
	3.19	-7.08	2.01	-5.55	1.27	-3.37
	2.01	-5.69	1.27	-3.62	0.801	-1.72
	1.27	-4.72	0.801	-2	0.506	-0.35
	0.801	-3.61	0.506	-0.63	0.319	0.7
	0.506	-2.05	0.319	0.63	0.201	1.86
	0.319	-0.63	0.201	1.88	0.127	3.03
	0.201	0.5	0.127	2.38		
Sample #	ME118		CR2		CR9a	
	Crystal Size (mm)	ln (pop density) (mm^{-4})	Crystal Size (mm)	ln (pop density) (mm^{-4})	Crystal Size (mm)	ln (pop density) (mm^{-4})
	8.01	-12.9	8.01	-14.33	8.01	-14.33
	5.06	-10.21	5.06	-11.83	5.06	-10.94
	3.19	-7.92	3.19	-8.46	3.19	-8.49
	2.01	-5.11	2.01	-6.46	2.01	-6.45
	1.27	-3	1.27	-4.85	1.27	-4.98
	0.801	-1.54	0.801	-4.25	0.801	-4.65
	0.506	-0.42				
	0.319	0.71				
	0.201	1.83				
	0.127	2.34				
Sample #	CR14		CR62		CR88	
	Crystal Size (mm)	ln (pop density) (mm^{-4})	Crystal Size (mm)	ln (pop density) (mm^{-4})	Crystal Size (mm)	ln (pop density) (mm^{-4})
	3.19	-8.51	5.06	-11.7	5.06	-10.83
	2.01	-6.33	3.19	-8.73	3.19	-8.71
	1.27	-4.81	2.01	-7.23	2.01	-7.22
	0.801	-3.71	1.27	-5.84	1.27	-5.88
			0.801	-4.93	0.801	-5.03
					0.506	-4.49
Sample #	ME7		CR38		ME17	
	Crystal Size (mm)	ln (pop density) (mm^{-4})	Crystal Size (mm)	ln (pop density) (mm^{-4})	Crystal Size (mm)	ln (pop density) (mm^{-4})
	5.06	-12.3	8.01	-13.24	5.06	-10.77
	3.19	-8.97	5.06	-10.66	3.19	-7.66
	2.01	-6.97	3.19	-7.99	2.01	-5.64
	1.27	-5.52	2.01	-6.39	1.27	-3.85
	0.801	-4.2	1.27	-4.98	0.801	-2.69
			0.801	-4.24	0.506	-1.79
					0.319	-0.9
					0.201	-0.4
					0.127	0.25
Sample #	ME7					
	Crystal Size (mm)	ln (pop density) (mm^{-4})				
	12.7	-12.19				
	8.01	-10.23				
	5.06	-8.88				
	3.19	-7.36				
	2.01	-6.02				
	1.27	-4.85				
	0.801	-3.82				
	0.506	-2.5				
	0.319	-1.55				
	0.201	-0.58				
	0.127	-0.02				

Table 29. CSD data for Plagioclase phenocrysts – Texture 4

Plagioclase CSD data for Texture 4						
Sample #	ME131		ME132		ME137	
	Crystal Size (mm)	ln (pop density) (mm^{-4})	Crystal Size (mm)	ln (pop density) (mm^{-4})	Crystal Size (mm)	ln (pop density) (mm^{-4})
	5.06	-11.04	5.06	-10.03	12.7	-13.32
	3.19	-7.86	3.19	-7.34	8.01	-12.08
	2.01	-5.74	2.01	-5.73	5.06	-9.43
	1.27	-4.18	1.27	-4.29	3.19	-6.99
	0.801	-3.05	0.801	-3.6	2.01	-5.7
	0.506	-2.1	0.506	-2.79	1.27	-4.48
	0.319	-1.62	0.319	-2.14	0.801	-3.33
	0.201	-0.96	0.201	-1.26	0.506	-1.99
	0.127	-0.87	0.127	-0.44	0.319	-0.89
					0.201	0.2
					0.127	1.32

Table 30. CSD data for Plagioclase phenocrysts – Texture 5

Plagioclase CSD data for Texture 5						
Sample #	ME12		ME136		ME102	
	Crystal Size (mm)	ln (pop density) (mm^{-4})	Crystal Size (mm)	ln (pop density) (mm^{-4})	Crystal Size (mm)	ln (pop density) (mm^{-4})
	8.01	-12.15	5.06	-10.74	8.01	-13.23
	5.06	-9.38	3.19	-6.97	5.06	-11.68
	3.19	-7.21	2.01	-5.32	3.19	-7.63
	2.01	-4.8	1.27	-3.84	2.01	-5.44
	1.27	-3.44	0.801	-2.71	1.27	-3.97
	0.801	-2.38	0.506	-2.08	0.801	-2.93
	0.506	-1.51	0.319	-1.5	0.506	-1.94
	0.319	-1.09	0.201	-1.09	0.319	-1.22
	0.201	-0.87	0.127	-0.59	0.201	-0.38
	0.127	-0.95			0.127	-0.05
Sample #	ME113					
	Crystal Size (mm)	ln (pop density) (mm^{-4})				
	8.01	-11.63				
	5.06	-9.12				
	3.19	-6.75				
	2.01	-4.7				
	1.27	-3.19				
	0.801	-2.16				
	0.506	-1.16				
	0.319	-0.33				
	0.201	0.26				

10.4 Appendix D: UTM Coordinates for All Samples

Table 31. UTM coordinates for all samples. All Coordinates in UTM zone 12, with datum NAD83.

Samples	Easting	Northing
ME100	517248	4213902
ME101	514984	4211129
ME102	519480	4211458
ME103	519256	4213062
ME104	523710	4216293
ME105	523433	4216214
ME106	519773	4211075
ME107	515013	4209776
ME108	514337	4214857
ME109	514033	4216670
ME110	515622	4213115
ME111	520577	4214919
ME112	513938	4225442
ME113	518074	4215441
ME114	515652	4213566
ME115	515610	4211707
ME116	516196	4211046
ME117	517587	4210688
ME118	520917	4214005
ME119	519170	4217092
ME120	523224	4222671
ME121	523603	4222672
ME122	520731	4219216
ME123	519657	4216859
ME124	520182	4217331
ME125	522778	4220030
ME126	523219	4220700
ME127	522946	4213657
ME128	517044	4210983
ME129	518788	4212901
ME130	518505	4213191
ME131	519175	4213001
ME132	519795	4213384
ME133	519286	4213082
ME134	519418	4216165
ME135	519345	4214987
ME136	519632	4214450
ME137	524281	4207556
ME138	519411	4216053

**Source of Samples: This Study

Samples	Easting	Northing
ME8	521243	4210732
ME9	521274	4211060
ME10	519588	4215672
ME11	519915	4215563
ME12	519916	4215173
ME13	520281	4215040
ME14	520282	4214876
ME15	521133	4214650
ME16	521364	4214185
ME17	513227	4210730
ME19	521467	4213983
ME20	520953	4208339
ME21	520753	4208300
CR1	521166	4211222
CR8	522049	4211158
CR12	521044	4210345
CR19	521687	4210995
CR31	520802	4211428
CR35	521102	4212242
CR37	521403	4212584
CR46	521871	4211346
CR63	521788	4208571
CR66	521670	4210179
CR67	520088	4211048
CR71	521772	4211507
CR75	521661	4211871
CR76	521598	4211906
CR78	521370	4212036
CR81	521245	4212011
CR82	520421	4209011
CR88	522480	4211948
CR95	520210	4210273
CR100	520528	4212371
CR104	521325	4210067
CR114	521267	4210388

**Source of Samples: Maurer (2015)

Samples	Easting	Northing
ELLN-1	521162	4208431
ELLN-2	518542	4213233
ELLN-3	518810	4213141
ELLN-4	521414	4214442
ELLN-5	521171	4214318
ELLN-6	519264	4217025
ELLN-9	521174	4213208
ELLN-10	521293	4214133
ELLN-11	517196	4216250
ELLN-11i-B	517196	4216250
BULL-1	522804	4222675

**Source of Samples: Nelson & Davidson (1993)